Low-Cost High-Efficiency Solar Cells with Wafer Bonding and Plasmonic Technologies

Thesis by
Katsuaki Tanabe

In Partial Fulfillment of the Requirements
for the Degree of
Doctor of Philosophy

California Institute of Technology
Pasadena, California

2008

(Defended May 21, 2008)

Acknowledgements

First of all, I would like to thank my thesis adviser Harry Atwater for his great mentorship and guidance over the years. While he is an extremely busy professor holding about twenty students in his research group and a lot of domestic and international travels for seminars and conferences, he never hesitated to discuss with me when I knocked on his office's door. Our discussion often went over 1 hour in his tight schedule, but he did not stop until we reached clear conclusions and decided what to do next. While he always tries to find the most effective way for experimental scheme, Harry one day told me that we engineers should always assume possible to fabricate whatever structure possible when I showed a hesitation for doing a complicated process, which preach is still and will be in my mind.

It was also a great pleasure for me to work with the excellent members in the Atwater research group. Anna Fontcuberta i Morral, a fromer postdoc through 2002 to 2003 and currently a research group leader in Walter Schottky Institute in Germany, was a mentor when I first came to Caltech in summer 2003. She gave me an exclusive guidance for wafer bonding and layer transfer technique. Jimmy Zahler, a former grad student graduating in 2005 and currently at BP Solar, also gave me a lot of advice for wafer bonding and multijunction solar cell structures. He was also one of my collaborators as the technical leader at Aonex Technologies for the project in Chapters 5 and 6. Melissa Archer, the other student member of the III-V solar cell subgroup, has been giving me various technical supports particularly for our home-made solar simulator setup and useful discussions on the multijunction solar cell projects as well as sharing the pain to

wait long for the growth by the busy scientists at Spectrolab. She also helped me a lot for the semiconductor polishing process, giving me a ride to UCLA Nanolab. Keisuke Nakayama, a visiting scholar from Nippon Oil in Japan, joined the group late 2006 and accelerated the plasmonic solar cell research progress in Chapter 7 with his more-than-precise nanoparticle making technique. For Chapter 7, I also received a lot of advices on plasmonics from Rene de Waele, Jen Dionne, Vivian Ferry, Henri Lezec, Domenico Pacifici and Luke Sweatlock. Without those people, I would not have realized the significance and excitement of plasmonic technologies. I had nice discussions on solar cell basic principles and potential future technologies with Brendan Kayes and Christine Richardson from the silicon solar cell team. They helped me also for the sample preparation for SIMS measurements, solar simulator setup, e-beam lithography etc. Mike Kelzenberg also gave me an essential technical support through the photolithography process and solar cell measurements. Julie Biteen and Morgan Putnam supported my chemical experiments as the safety officers for our cleanroom. Robb Walters supported me for the optical and electrical measurements particularly for the help to write the LabView codes. I also have received a lot of helps for my experimental works such as furnace annealing by Ryan Briggs, FIB milling by Stan Burgos, oxygen plasma treatment by Ken Diest, and electrical measurements by Youngbae Park.

I had great times of enjoyment in my daily research life and at conferences also with Julie Brewer, Matt Czubakowski, Davis Darvish, Mike Deceglie, Chris de Ruiter, Matt Dicken, Tao Feng, Mike Filler, Anna Hiszpanski, Carrie Hoffman, Ernst Jan Vesseur, Seokmin Jeon, Pieter Kik, Sungjee Kim, Greg Kimball, Beth Lachut, Krista Langeland,

Andrew Leenheer, Stefen Maier, Maribeth Mason, Gerald Miller, Phil Munoz, Deirdre O'Carroll, Imogen Pryce, Jen Ruglovsky and Darci Taylor.

My campus life was also supported largely by the administrative and secretary people at Caltech: Cierina Marks, Mary Metz, April Neidholdt, Connie Rodriguez and Eleonora Vorobieff.

I collaborated several researchers from research institutes outside of Caltech, which was a great experience. Dan Aiken at Emcore Photovoltaics grew the inverted GaAs subcells used in Chapter 4. Mark Wanlass at the National Renewable Energy Laboratory (NREL) grew the InGaAs subcells used also in Chapter 4. Dan and Mark gave me also useful advices for solar cell processing. Corinne Ladous and Tom Pinnington at Aonex Technologies prepared the InP/SiO_2/Si epitaxial templates used in Chapters 5 and 6. I thank them also for their advice on the InP/Si substrate fabrication and for letting me use their cleanroom at Aonex occasionally. Daniel Law at Spectrolab grew the InP/InGaAs double heterostructures on my InP/Si substrates in Chapter 5. Fred Newman at Emcore Photovoltaics grew the InGaAs cells in Chapter 6.

I also greatly appreciate for the support for my studies from the following people. Bob Reedy at NREL conducted the SIMS measurement appeared in Chapter 3. Art Ackerman and Fiona Ku at Aonex Technologies gave me useful advices on the chemical mechanical polishing process. Ewold Verhagen and Prof. Albert Polman at AMOLF in the Netherlands laid the theoretical basis for the energy dissipation calculation in Chapter 7.

Ali Ghaffari, the technical administrator for the departmental facilities in Watson building at Caltech trained me for the use of the cleanroom, AFM, SEM and profilometer. Tony Fitch in Lewis group at Caltech let me use their solar simulator before ours was set up. Rizal Hariadi in Winfree group at Caltech let me use their AFM when ours was out of order. Carol Garland in the TEM lab at Caltech helped me for mechanical polishing for the SIMS sample making. David Boyd in Mechanical Engineering and Liz Boyd in Geology and Planetary Sciences, both at Caltech, helped me for FTIR measurement. Guy DeRose in KNI lab at Caltech helped me for e-beam lithography. Hsin-Ying Chiu in Bockrath group at Caltech advised to me for thermal evaporation and e-beam lithography. Elvin Nixon, a project manager at Caltech, designed and conducted plumbing for various lab facilities. Frank Dimroth at Fraunhofer Institute in Germany grew the GaAs cells used in Chapter 7. Murray Bennett, Dave Carlson and Tim Koval at BP Solar provided calibration silicon solar cells for our solar simulator to us. Huynh Do, Steve Franz, Sumiko Hayashi and Jamie Jung at UCLA gave me technical assistance for chemical mechanical polishing.

I would like to also acknowledge the financial support from the Department of Energy, Basic Energy Sciences, ITO Foundation, Japan, NASA and NREL.

I thank my friends here at Caltech, particularly in the departments of Materials Science and Applied Physics and in Avery House. That was my great fun and refreshment to hang out with them to go for dinner, to beaches and mountains. My family in Japan also has been giving me a lot of support and encouragement for my graduate student life.

Finally, I would like to thank and acknowledge the professors at Caltech in my candidacy and thesis examination committees: Prof. Harry Atwater, Prof. Kaushik Bhattacharya, Prof. Marc Bockrath, Prof. Brent Fultz, Prof. Julia Greer and Prof. Nate Lewis.

Katsuaki Tanabe

May 2008

Pasadena, CA

Abstract

III-V compound multijunction solar cells enable ultrahigh efficiency performance in designs where subcells with high material quality and high internal quantum efficiency can be employed. However the optimal multijunction cell bandgap sequence cannot be achieved using lattice-matched compound semiconductor materials. Most current compound semiconductor solar cell design approaches are focused on either lattice-matched designs or metamorphic growth (i.e., growth with dislocations to accommodate subcell lattice mismatch), which inevitably results in less design flexibility or lower material quality than is desirable. An alternative approach is to employ direct bonded interconnects between subcells of a multijunction cell, which enables dislocation-free active regions by confining the defect network needed for lattice mismatch accommodation to tunnel junction interfaces.

We fabricated for the first time a direct-bond interconnected multijunction solar cell, a two-terminal monolithic GaAs/InGaAs dual-junction cell, to demonstrate a proof-of-principle for the viability of direct wafer bonding for solar cell applications. The bonded interface is a metal-free n^+GaAs/n^+InP tunnel junction with highly conductive Ohmic contact suitable for solar cell applications overcoming the 4% lattice mismatch. The quantum efficiency spectrum for the bonded cell was quite similar to that for each of unbonded GaAs and InGaAs subcells. The bonded dual-junction cell open-circuit voltage was equal to the sum of the unbonded subcell open-circuit voltages, which indicates that the bonding process does not degrade the cell material quality since any generated crystal defects that act as recombination centers would reduce the open-circuit voltage. Also, the

bonded interface has no significant carrier recombination rate to reduce the open circuit voltage.

Such a wafer bonding approach can also be applied to other photovoltaic heterojunctions where lattice mismatch accommodation is also a challenge, such as the InGaP/GaAs/InGaAsP/InGaAs four-junction tandem cell by bonding a GaAs-based lattice-matched InGaP/GaAs subcell to an InP-based lattice-matched InGaAsP/InGaAs subcell. Simple considerations suggest that for such a cell the currently-reported interfacial resistance of 0.12 Ohm-cm^2 would result in a negligible decrease in overall cell efficiency of ~0.02%, under 1-sun illumination.

Engineered substrates consisting of thin films of InP on Si handle substrates (InP/Si substrates or epitaxial templates) have the potential to significantly reduce the cost and weight of compound semiconductor solar cells relative to those fabricated on bulk InP substrates. InGaAs solar cells on InP have superior performance to Ge cells at photon energies greater than 0.7 eV and the current record efficiency cell for 1 sun illumination was achieved using an InGaP/GaAs/InGaAs triple junction cell design with an InGaAs bottom cell. Thermophotovoltaic (TPV) cells from the InGaAsP-family of III-V materials grown epitaxially on InP substrates would also benefit from such an InP/Si substrate. Additionally, a proposed four-junction solar cell fabricated by joining subcells of InGaAs and InGaAsP grown on InP with subcells of GaAs and AlInGaP grown on GaAs through a wafer-bonded interconnect would enable the independent selection of the subcell band gaps from well developed materials grown on lattice matched substrates. Substitution of InP/Si substrates for bulk InP in the fabrication of such a four-junction solar cell could

significantly reduce the substrate cost since the current prices for commercial InP substrates are much higher than those for Si substrates by two orders of magnitude. Direct heteroepitaxial growth of InP thin films on Si substrates has not produced the low dislocation-density high quality layers required for active InGaAs/InP in optoelectronic devices due to the ~8% lattice mismatch between InP and Si.

We successfully fabricated InP/Si substrates by He implantation of InP prior to bonding to a thermally oxidized Si substrate and annealing to exfoliate an InP thin film. The thickness of the exfoliated InP films was only 900 nm, which means hundreds of the InP/Si substrates could be prepared from a single InP wafer in principle. The photovoltaic current-voltage characteristics of the $In_{0.53}Ga_{0.47}As$ cells fabricated on the wafer-bonded InP/Si substrates were comparable to those synthesized on commercially available epi-ready InP substrates, and had a ~20% higher short-circuit current which we attribute to the high reflectivity of the InP/SiO_2/Si bonding interface. This work provides an initial demonstration of wafer-bonded InP/Si substrates as an alternative to bulk InP substrates for solar cell applications.

Metallic nanostructures can manipulate light paths by surface plasmons and can dramatically increase the optical path length in thin active photovoltaic layers to enhance photon absorption. This effect has potential for cost and weight reduction with thinned layers and also for efficiency enhancement associated with increased carrier excitation level in the absorber layer.

We have observed photocurrent enhancements up to 260% at 900 nm for a GaAs cell with a dense array of Ag nanoparticles with 150 nm diameter and 20 nm height deposited

through porous alumina membranes by thermal evaporation on top of the cell, relative to reference GaAs cells with no metal nanoparticle array. This dramatic photocurrent enhancement is attributed to the effect of metal nanoparticles to scatter the incident light into photovoltaic layers with a wide range of angles to increase the optical path length in the absorber layer.

GaAs solar cells with metallic structures at the bottom of the photovoltaic active layers, not only at the top, using semiconductor-metal direct bonding have been fabricated. These metallic back structures could incouple the incident light into surface plasmon mode propagating at the semiconductor/metal interface to increase the optical path, as well as simply act as back reflector, and we have observed significantly increased short-circuit current relative to reference cells without these metal components.

List of Related Publications

Journal Papers

K. Tanabe, K. Nakayama and H. A. Atwater

"Ultrathin GaAs solar cells with enhanced photocurrent via metallic nanoparticles and air/semiconductor/metal waveguide structures", in preparation.

K. Nakayama, K. Tanabe and H. A. Atwater

"Improved electrical properties of wafer bonded p-GaAs/n-InP interfaces with sulfide passivation"

J. Appl. Phys. **103** (9), 094503, 2008.

J. M. Zahler, K. Tanabe, C. Ladous, T. Pinnington, F. D. Newman and H. A. Atwater

"High efficiency InGaAs solar cells on Si by InP layer transfer"

Appl. Phys. Lett. **91** (1), 012108, 2007

"Exfoliation produces lighter, cheaper solar cells", New Scientist, July 2007

"Layer transfer cuts InP substrate cost", Compound Semiconductor, Sep. 2007

K. Tanabe, D. J. Aiken, M. W. Wanlass, A. Fontcuberta i Morral and H. A. Atwater

"Direct-bonded GaAs/InGaAs tandem solar cell"

Appl. Phys. Lett. **89** (10), 102106, 2006

Conference Talks and Proceedings

K. Tanabe*, K. Nakayama and H. A. Atwater

"Plasmon-enhanced Absorption and Photocurrent in Ultrathin GaAs Solar Cells with Metal Nanoparticle Arrays"

Proc. 33rd IEEE Photovoltaic Specialists Conference, San Diego, in press.

(Outstanding Student Paper/Presentation Award)

K. Tanabe*, K. Nakayama and H. A. Atwater

"Plasmonic GaAs Solar Cells: Absorption Enhancement by Metallic Nanostructures"

MRS Spring Meeting, San Francisco, KK 3.3, 2008

J. M. Zahler, K. Tanabe*, C. Ladous, T. Pinnington, F. D. Newman and H. A. Atwater

"Photocurrent Enhancement in $In_{0.53}Ga_{0.47}As$ Solar Cells Grown on $InP/SiO_2/Si$ Transferred Epitaxial Templates"

Proc. SPIE **6649**, San Diego, 664909, 2007

J. M. Zahler, K. Tanabe*, C. Ladous, T. Pinnington, F. D. Newman and H. A. Atwater

"InGaAs Solar Cells Grown on Wafer-Bonded InP/Si Epitaxial Templates"

MRS Spring Meeting, San Francisco, Y 1.9, 2007 (also in *Proc. MRS* **1012**, *Thin-Film Compound Semiconductor Photovoltaics - 2007*, 1012-Y01-09, 2007)

K. Tanabe*, D. J. Aiken, M. W. Wanlass, A. Fontcuberta i Morral and H. A. Atwater

"Lattice-mismatched Monolithic GaAs/InGaAs Two-junction Solar Cells by Direct Wafer Bonding"

Proc. IEEE 4th World Conference on Photovoltaic Energy Conversion, Waikoloa, 768, 2006

K. Tanabe*, D. J. Aiken, M. W. Wanlass, A. Fontcuberta i Morral and H. A. Atwater

"Direct-bond Interconnected Multijunction GaAs/InGaAs Solar Cell"

MRS Spring Meeting, San Francisco, FF 8.5, 2006

K. Tanabe*, A. Fontcuberta i Morral, D. J. Aiken, M. W. Wanlass and H. A. Atwater

"Low Resistance Ohmic GaAs/InP Bonded Heterojunctions for Lattice-mismatched Multijunction Solar Cell Applications"

Proc. 47th TMS Elect. Mat. Conf., Santa Barbara, S7, 2005

Contributed Conference Talks

K. Nakayama*, K. Tanabe and H. A. Atwater

"Surface Plasmon Enhanced Photocurrent in Thin GaAs Solar Cells"

Proc. SPIE, San Diego, in press.

K. Tanabe, M. J. Griggs, J. M. Zahler, D. C. Law, R. R. King, A. C. Ackerman, C. Ladous, T. Pinnington, F. D. Newman and H. A. Atwater*

"InGaAs/InP/Si and InGaP/GaAs/Ge/Si Solar Cells for Ultrahigh Efficiency Multijunction Solar Cells via Layer Transfer Fabrication"

Proc. DOE Solar Energy Technologies Program Review Meeting, Denver, 2007, in press. (invited)

M. J. Griggs*, K. Tanabe, D. C. Law, R. R. King and H. A. Atwater

"Developments for Four Junction Solar Cells based on Transferred Epitaxial Templates"

Proc. DOE Solar Energy Technologies Program Review Meeting, Denver, 49, 2005

H. A. Atwater*, M. J. Griggs, K. Tanabe, J. M. Zahler, A. Fontcuberta i Morral and S. Olson

"Ultrahigh Efficiency Microconcentrator PV"

3rd International Conference on Solar Concentrators for the Generation of Electricity or Hydrogen, Scottsdale, 2005

H. A. Atwater, M. J. Griggs*, K. Tanabe and J. M. Zahler

"Layer Transfer Processes for Lattice-Mismatched Compound Semiconductor Heterostructure Solar Cells"

16th American Conference on Crystal Growth and Epitaxy / 12th US Biennial Workshop on Organometallic Vapor Phase Epitaxy, Big Sky, 2005 (invited)

H. A. Atwater*, M. J. Griggs, A. Fontcuberta i Morral, K. Tanabe and J. M. Zahler

"Wafer-scale Fabrication of Ge/Si and InP/Si for Multijunction Solar Cell Applications"

Proc. DOE Solar Energy Technologies Program Review Meeting, Denver, 196, 2004

Table of Contents

List of Figures

List of Tables

Chapter 1 Introduction

1-1. Global crisis and Solar cells

The current world's consumption of electric energy is around 12-13 TW and the earth receives more solar energy in 1 hour than is the energy used in 1 year globally, considering the solar constant 1.7 x 10^5 TW at the top of the earth's atmosphere. [1] However the solar energy incidence, around 1 kW/m^2, is quite dilute and requires vast area of energy converters to meet the world's energy consumption. Therefore high efficiency solar energy conversion is crucial. Solar cells, also called *photovoltaics*, are devices converting the energy of the sunlight into electricity by the photovoltaic effect discovered by the French scientist Henri Becquerel in 1839. Electron-hole pairs are generated by the energy of the incident photons overcoming the energy bandgap of the photovoltaic material to make a current flow according to the built-in potential slope, typically with a p-n junction of semiconductor, in the material, as schematically depicted in Figure 1.1. Solar cells have been recognized as an important alternative power source especially since the 1970s oil crises. Solar cells are also promising as a carbon-free energy source to suppress the global warming.

The energy conversion efficiency of a solar cell is defined as the ratio of the electric power generated by the solar cell to the incident sunlight energy into the solar cell per time. Currently the highest reported cell efficiencies in laboratories are around 40% while the energy conversion efficiencies for thermal power generation can exceed 50%. This fact however never means the superiority of thermal generation since its resources such

as fossil fuels are limited while the solar energy is essentially unlimited. The incident energy flux spectrum of sunlight for reported solar cell efficiencies is standardized as some specifically defined spectra such as Air Mass 0 (AM0), Air Mass 1.5 Global and Direct (AM1.5G and AM1.5D). [2-4] Figure 1.2 shows the AM1.5G spectrum, most commonly referred for terrestrial-use solar cells under non-concentrated sunlight spectrum measurements. The solar spectrum widely ranges through 300 nm to 2000 nm with its peak around at 500-600 nm and a large fraction stems from the visible range. The dips prominently observed around at 1100 nm, 1400 nm etc. are due to the absorption mainly by CO_2 and H_2O in the atmosphere. The energy fraction of the solar spectrum utilized by an ideal single-junction solar cell with an energy bandgap of 1.4 eV determined by the *detailed balance* calculation based on thermodynamics considering recombination loss of carriers (electron-hole pairs) proposed by Shockley and Queisser [5] is shown in Figure 1.2. The area ratio of this energy generation spectrum by the solar cell to the solar irradiation spectrum corresponds to the energy conversion efficiency and is 31% in this case.

Concentration of sunlight into smaller incident area using lenses has two advantages for solar cell applications. The first is the material cost reduction with smaller area of cells required to generate the same amount of energy. The second is the efficiency enhancement with the higher open-circuit voltage determined by the ratio of the photocurrent to the recombination current. However, too much sunlight concentration would rather reduce the open-circuit voltage with increased temperature and also induce significant power loss by the series resistance. There is therefore an optimized

concentration factor for each solar cell. Although this thesis will not discuss the detail of concentrators, interested readers can refer Ref. 6-8.

Solar cells made of III-V semiconductor compounds have been exhibiting the leading energy conversion efficiencies rather than the other materials represented by silicon. [9] Besides the potential for high efficiency, III-V semiconductor compound materials have advantages including the bandgap tunability by elemental compositions, higher photon absorption by the direct bandgap energies, higher resistivity against high-energy rays in space, and smaller efficiency degradation by heat than Si solar cells. The energy conversion efficiencies of III-V solar cells are steadily increased year by year and approaching 40% for the laboratory-scale cells as seen in Figure 1.3. [10] A lot of efforts have been made to date to improve the cell performance further for the purpose of the development of space activities and the solution for the upcoming energy crisis and global environmental issues.

1-2. Developments of multijunction III-V semiconductor compound solar cells

Here I describe the principle, history and recent developments of multijunction III-V solar cells in this section. One of the major factors of energy loss in a solar cell is the gap between the photon energy and the bandgap energy of the photovoltaic material. No absorption would occur if the photon energy was smaller than the bandgap energy and merely the part equal to the bandgap energy out of the photon energy could be extracted as electric power leaving the other part wasted as heat if larger. Multistacking of photovoltaic materials of different bandgap energies is therefore commonly used for high

efficiency III-V solar cells to reduce this energy loss and absorb the photon energy from the sunlight spectrum more widely and efficiently, taking advantage of the tunability of bandgap energies and lattice constants with the compositions of III-V semiconductor compounds, called multijunction or tandem cells. The theoretical efficiency limit based on the *detailed balance* calculation estimated by Henry shows that a 36-gap or -junction cell ideally could reach 72% efficiency at a concentration of 1000 suns relative to the 37% for a 1-gap cell. (Figure 1.4) [11] A theoretical calculation for the ideal efficiencies according to the bandgap energy combinations of the top and bottom semiconductor materials in two-junction (2J) solar cells are shown in Figure 1.5. [12] Similar calculations under different conditions are found in Ref. 13 and 14.

For multijunction cells, monolithic or two-terminal structures are generally favored and used rather than expensive and impractical three- or four-terminal structures. [15] A schematic cross-sectional diagram of a monolithic 3J solar cell structure is shown in Figure 1.6. [16] Multijunction solar cells have been layered by epitaxial growth generally with metalorganic chemical vapor deposition (MOCVD) requiring lattice matching among the stacked semiconductor materials. [17-20] Figures 1.7 and 1.8 show the relation between the lattice constants and the bandgap energies for commonly used III-V semiconductor compounds.

One of the most common and highest efficiency two 2J cells consists of a combination of $In_{0.48}Ga_{0.52}P$ and GaAs with the same lattice constant of 5.64 A and the bandgap energy of 1.86 eV and 1.42 eV, respectively. [22-24] This InGaP/GaAs cell has the

highest efficiency of 30.3% under AM1.5G solar spectrum with 1-sun intensity (100 mW cm^{-2}) among monolithic 2J cells [9, 24], while 4-terminal configuration allowed the highest 2J efficiency of 32.6% under AM1.5D spectrum at 100 suns for a lattice-mismatched GaAs/GaSb stack (GaSb: 6.09 A, 0.70 eV). [25]

For 3J cells, most commonly so far, a Ge bottom cell is added to the InGaP/GaAs 2J cell to form an InGaP/GaAs/Ge structure for Ge's lattice constant of 5.66 A nearly equal to that of InGaP/GaAs. This 3J structure is grown on a Ge substrate and an advantage that Ge is a cheaper and mechanically stronger material than GaAs relative to cells grown on GaAs substrates. The current formally-reported highest efficiency solar cell (as of May, 2008) is actually an InGaP/GaAs/Ge 3J cell with the efficiency of 40.7% at 240 suns under AM1.5D. [26, 27] However, it should be noted that the 0.66 eV bandgap energy of Ge is not optimal as the material for the bottom cell in a 3J cell. This point will be discussed in the following section.

Specifically for the space use, very thin, light and flexible InGaP/GaAs 2J and InGaP/GaAs/Ge 3J cells are being developed recently. [28-30] Figure 1.9 shows a photograph of a flexible InGaP/GaAs 2J device. [30] Although the fabrication processes have not been well disclosed, the photovoltaic layers are attached to metal or polymer supporting films and the parent substrates for the epitaxial growth are removed somehow. For further improvement of the cell efficiency, cells with more junctions are being proposed such as an InGaP/GaAs/InGaAsN/Ge 4J structure. [31] Recently an (Al)InGaP/InGaP/Al(In)GaAs/(In)GaAs/InGaAsN/Ge 6J cell has been demonstrated. [32] The efficiency of this 6J cell was 23.6% under AM0 at 1 sun (135 mW cm^{-2}). (Note

that the intensities of 1 sun for AM1.5 and AM0 are different. See Ref. 4 and 33 for the detail of the standard artificial solar spectra for cell measurements.) This efficiency is much lower than the highest efficiency 3J cell regardless of more number of junctions presumably due to the current-limiting InGaAsN layer with low quantum efficiency. The open-circuit voltage of this 6J cell was however 5.33V, significantly higher than the 3.09 V of the highest efficiency 3J cell, simply because of the series connection of six semiconductor materials.

1-3. 1.0 eV bandgap subcells

Here I briefly review the fabrication and characteristics of the materials with bandgap energies around 1.0 eV, one of the most critical issues for the further development of III-V multijunction cells in the near future, in this section. The optimal bandgap energy for the bottom cells in 3J solar cells is known to be around 1.0 eV considering the current matching among three subcells, assuming the top two-junction structure is the InGaP/GaAs. [34] Therefore materials of ~1.0 eV bandgap lattice-matched to GaAs and Ge are intensively searched these days. As well as replacing the Ge subcell with a 1.0 eV bandgap material, insertion of a 1.0 eV material between the GaAs and Ge subcells would also improve the efficiency. Such a 4J cell could exhibit an efficiency higher than 50% theoretically. [35] It should be noted that another way to improve the efficiency from the InGaP/GaAs/Ge 3J cell is to increase the bandgap of the InGaP subcell by adding Al. However the addition of Al induces a significant reduction of the photocurrent of the InGaP cell probably due to the adverse effect of Al and the associated oxygen contamination on minority-carrier properties. [36] Lowering the bandgap of the GaAs

middle cell by substituting a portion of the Ga content with In is also a way for higher efficiency than the InGaP/GaAs/Ge 3J cell, although this approach accompanies lattice mismatch and requires graded buffer layers or suffers from large density of dislocations otherwise. [37, 38]

$In_xGa_{1-x}As_{1-y}N_y$ can be lattice matched to GaAs for compositions satisfying $x = 3y$ and can have a bandgap of ~1.0 eV. [39] Although this InGaAsN has been thought to be the most promising candidate, its minority carrier diffusion length has been too short resulting low output photocurrent. [40-42] Other candidates such as $ZnGeAs_2$, $GaTlP_2$ and InGaAsB have not shown very promising properties either. [15]
Sb has been recently incorporated in the nitride system to form InGaAsNSb cells lattice-matched to GaAs with 0.92 eV bandgap and demonstrated relatively high quantum efficiency and current density enough for current-matching to the InGaP/GaAs cell. [43] The open-circuit voltage was however quite low and it is unclear if this InGaAsNSb would be better than Ge.

An alternative is a 1.0 eV InGaAs material lattice-mismatched to GaAs with graded compositions in epitaxial growth. [44] A ~1 eV InGaAs subcell lattice-mismatched to GaAs by 2.2% was grown on an inversely grown GaAs/InGaP 2J subcell via transparent compositionally graded layers. This epitaxial structure was mounted to a pre-metallized Si supporting wafer and then the parent GaAs substrate was selectively removed resulting an InGaP/GaAs/InGaAs 3J cell. This inversely grown cell achieved a 38.9% efficiency

under AM1.5D at 81 suns and also the highest efficiency (as of May, 2008) for AM1.5G, 1-sun condition of 33.8%. [45-47]

1-4. Outline of Thesis

In this chapter I described the importance of the photovoltaic devices or solar cells, the motivation of this study. In Chapter 2, I will introduce the wafer bonding technologies and their applications. In Chapter 3, I will describe my experiment for wafer bonding of GaAs and InP wafers as a preparation of the direct-bonded multijunction solar cells. In Chapter 4, the fabrication and characterization of lattice-mismatched GaAs/InGaAs solar cells via direct wafer bonding technique will be shown. In Chapter 5, the introduction and experiments for InP layer transfer onto Si for III-V solar cell cost reduction will be given. In Chapter 6, the fabrication and characterization of InGaAs solar cells grown on the prepared layer-transferred InP/Si low-cost alternative epitaxial substrates will be described. In Chapter 7, the development of GaAs “plasmonic” solar cells with metallic nanostructures for absorption enhancement will be described. This thesis will end with Chapter 8, conclusions and future outlook.

1-5. References

[1] A. J. Nozik, *Inorg. Chem.* **44**, 6893 (2005).

[2] K. Emery and C. Osterwald, *Sol. Cells* **17**, 253 (1986).

[3] S. Nann and K. Emery, *Sol. Energy Mater.* **27**, 189 (1992).

[4] K. Emery, in *Handbook of Photovoltaic Science and Engineering*, edited by A. Luque and S. Hegedus (Wiley, New York), Chap. 16 (2003).

[5] W. Shockley and H. J. Queisser, *J. Appl. Phys.* **32**, 510 (1961).

[6] P. Campbell and M. A. Green, *IEEE Trans. Electron. Dev.* **33**, 234 (1986).

[7] V. Andreev et al, *Photovoltaic Conversion of Concentrated Sunlight* (Wiley, New York) (1997).

[8] R. M. Swanson, in *Handbook of Photovoltaic Science and Engineering*, edited by A. Luque and S. Hegedus (Wiley, New York), Chap. 11 (2003).

[9] M. A. Green et al, *Prog. Photovolt. Res. Appl.* **13**, 387 (2005).

[10] T. Surek, *J. Cryst. Growth* **275**, 292 (2005).

[11] C. H. Henry, *J. Appl. Phys.* **51**, 4494 (1980).

[12] H. Takakura, *Jpn. J. Appl. Phys.* **31**, 2394 (1992).

[13] S. R. Kurtz et al, *J. Appl. Phys.* **68**, 1890 (1990).

[14] A. W. Bett et al, *Appl. Phys. A* **69**, 119 (1999).

[15] J. M. Olson et al, in *Handbook of Photovoltaic Science and Engineering*, edited by A. Luque and S. Hegedus (Wiley, New York), Chap. 9 (2003).

[16] K. Nishioka et al, *Jpn. J. Appl. Phys.* **43**, 882 (2004).

[17] M. Sugo et al, *J. Appl. Phys.* **68**, 540 (1990).

[18] R. D. Dupuis, *IEEE J. Select. Top. Quant. Elect.* **6**, 1040 (2000).

[19] Y. Shimizu and Y. Okada, *J. Cryst. Growth* **265**, 99 (2004).

[20] Y. Li et al, *Phil. Mag.* **85**, 3073 (2005).

[21] S. Tiwari and D. J. Frank, *Appl. Phys. Lett.* **60**, 630 (1992).

[22] J. M. Olson et al, *Appl. Phys. Lett.* **56**, 623 (1990).

[23] K. A. Bertness et al, *Appl. Phys. Lett.* **65**, 989 (1994).

[24] T. Takamoto et al, *Appl. Phys. Lett.* **70**, 381 (1997).

[25] L. M. Fraas et al, *Proc. 21st IEEE Photovoltaic Specialists Conference*, Kissimimee, 190 (1990).

[26] R. R. King et al, *Proc. 4th International Conference on Solar Concentrator*, El Escorial (2007).

[27] R. R. King et al, *Appl. Phys. Lett.* **90**, 183516 (2007).

[28] T. Takamoto et al, *Proc. 31st IEEE Photovoltaic Specialists Conference*, Lake Buena Vista, 519 (2005).

[29] D. C. Law et al, *Proc. IEEE 4th World Conference on Photovoltaic Energy Conversion*, Waikoloa, 1879 (2006).

[30] T. Takamoto et al, *Proc. IEEE 4th World Conference on Photovoltaic Energy Conversion*, Waikoloa, 1769 (2006).

[31] N. H. Karam et al, *Sol. Ener. Mater. Sol. Cell.* **66**, 453 (2001).

[32] R. R. King et al, *Proc. IEEE 4th World Conference on Photovoltaic Energy Conversion*, Waikoloa, 1757 (2006).

[33] D. R. Myers et al, *Proc. 28th IEEE Photovoltaic Specialists Conference*, Anchorage, 1202 (2000).

[34] D. J. Friedman et al, *Proc. IEEE 2nd World Conference on Photovoltaic Energy Conversion*, Vienna, 3 (1998).

[35] S. R. Kurtz et al, *Proc. 26th IEEE Photovoltaic Specialists Conference*, Anaheim, 875 (1997).

[36] R. R. King et al, *Proc. 28th IEEE Photovoltaic Specialists Conference*, Anchorage, 998 (2000).

[37] R. R. King et al, *Proc. IEEE 4th World Conference on Photovoltaic Energy Conversion*, Waikoloa, 760 (2006).

[38] F. Dimroth et al, *IEEE Electron. Dev. Lett.* **21**, 209 (2000).

[39] M. Kondow et al, *Jpn. J. Appl. Phys.* **35**, 1273 (1996).

[40] J. F. Geisz et al, *J. Cryst. Growth* **195**, 401 (1998).

[41] D. J. Friedman et al, *J. Cryst. Growth* **195**, 409 (1998).

[42] S. R. Kurtz et al, *Appl. Phys. Lett.* **74**, 729 (1999).

[43] D. B. Jackrel et al, *J. Appl. Phys.* **101**, 114916 (2007).

[44] M. W. Wanlass et al, *Proc. 31st IEEE Photovoltaic Specialists Conference*, Lake Buena Vista, 530 (2005).

[45] M. W. Wanlass et al, *Proc. International Conference on Solar Concentrators for the Generation of Electricity or Hydrogen*, Scottsdale (2005).

[46] M. W. Wanlass et al, *Proc. IEEE 4th World Conference on Photovoltaic Energy Conversion*, Waikoloa, 729 (2006).

[47] J. F. Geisz et al, *Appl. Phys. Lett.* **91**, 023502 (2007).

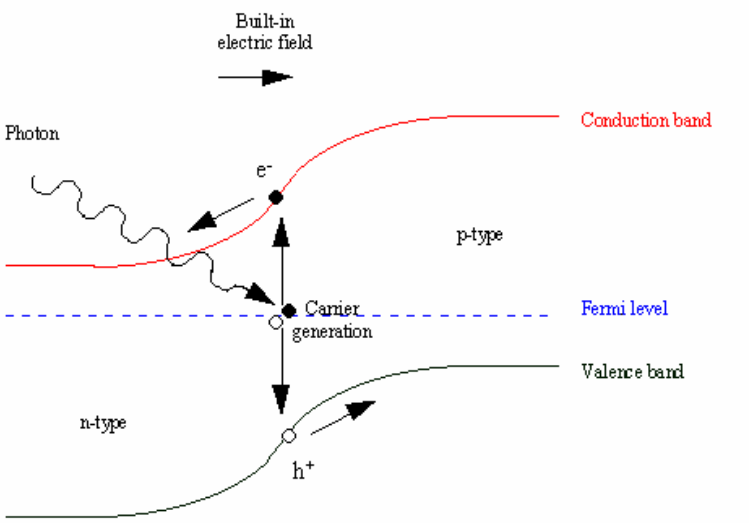

Fig. 1.1 Schematic diagram of the work principle of photovoltaic devices or solar cells. Electrical current is generated from charge carriers (electrons and holes) excited by incident light flowing directed by the potential slope built by a p-n junction in a semiconductor.

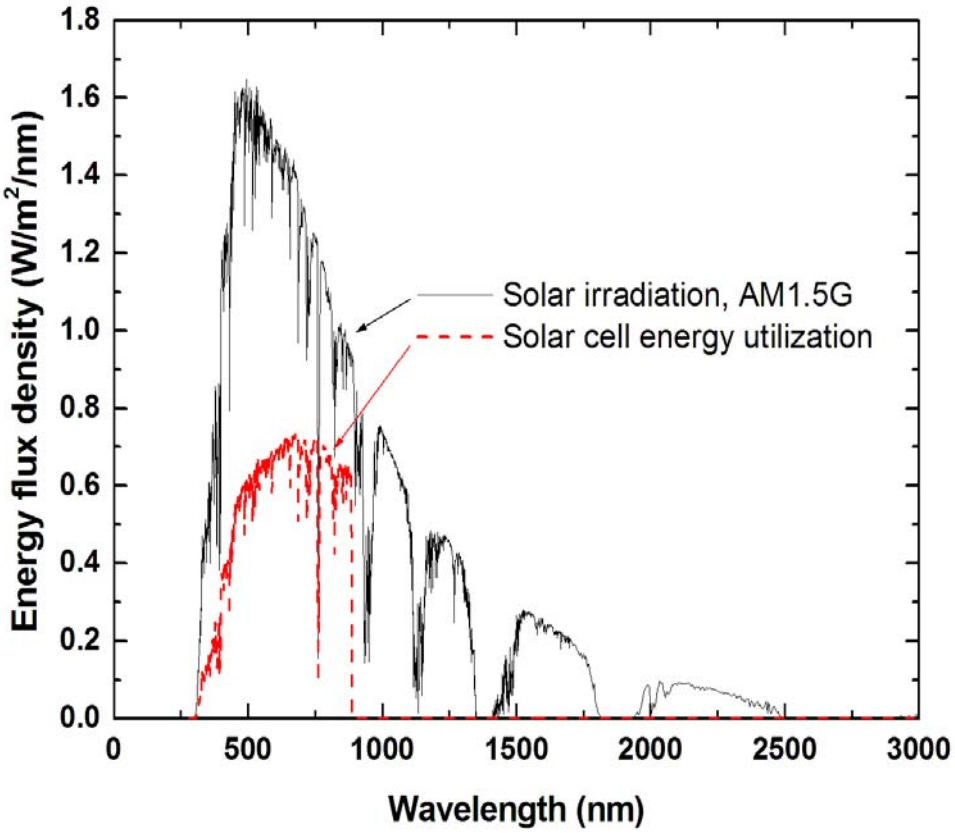

Fig. 1.2 Solar irradiation spectrum of AM1.5G and energy utilization spectrum by a single-junction solar cell with an energy bandgap of 1.4 eV.

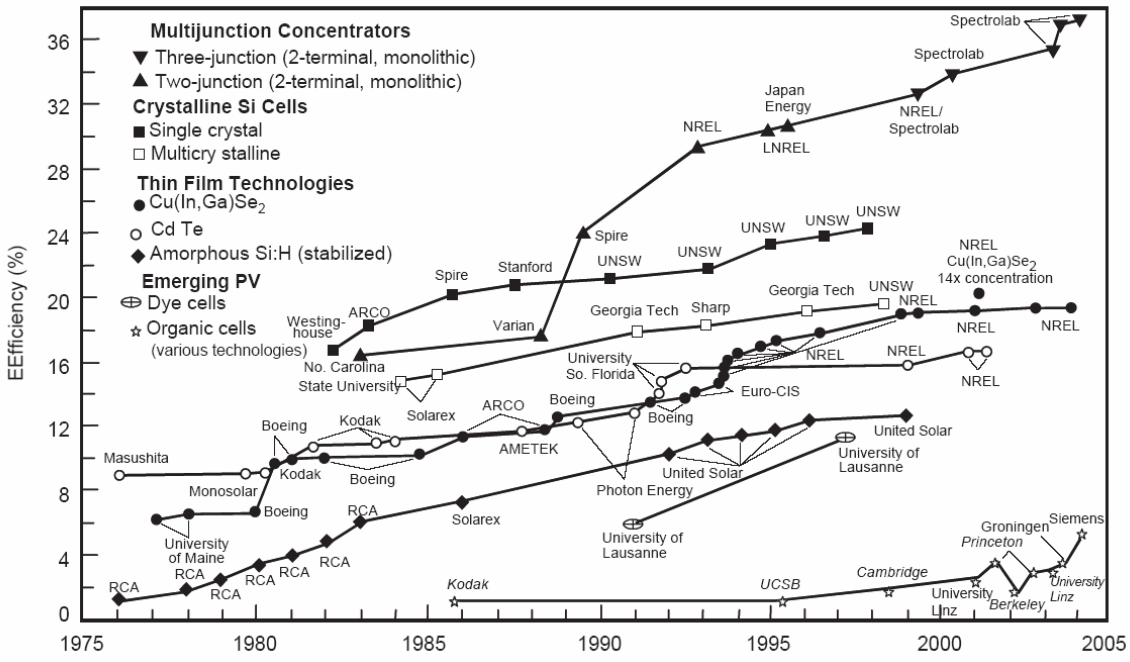

Fig. 1.3 Chronological record energy-conversion efficiencies of solar cells. (from Ref. 10)

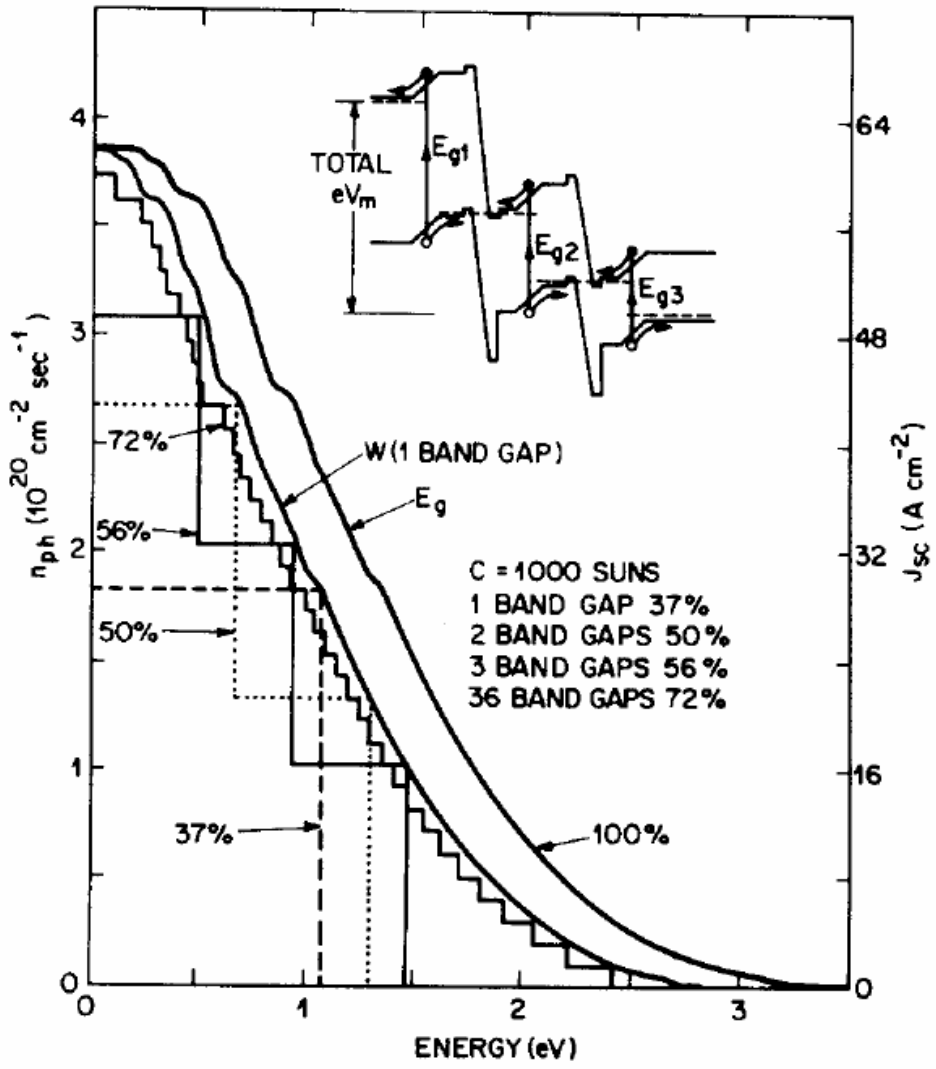

Fig. 1.4 Graphical analysis of the efficiencies of 1, 2, 3 and 36 energy gap solar cells. The step heights equal to the photon flux absorbed, n_{ph}, by each energy gap and the step widths (measured from the origin) equal to the maximum energy per absorbed photon, delivered to the load. The efficiency of each cell is given by the ratio of the area enclosed by steps and the area under the outer curve, labeled 100%. (from Ref. 11)

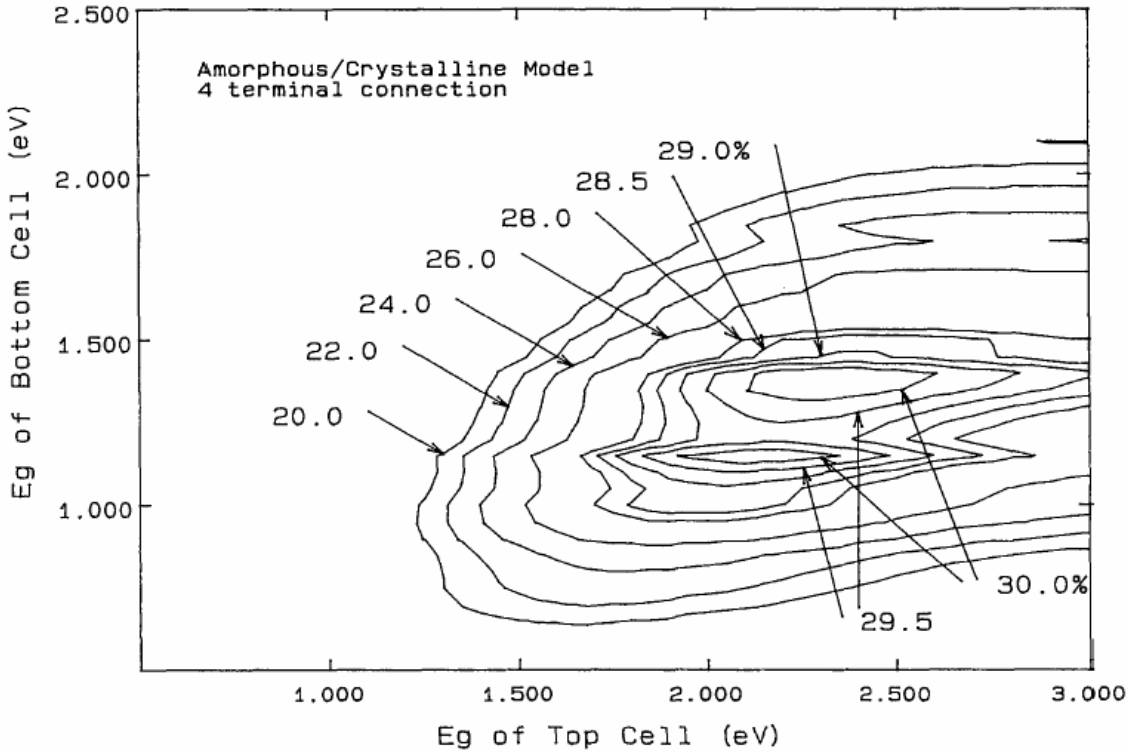

Fig. 1.5 Calculated isoefficiency map for two-junction four-terminal solar cells under AM1.5G spectrum at one-sun illumination according to the top and bottom cell bandgaps. (from Ref. 12)

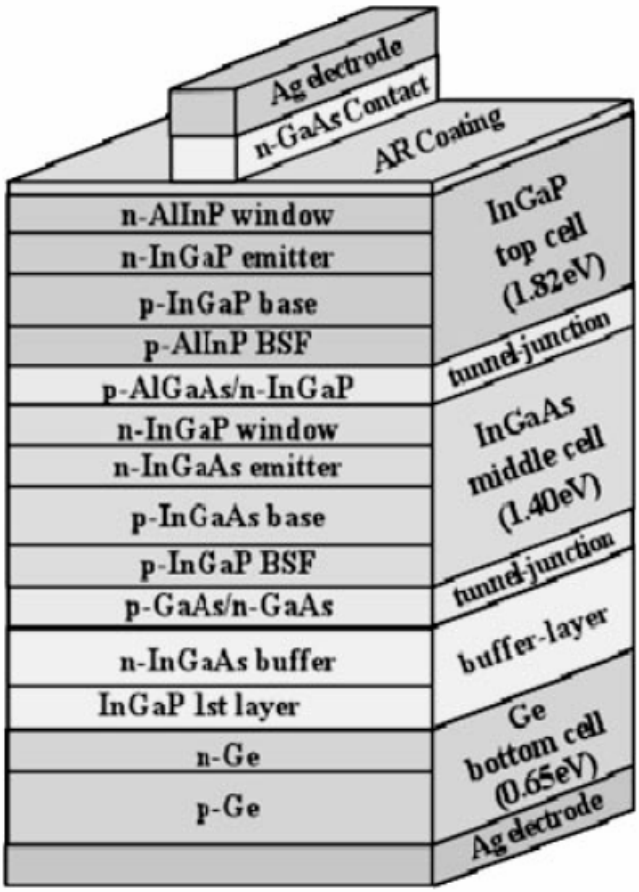

Fig. 1.6 Cross-sectional schematic of a three-junction cell structure. (from Ref. 16)

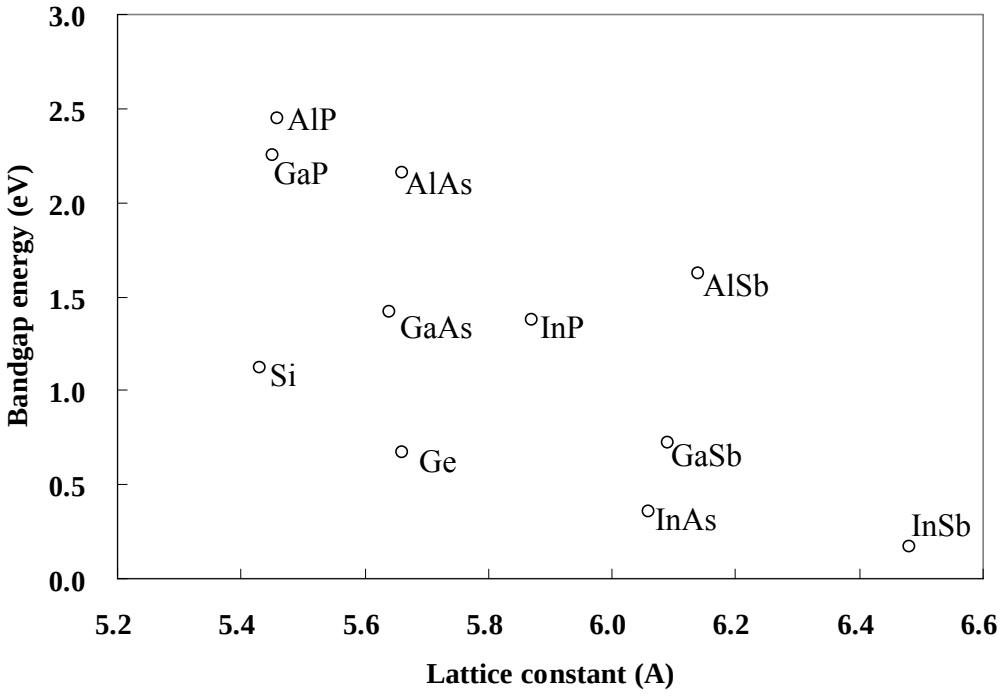

Fig. 1.7 Bandgap energies plotted as a function of the lattice constant of semiconductors.

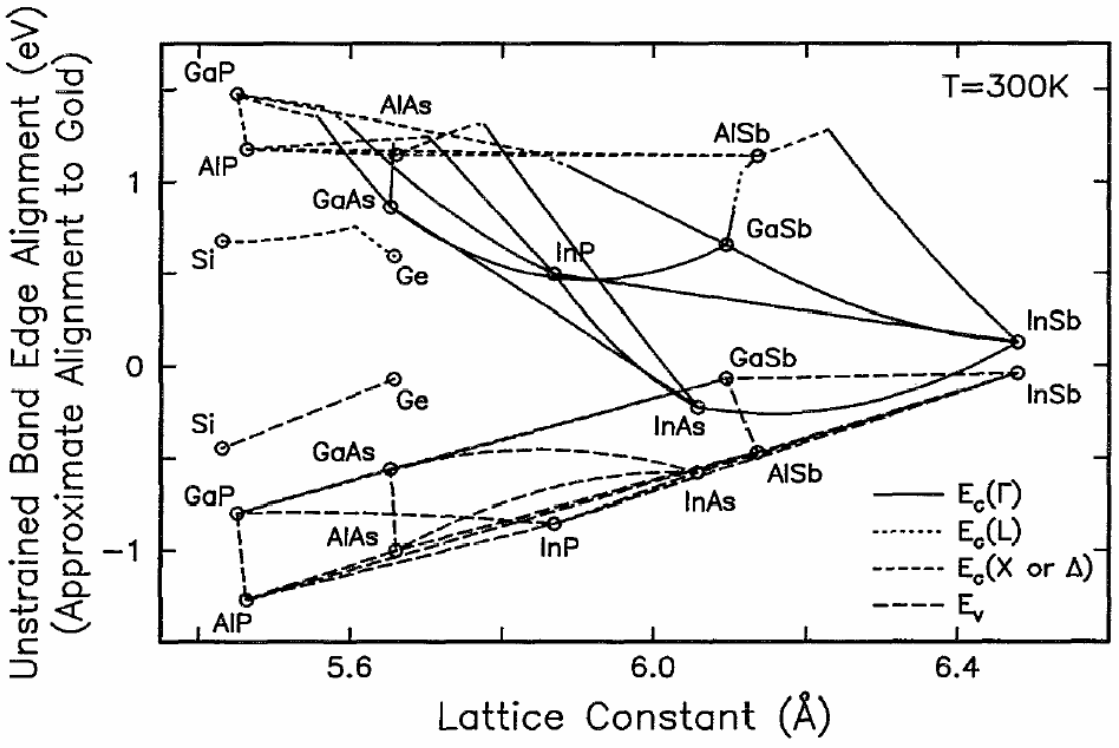

Fig. 1.8 Conduction band edge and valence band edge energies plotted as a function of the lattice constant of semiconductors. The zero energy point represents the approximate gold Schottky barrier position in the band gap of any given alloy. (from Ref. 21)

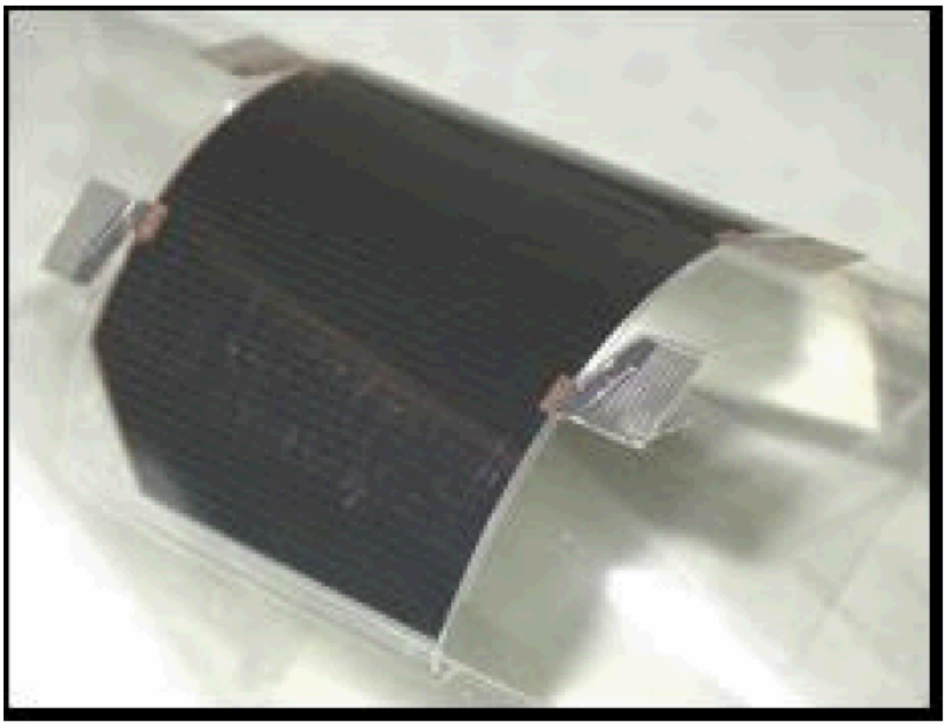

Fig. 1.9 Photograph of a flexible thin-film InGaP/GaAs two-junction 4x7-cm^2 film-laminated cell. (from Ref. 30)

Chapter 2 Wafer bonding for solar cell applications

2-1. Introduction

In the previous chapter, multijunction solar cells for high efficiency energy conversion were introduced. In this chapter, we will look into more detail or learn what kind of materials stacking would make multijunction solar cells more efficient. To do that, we use the "detailed balance limit calculation", a method to estimate the thermodynamical limit of solar energy conversion, to determine ideal bandgap combinations. We will recognize that release of the lattice matching restriction among the stacking materials would give us significant improvement of efficiency. As a way to overcome the lattice mismatch, the wafer bonding technique is introduced as a method to stack semiconductor materials compared with the conventional epitaxial growth.

2-2. Ideal lattice-mismatched multijunction solar cells, detailed balance limit calculation

In the previous chapter, I mentioned multijunction solar cells can exhibit higher energy conversion efficiencies rather than single-junction cells. In this section, let's estimate what kind of combinations of semiconductor materials with bandgap energies can ideally achieve how much energy conversion efficiencies. To do that, here I will use the "detailed balance limit" calculation method developed by Shockley and Queisser. [1] The "detailed balance limit" represents the thermodynamical energy conversion efficiency limit of solar cells taking black-body radiation into account. See References 1 and 2 for the detail of the theory and formalism. The radiative current density J_{rad} can be written as

$$J_{rad} = e\int_{Ec/\hbar}^{\infty} d\omega \int d\Omega \cos\theta \rho_{rad} v_g \,, \quad \text{(Eq. 1)}$$

where the radiation density ρ_{rad} is given by

$$\rho_{rad} \cong \frac{1}{4\pi}\frac{k^2}{v_g}\exp\left(\frac{eV-\hbar\omega}{kT}\right). \quad \text{(Eq. 2)}$$

T represents the temperature of the solar cell and was assumed to be 300 K in this Thesis, as in References 1 and 2. Considering the total reflection at the top surface of the active region, the angular integral in Eq. 1 becomes

$$\int d\Omega \cos\theta = \pi\left(1 + 1/n^2\right), \quad \text{(Eq. 3)}$$

where n is the refractive index of the active region, and J_{rad} becomes

$$J_{rad} = \frac{e\left(n^2+1\right)}{4\pi^2 c^2}\int_{Ec/\hbar}^{\infty} \omega^2 \exp\left(\frac{eV-\hbar\omega}{kT}\right) d\omega \cong A\exp\left(\frac{eV-E_g}{kT}\right), \quad \text{(Eq. 4)}$$

where

$$A \equiv \frac{e\left(n^2+1\right)E_g{}^2 kT}{4\pi^2\hbar^3 c^2}. \quad \text{(Eq. 5)}$$

The current density to the load is

$$J \cong J_{ph} - J_{rad} = J_{ph} - A\exp\left(\frac{eV - E_g}{kT}\right), \quad \text{(Eq. 6)}$$

where J_{ph} is the carrier generation flux and

$$J_{ph} = \int Q(\lambda) I_S(\lambda) d\lambda, \quad \text{(Eq. 7)}$$

where

$$Q(\lambda) = \frac{E_g}{E_S(\lambda)} \quad \left(E_S(\lambda) \geq E_g\right)$$

$$= 0 \quad \left(E_S(\lambda) < E_g\right), \quad \text{(Eq. 8)}$$

where λ is the corresponding wavelength of sunlight, $I_S(\lambda)$ is the incident energy flux density of the solar irradiation, the energy utilization factor $Q(\lambda)$ is the fraction of the incident energy flux used to excite electron-hole pairs, E_g is the energy bandgap of the solar cell material, and $E_S(\lambda) = hv$ is the energy of the photons with the wavelength of λ. Setting $J = 0$ in Eq. 6, the open-circuit voltage is

$$eV_{oc} = E_g - kT \ln\left(\frac{A}{J_{ph}}\right). \quad \text{(Eq. 9)}$$

The voltage at the maximum power point is found by setting the derivative *d(JV)/dV = 0*.

$$eV_m = eV_{oc} - kT \ln\left(1 + \frac{eV_m}{kT}\right) \quad \text{(Eq. 10)}$$

Solving this transcendental equation for V_m, the current density at the maximum power point, J_m, is obtained by

$$J_m = \frac{J_{ph}}{1 + kT / eV_m}. \quad \text{(Eq. 11)}$$

Finally the solar cell efficiencies are calculated by

$$\eta = \frac{J_m V_m}{\int I_S(\lambda) d\lambda}. \quad \text{(Eq. 12)}$$

Air Mass 1.5 Global solar spectrum (AM1.5G) was used as $I_S(\lambda)$ for the cases of 1-sun irradiation intensity. Air Mass 1.5 Direct solar spectrum (AM1.5D) was used for concentration cases considering only direct incidence of the sunlight, not scattered photons, as appropriate for optical concentrators.

Figure 2.1 shows the solar irradiation spectrum, $I_S(\lambda)$, and the calculated energy utilization spectrum by a single-junction solar cell with the optimized E_g to maximize η under 1-sun and concentration illumination. Ratio of the integral of the energy utilization spectrum for the solar cell to the integral of the solar irradiation spectrum corresponds to the energy conversion efficiency, η, of the solar cell. The obtained η for the cell, 31.3% for 1 sun and 37.6% for 1000 suns, are quite consistent with the results presented in Ref. 1 and 2.

Figure 2.2 shows an example of the solar irradiation spectrum, $I_S(\lambda)$, and the calculated energy utilization spectrum by a four-junction solar cell for 1-sun illumination. The bandgap energies were randomly picked and current matching among subcells was not considered here. Again, note that the ratio of the integral of the energy utilization spectrum for the solar cell to the integral of the solar irradiation spectrum corresponds to the energy conversion efficiency, η, of the solar cell. In this four-junction cell case, η reaches ~50%. We see here that multijunction solar cells can collect solar energy more efficiently than single-junction cells do.

First, I investigated (Al)InGaP/GaAs/3rd subcell triple junction solar cells since $In_{0.5}Ga_{0.5}P$/GaAs dual-junction (2J) cells are known to be the most efficient monolithic 2J cells, as I described in the previous chapter. Figure 2.3 shows the dependence of the computed detailed balance limit efficiency on the bandgap energy of the 3rd subcell under a 100-sun illumination. It is found that as the bandgap energy of the bottom subcell goes up, the efficiency could go even higher than the case of Ge, because of higher

photovoltage while the photocurrent is limited by the top subcells. The calculated detailed balance limit efficiency reaches 50.5% with a 3rd subcell with a bandgap energy of 1.02 eV, relative to 45.6% with a Ge 3rd subcell. Note again that the current (as of May, 2008) solar cell efficiency record is 40.7% with an InGaP/GaAs/Ge triple-junction cell under a 240-sun illimination. [3]

Furthermore, if we could make a (Al)InGaP/GaAs/3rd subcell/4th subcell four-junction solar cell, the efficiency could be even higher. Figure 2.4 shows a contour plot of four-junction cell efficiencies depending on the bandgap energies of the 3rd and 4th subcells. [4] We see that certain combination of the bandgap energies of the bottom two subcells would lead up to ~55% efficiency. Given a 4th subcell of $In_{0.53}Ga_{0.47}As$ lattice matched to InP (Eg = 0.74 eV), I calculated the maximum efficiency to be 51.4% with the optimized 3rd subcell bandgap energy of 1.06 eV.

So far we only have looked at series connection, but the calculated maximum efficiency reaches 55.7%, as shown in Figure 2.5, for the same (Al)InGaP/GaAs/3rd subcell/InGaAs four-junction solar cell with the optimized 3rd subcell bandgap energy of 1.06 eV assuming independent connection of the top dual-junction and the bottom dual-junction.

However, it is not trivial to fabricate these types of triple or four-junction III-V semiconductor compound solar cells due to the issue of lattice mismatch among materials. Figure 2.6 shows a plot of lattice constants and bandgap energies for commonly used III-V semiconductor compounds, which specifically shows a lattice mismatch between top

subcells such as (Al)InGaP and GaAs and bottom subcells such as InGaAsP and InGaAs. Figure 2.7 shows cross-sectional transmission electron microscopy (TEM) images for the interface of grown layers and substrates with lattice mismatch for common III-V semiconductor compound materials. [5, 6] These images indicate that even a lattice mismatch of a couple of percent generates a significant density of threading dislocations, which would degrade the performance of photovoltaic devices by acting as carrier recombination centers.

2-3. Wafer bonding technology for solar cell applications

2-3-1. What is wafer bonding ?

Wafer bonding is a technique to form a homo- or hetero-junction by bonding two materials. There are two types of wafer bonding schemes. One is direct wafer bonding with no additional bonding layer between the two materials you want to get together. The other is bonding via some bonding layers such as semiconductor oxides, metals or adhesive polymers to enhance the bonding strength. To the best of my knowledge, direct wafer bonding was first proposed and demonstrated by Shimbo et al [7] as a method to form an abrupt p-n junction of silicon diode. They joined two mirror-polished Si wafers and annealed the pairs to found that the bonding interfacial strength increases with increasing temperature at above 300 ^{o}C to reach a fracture strength of bulk silicon (100 - 200 kg/cm^{2}) at 1000 ^{o}C.

Presence of dislocations brings us undesirable effects on electronic performance of semiconductor materials, serving as easy diffusion paths for dopants or as recombination

centers to diminish carrier density in devices. [8] Therefore, controlling structural defects by misfit strain is an important issue.

Wafer bonding, which makes a heterostructure from a pair of crystalline wafers, can avoid threading dislocations confining all of the dislocations at the heterointerface. Because only the atoms very close to the interface participate in the reaction, the rest of the material is not affected by the bonding process and no defects can propagate into the layers. In other words, we can operate a wafer bonding process at a temperature where covalent bonds across the heterointerface form but the thermal fluctuation cannot overcome the kinetic barrier for the advance of threading dislocations. Somehow low temperature does not allow strain relaxation by generation of threading dislocations which is thermodynamically preferred, but leaves the structure at a metastable state.

2-3-2. Mechanics in wafer bonding

Wafer bonding, which makes a heterostructure from a pair of crystalline wafers, can avoid threading dislocations confining all of the dislocations at the heterointerface. Because only the atoms very close to the interface participate in the reaction, the rest of the material is not affected by the bonding process and no defects can propagate into the layers. In other words, we can operate a wafer bonding process at a temperature where covalent bonds across the heterointerface form but the thermal fluctuation cannot overcome the kinetic barrier for the advance of threading dislocations. Somehow low temperature does not allow strain relaxation by generation of threading dislocations which is thermodynamically preferred, but leaves the structure at a metastable state.

The transition between coherency (with no dislocation and with strain) and semi-coherency (strain is partially relaxed by dislocations) also requires the motion of dislocations to (or near to) the epilayer/substrate interface, not only the discussion on energy we have done above.

Considering the Peach-Koehler force,

$$d\bar{F} = \left(\bar{b} \bullet \bar{\bar{\sigma}}\right) \times \hat{l}, \quad \text{(Eq. 13)}$$

which describes the force acting on unit length of dislocation in an external stress field, and from a similar formalism as the total energy by strain and dislocations, $u_{coh} + u_{dis}$, we derived above, the excess force to drive the bending of threading dislocations to form misfit segments is;

$$\begin{aligned} \sigma_{exc} &= \sigma_{coh} - \sigma_{dis} \\ &= -2\mu\left(\frac{1+\nu}{1-\nu}\right)\left(f - \rho_{md} b_{edg,\parallel}\right) - \frac{\mu b}{4\pi h \cos\lambda}\left(\frac{1-\nu\cos^2\beta}{1-\nu}\right)\ln\left(\frac{4h}{b}\right) \end{aligned} \quad \text{(Eq. 14)}$$

When $\sigma_{exc} > 0$, threading dislocations will tend to bend over to form strain-relaxing misfit segments. When $\sigma_{exc} < 0$, threading dislocations that have bent over to form strain-relaxing misfit segments will tend to straighten. [9-11]

Based on the excess stress, a measure of the driving force for strain relaxation by dislocation creation, the dynamics of dislocations in bulk materials is summarized in what are known as deformation-mechanism maps, hereafter denoted as DMM. Figures 2.8 and 2.9 are the DMM for Si and Ge, respectively. [12] From the iso-strain rate contours in the maps, we can roughly estimate the dislocation density in the material for a given set of stress, process temperature and time.

Let's think about wafer bonding of Si and Ge as a case study. From Eq. 14, the normalized stress, σ/μ, at the bonding heterointerface is around or less than the misfit, f, which is 4 % for Si and Ge. This is because the Poisson's ratio, v, is around 0.25 – 0.35 for most common materials and then $2(1-v)/(1+v)$ is around 1. Then, in Figures 2.8 and 2.9, the strain rate drastically varies between $1\text{x}10^{-10}$ s^{-1} and 1 s^{-1} for both of Si and Ge around at half of their melting temperature, at which people actually do the wafer bonding successfully.

However, stress depends on the position in the layers from the interface. A theoretical model considering periodic compressive and tensile strains along the wafer-bonded interface shows that the strain is highly localized to the interface rapidly diminishing away from the interface. [13] The displacement of atoms to the direction parallel to the bonding interface is proportional to an exponent including the distance from the interface;

$$u \propto Exp\left(-\frac{2\pi f}{a}z\right),$$

where f is the lattice mismatch, a is the lattice constant, and z is the distance from the interface. From this equation, assuming $f = 0.05$ and $a = 5$ A, the atomic displacement at the 10 nm distant from the interface is only 0.2 % of that of the interface. Since stress is proportional to displacement, σ/μ is less than $1x10^{-4}$ at 10 nm distant from the interface in this case, where the strain rate is far smaller than $1x10^{-10}$ s^{-1} in the DMM. At this strain rate, the dislocation density is less than the order of one dislocation per centimeter, which is essentially negligible, after 1 hour thermal process. This implies a minimal disturbance to the bulk of the materials during the wafer bonding process.

Actually a lot of TEM observations show only misfit dislocations at the bonded interface, sometimes with threading dislocation half-loops around the interface, but no threading dislocation throughout a layer. [14]

This is rather different from the heteroepitaxial growth of thick layers on lattice-mismatched substrates, in which the strain relaxation resulted in high densities of threading dislocations in the grown layers. When growth proceeds, many of misfit dislocations at the interface continue to extend into the thickness of the grown structure.

Since it is known that thermal strain from difference of thermal expansion coefficients is proportional to the square root of layer thickness, it is often effective to thin one of the bonded wafers before thermal process to reduce strain, if the interface has enough mechanical strength to endure the thinning process. [14]

In equilibrium, theoretically the dislocation density in epi-grown films and wafer bonded films would be same, as long as the combinations of the materials are same. However, in wafer bonding, considering kinetics, the dislocations first generating at the bonding interface cannot fully propagate throughout the films or mostly stay at the interface leaving strain energy in the films, for common wafer bonding conditions (temperature, time). So, we can conclude wafer-bonded heterostructures have dislocations almost only at the bonded interfaces and therefore have better performance as optoelectronic materials than those of epi-grown heterostructures, which have dislocation also in the bulk region of the grown films.

Practically it is difficult to have the density of threading dislocation in heteroepitaxy less than $1x10^6$ cm^{-2}. Under this defect density, most majority-carrier devices such as field-effect transistors perform normally, but the minority-carrier devices such as lasers experience appreciable degradation.

In contrast to the heteroepitaxial growth, these misfit dislocations were all edge dislocations, strictly confined at the heterointerface. Neither stacking faults nor threading dislocations were found over the entire region being inspected. [15-17]

2-3-3. Existing applications of wafer bonding

Direct wafer bonding of InP and GaAs is a significant and promising process for various kinds of device application, such as high-speed LED and HEMT [18], long-wavelength VCSEL [19], nano photonic crystals for WDM [20,21] and strained SiGe-on-insulator for

MOSFET [22]. Recently silicon-based (i.e. compatible with conventional CMOS (complementary metal oxide semiconductor) technologies) hybrid InP laser was developed using InP/Si wafer bonding by the team of Prof. John Bower of UC Santa Barbara. [23] James Zahler et al, one of my collaborators, of Aonex Technologies has succeeded to fabricate GaN LEDs on inexpensive wafer bonded sapphire/poly-AlN substrates. [24]

2-3-4. Wafer bonding for lattice-mismatched multijunction solar cells

As we saw in the previous sections, multijunction solar cells with III-V semiconductor compound materials are promising for ultrahigh (> 40%) efficiency solar energy conversion in the coming decades. Most current multijunction solar cell design approaches are focused on either lattice-matched designs or metamorphic growth with dislocations to accommodate subcell lattice mismatch, which inevitably results in less design flexibility or lower material quality than is desirable. [8, 25]

Material integration by the direct wafer bonding technique enable atomic scale semiconductor- semiconductor bonding and do not utilize any metal as bonding agent at interfaces. Thus interface transparency, thermal conductivity, thermal stability and reliability should be superior to mechanical stacking approaches using patterned metallic pastes and frits. Also, monolithic, or two-terminal, devices can be integrated into modules with the same simplicity afforded by single-junction devices, with metallization at the very top and bottom of the stack only. Three- and four-terminal configurations do not require lattice mismatch or current matching. However, they are generally less

desirable structures, because of their complexities of fabrication and assembly, than the monolithic device. [26]

Direct wafer bonding enables dislocation-free active regions by confining the defect network needed for lattice mismatch accommodation to heterointerfaces. [14,27] The strain is highly localized to the interface rapidly diminishing away from the interface, implying a minimal disturbance to the bulk of the materials during the wafer bonding process. [13]

Figure 2.10 shows an ideal structure of III-V multijunction solar cell, which could exhibit ultrahigh efficiency. [28,29] It is difficult to prepare this multistack structure by epitaxial growth with optimal material quality because of the 4% lattice mismatch across the interface of the GaAs and InGaAs subcells. Wanlass et al reported a 37.9% efficiency cell with an epitaxially grown triple-junction structure of InGaP/GaAs/InGaAs. [30] However a considerable density of dislocations limiting the cell efficiency was observed in the InGaAs layer of graded composition. This result suggests the potential of over-40% efficiency utilizing the wafer bonding technology to diminish the dislocations.

In this thesis (Chapters 3 and4), GaAs/InP direct wafer bonding was first investigated for mechanically robust and highly conductive heterointerfaces applicable for solar cell applications. Secondly the first direct-bond interconnected multijunction solar cell, a two-terminal monolithic GaAs/InGaAs dual-junction cell, was fabricated based on the

bonding investigation to demonstrate a proof-of-principle for the viability of direct wafer bonding for solar cell applications.

2-3-5. Wafer bonding for III-V semiconductor compounds layer transfer for inexpensive alternative epitaxial substrate structures

Wafer bonding technologies introduced in the previous sections can be applied not only for lattice-mismatched stacking, but also for fabrication of low-cost epitaxial substrates. Wafer bonding enables us to do "layer-transfer" of thin films of expensive III-V semiconductor compound materials onto cheaper material substrates. This technique is the second main topic of my thesis and its detail will be described in Chapters 5 and 6. The basic idea is to reduce the cost of expensive InP bulk substrate for III-V semiconductor compound multijunction solar cells by replacing those substrates with an alternative substrate structure of a thin InP film sitting on top of an inexpensive Si wafer (Figure 2.11), which can be fabricated through layer transfer technique using wafer bonding.

2-4. List of symbols

ν : Poisson's ratio (= the negative of the ratio between lateral and longitudinal strains under uniaxial longitudinal stress)

μ : shear modulus (= the ratio between applied shear stress and shear strain under pure shear)

b: Burgers vector

r_0: inner radius of the cylinder, or the "cutoff" radius

R: outer radius of the cylinder

β: angle between the Burgers vector and the dislocation line

ρ_{md}: linear density of dislocations

f: lattice parameter misfit between the epitaxial layer and the substrate

λ: angle between the Burgers vector and the direction that is both normal to the dislocation line and that lies within the plane of the interface

h: thickness of the film

U_{edg}: energy per unit length associated with the elastic stresses and strains for edge dislocations

U_{scr}: energy per unit length associated with the elastic stresses and strains for screw dislocations

σ: stress

l: dislocation line

θ: twist angle between the wafer pairs

S_d: spacing between neighboring dislocations

a: lattice constant

D_{dis}: areal density of dislocations

2-5. References

[1] W. Shockley and H. J. Queisser, *J. Appl. Phys.* **32** (3), 510-519, 1961.

[2] C. H. Henry, *J. Appl. Phys.* **51** (8), 4494–4500, 1980.

[3] R. R. King et al, *Appl. Phys. Lett.* **90**, 183516, 2007.

[4] J. M. Zahler, Doctoral Thesis, California Institute of Technology, 2005.\

[5] Y. Li et al, *Phil. Mag.* **85**, 3073, 2005.

[6] P. Kongjaeng et al, *J. Cryst. Growth* **298**, 111, 2007.

[7] M. Shimbo, K. Furukawa, K. Fukuda, and K. Tanzawa, *J. Appl. Phys.* **60**, 2987-2989 (1986).

[8] S. Mahajan, *Acta Mater.* **48**, 137-149, 2000.

[9] D. Hull, *Introduction to Dislocations*, 2nd ed., Pergamon Press, 1975.

[10] J. Y. Tsao, *Materials Fundamentals of Molecular Beam Epitaxy*, Academic Press, 1993.

[11] L. B. Freund and S. Suresh, *Thin Film Materials –Stress, Defect Formation and Surface Evolution*, Cambridge University Press, 2003.

[12] H. J. Frost and M. F. Ashby, *Deformation-Mechanism Maps*, Pergamon, Oxford, 1982.

[13] Z. L. Liau. *Phys. Rev. B* **55** (19), 12899, 1997.

[14] U. Goesele and Q. Y. Tong, *Ann. Rev. Mater. Sci.* **28**, 215, 1998.

[15] G. Patriarche et al, *J. Appl. Phys.* **82** (10), 4892-4903, 1997.

[16] Y. H. Lo et al, *Appl. Phys. Lett.* **58**, 1961, 1991.

[17] Y. H. Lo et al, *Appl. Phys. Lett.* **62**, 1038, 1993.

[18] T. Whitaker, *Compound Semiconductor* **35**, May, 2002.

[19] H. C. Lin et al, *J. Appl. Phys.* **92**, 4132, 2002.

[20] S. Noda et al, *Appl. Phys. Lett.* **75**, 905, 1999.

[21] S. Noda et al, *Science* **289**, 604-606, 2000.

[22] B. Ghyselen et al, *Solid-St. Electron.* **48**, 1285, 2004.

[23] H. Park et al, *Opt. Express* **13**, 9460, 2005.

[24] J. M. Zahler et al, *Compound Semiconductor*, Nov. 2006.

[25] Y. Shimizu and Y. Okada, *J. Cryst. Growth* **265**, 99-106, 2004.

[26] J. M. Olson, D. J. Friedman, and S. R. Kurtz, in *Handbook of Photovoltaic Science and Engineering*, edited by A. Luque and S. Hegedus (Wiley, New York), 2003, pp. 359-411.

[27] A. Fontcuberta i Morral et al, *Appl. Phys. Lett.* **83**, 5413-5415, 2003.

[28] J. M. Zahler et al, *Proc. 29th IEEE Photovoltaic Specialists Conference*, 45-48, 2002.

[29] P. R. Sharps et al, *Proc. 26th IEEE Photovoltaic Specialists Conference*, 895-898,1997.

[30] M. W. Wanlass et al, *MWW 3rd ISCC*, 2005.

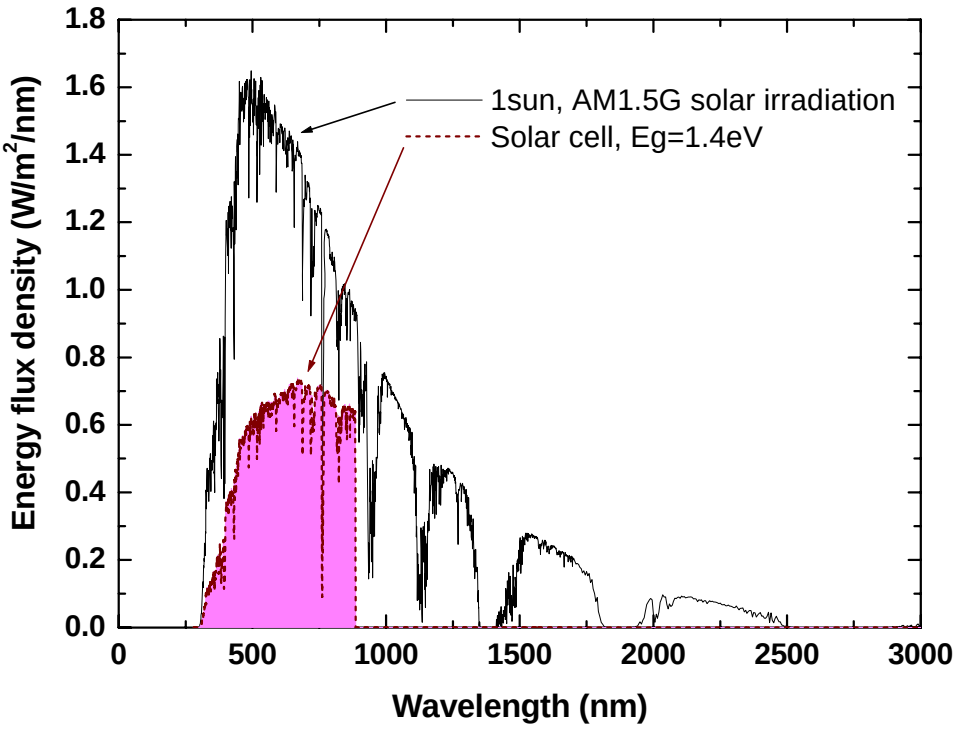

Fig. 2.1 (a) Solar irradiation spectrum of AM1.5G, 1 sun and energy utilization spectrum by a single-junction solar cell with the optimized energy bandgap to obtain the maximum efficiency. Eg = 1.4 eV, η = 31.3%.

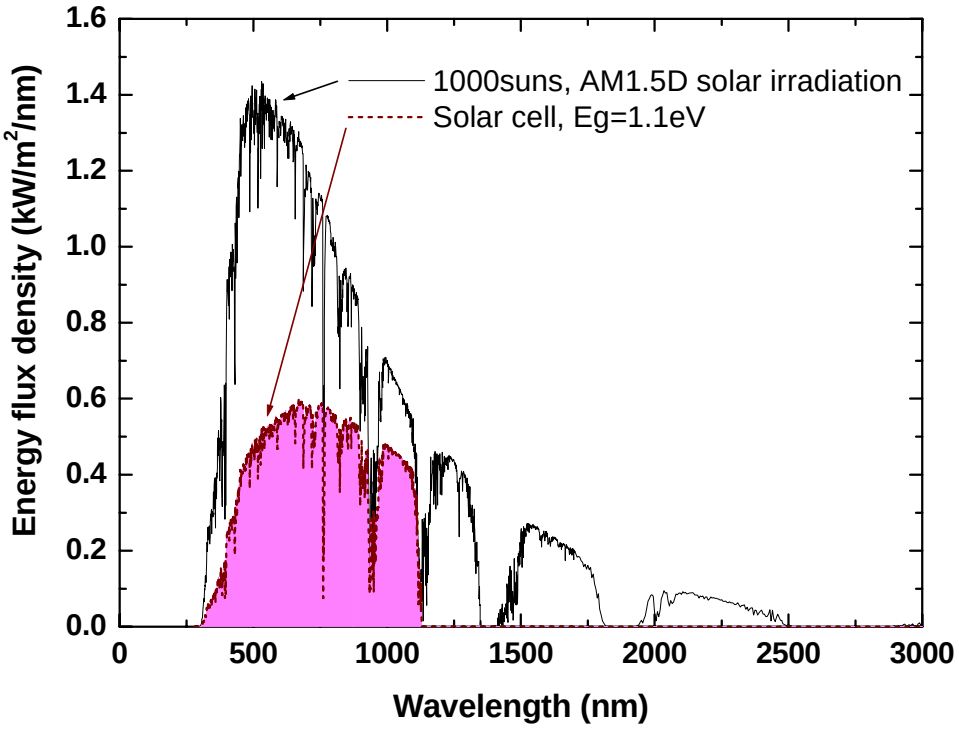

Fig. 2.1 (b) Solar irradiation spectrum of AM1.5D, 1000 suns and energy utilization spectrum by a single-junction solar cell with the optimized energy bandgap to obtain the maximum efficiency. Eg = 1.1 eV, η = 37.6%.

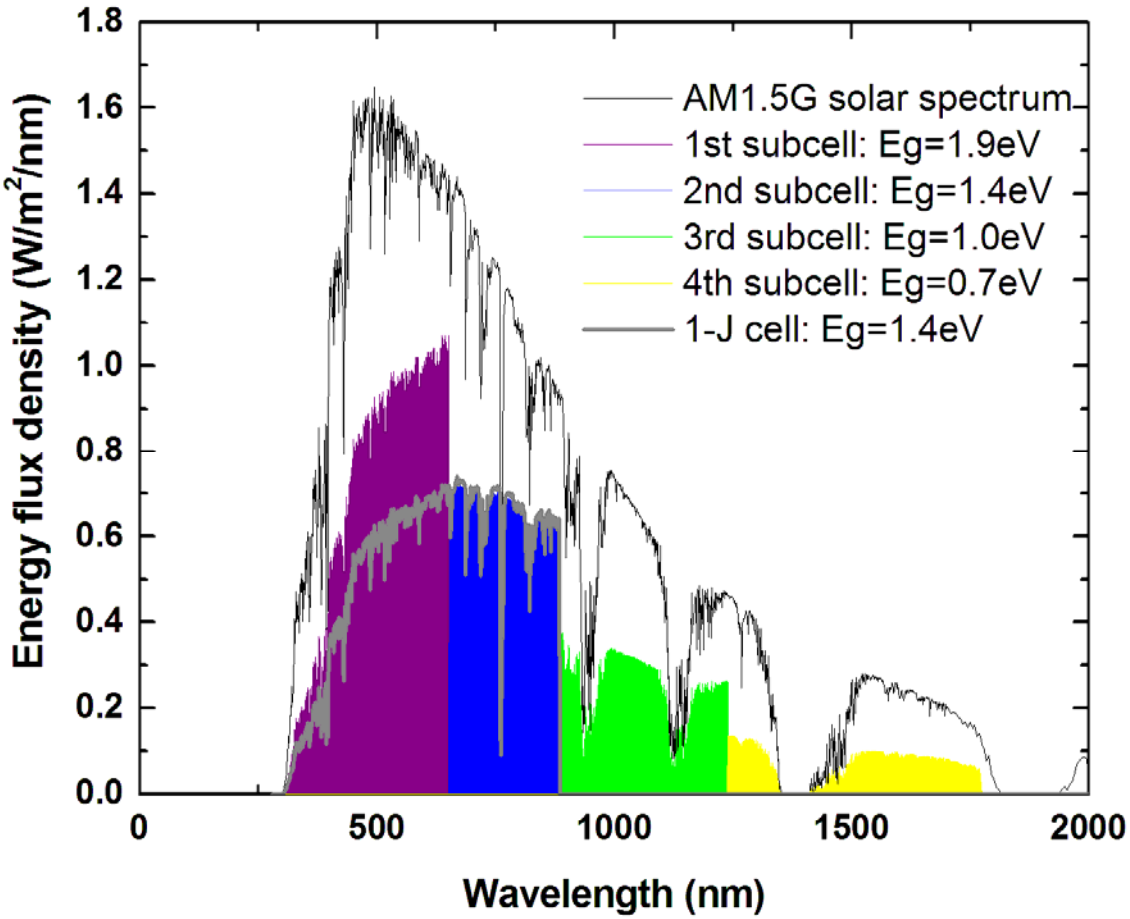

Fig. 2.2 Solar irradiation spectrum of AM1.5G, 1 sun and energy utilization spectrum by a four-junction solar cell. Also plotted is the energy utilization spectrum by a single-junction solar cell with the optimized energy bandgap of 1.4 eV.

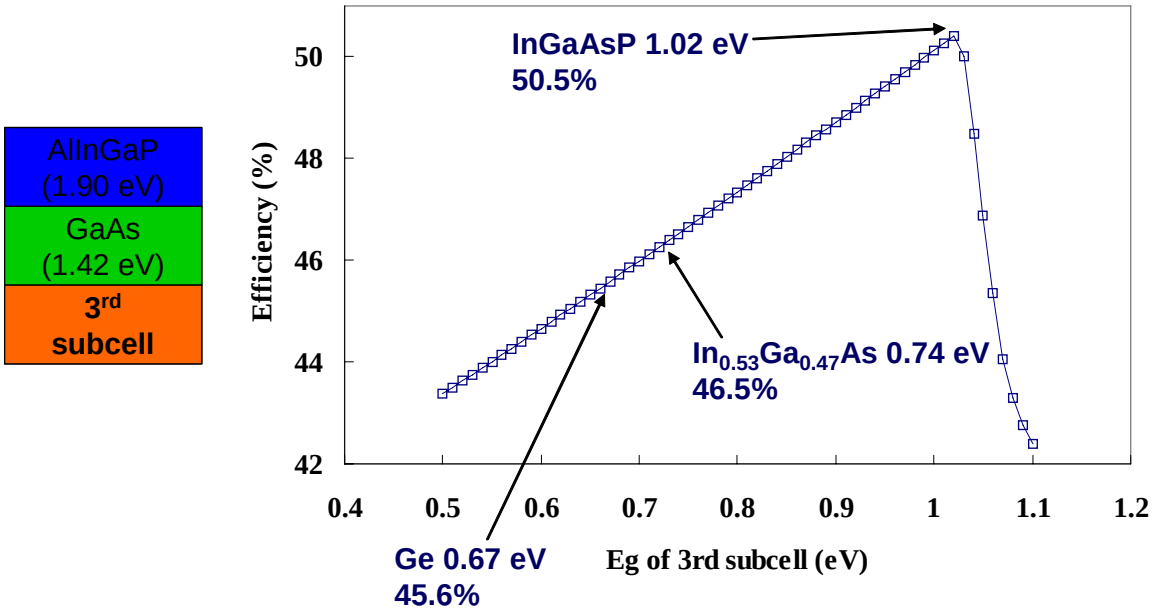

Fig. 2.3 Dependence of the computed detailed balance limit efficiency on the bandgap energy of the 3rd subcell for an AlInGaP (1.90 eV) / GaAs (1.42 eV) / 3rd subcell triple junction solar cell under a 100-sun illumination.

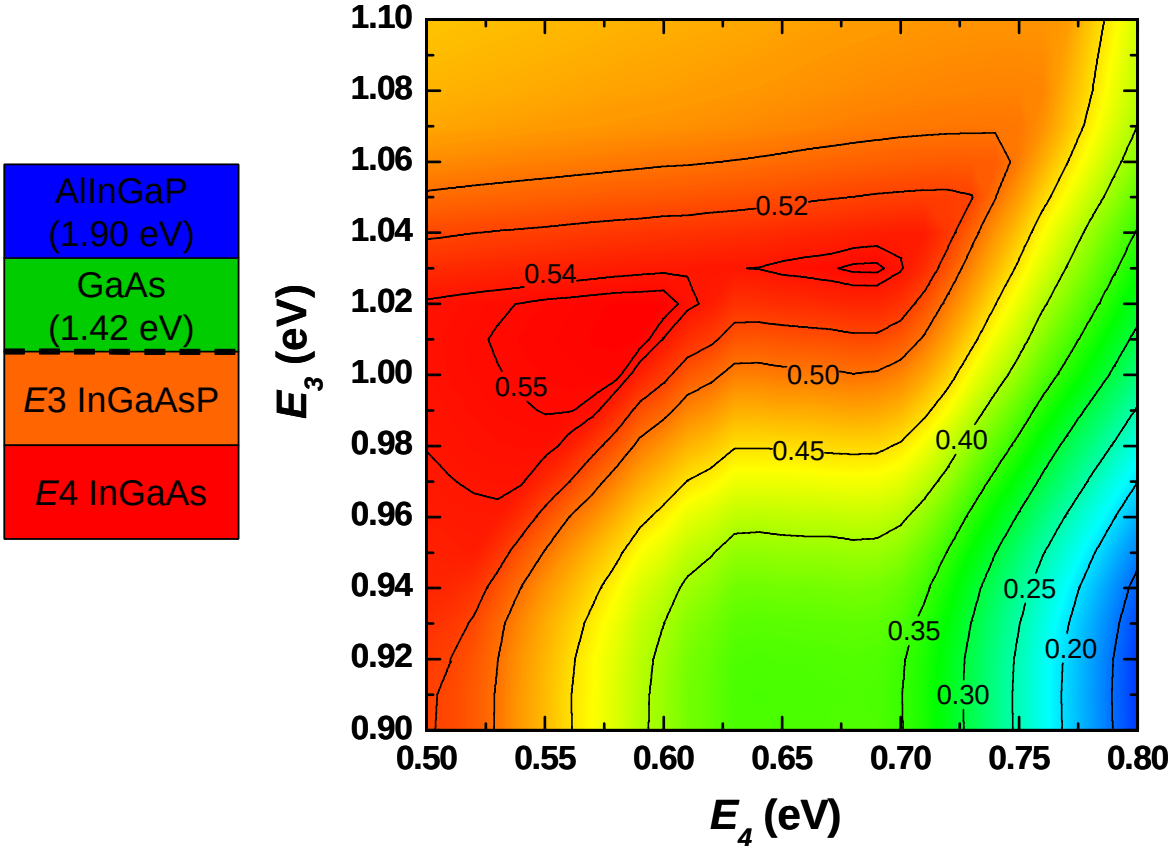

Fig. 2.4 Contour plot of four-junction cell efficiencies depending on the bandgap energies of the 3rd and 4th subcells for an AlInGaP (1.90 eV) / GaAs (1.42 eV) / 3rd subcell / 4th subcell four-junction solar cell under a 100-sun illumination.

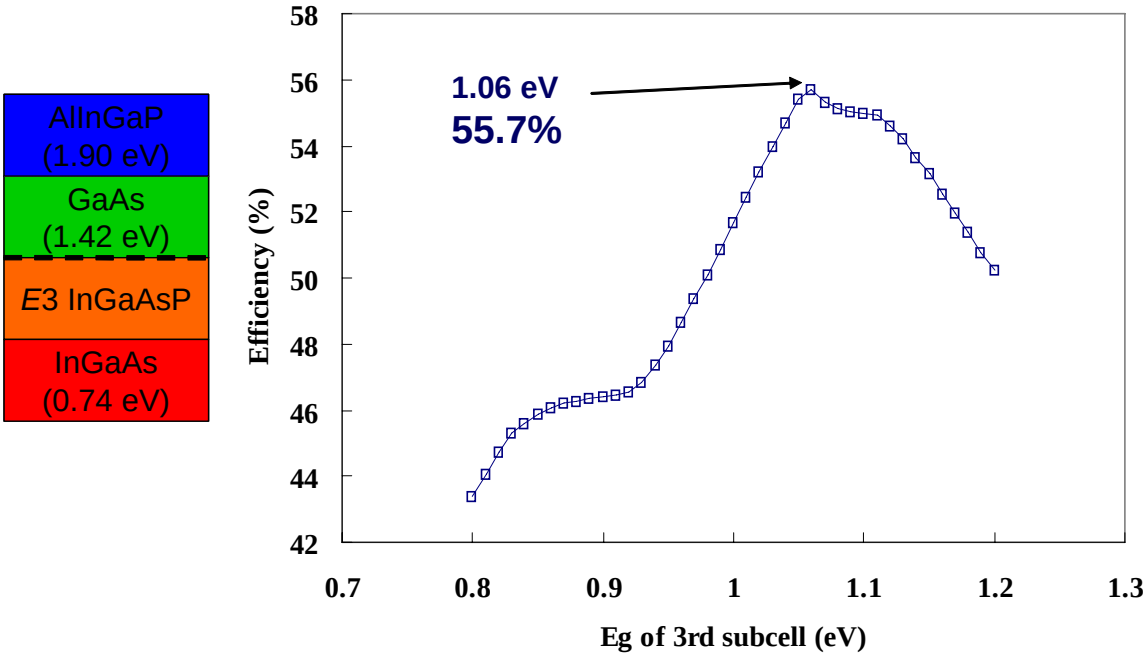

Fig. 2.5 Dependence of the computed detailed balance limit efficiency on the bandgap energy of the 3rd subcell for an AlInGaP (1.90 eV) / GaAs (1.42 eV) / 3rd subcell / InGaAs (0.74 eV) four-junction solar cell under a 100-sun illumination assuming independent connection of the top dual-junction and the bottom dual-junction.

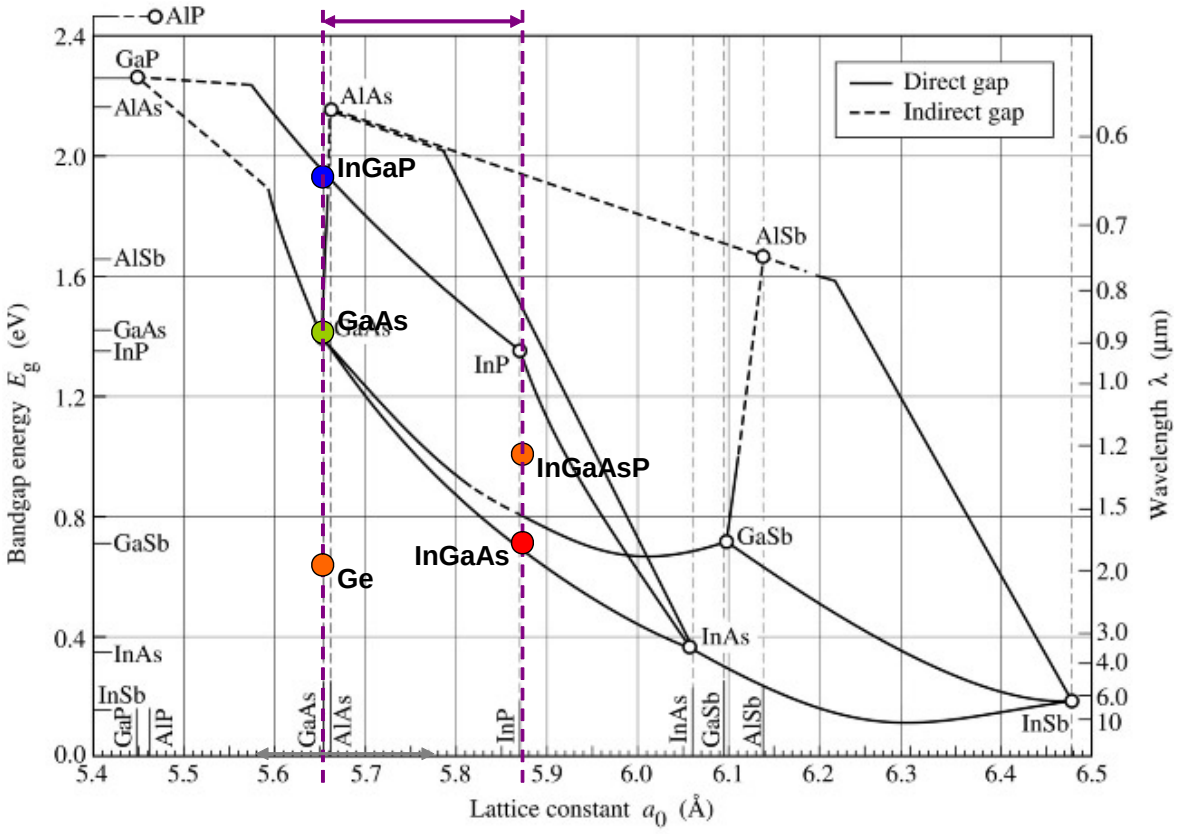

Fig. 2.6 Plot of lattice constants and bandgap energies for commonly used III-V semiconductor compounds. Note that the lattice constants of ternary and quaternary compounds depend on the materials composition and the values shown here is just examples to fit the concept of this study.

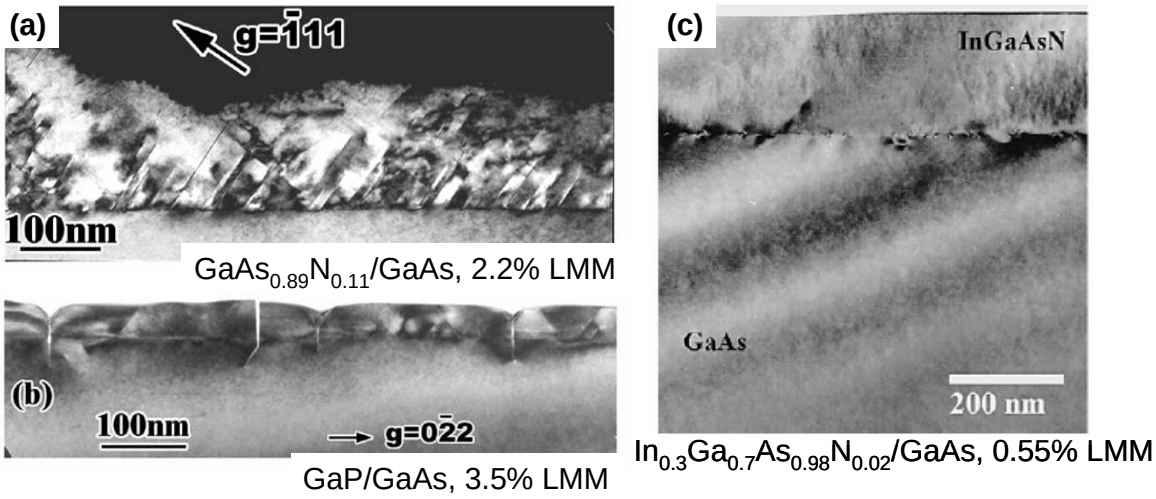

Fig. 2.7 Cross-sectional transmission electron microscopy (TEM) images for the interface of grown layers and substrates with lattice mismatch for common III-V semiconductor compound materials.

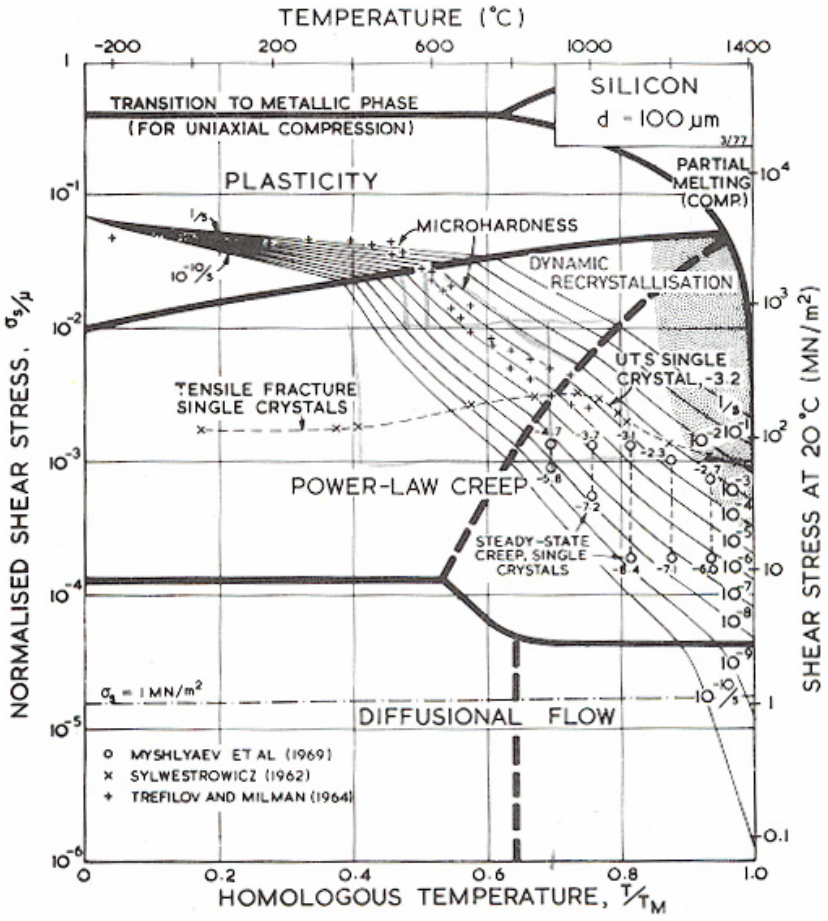

Fig. 9.1. Stress/temperature map for silicon of grain size 100 μm. Data are labelled with $\log_{10}(\dot{\gamma})$.

Fig. 2.8 Stress/temperature map for silicon of grain size 100 um. (from Ref. 12)

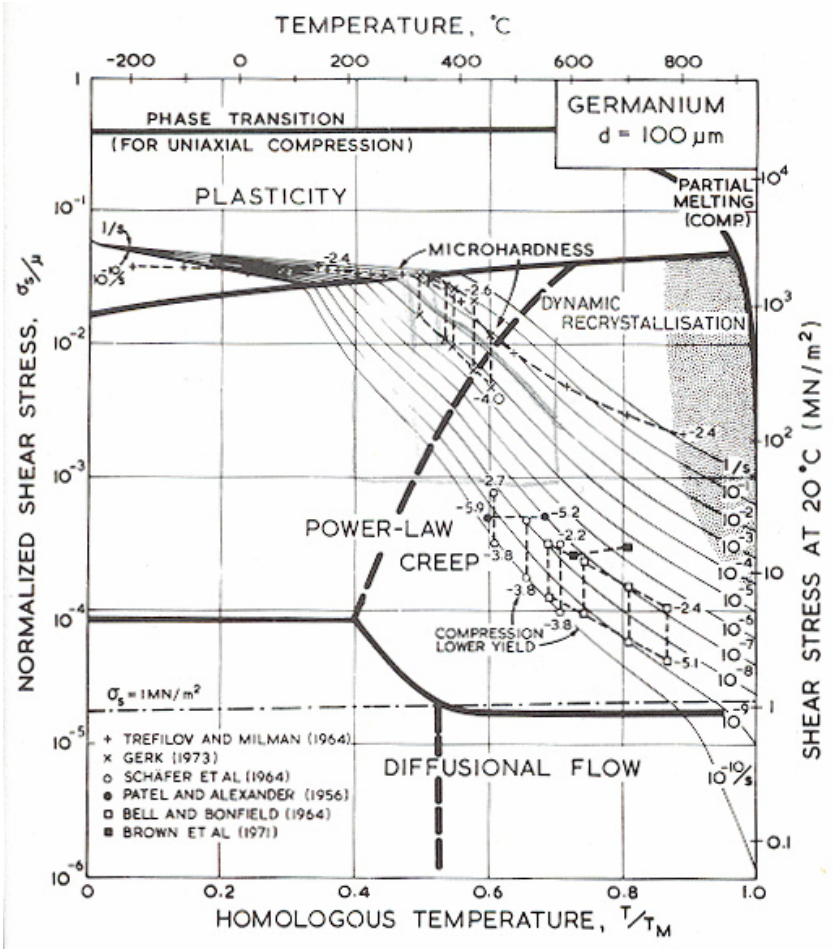

Fig. 9.3. Stress/temperature map for germanium of grain size 100 μm. Data are labelled with $\log_{10} \dot{\gamma}$.

Fig. 2.9 Stress/temperature map for germanium of grain size 100 um. (from Ref. 12)

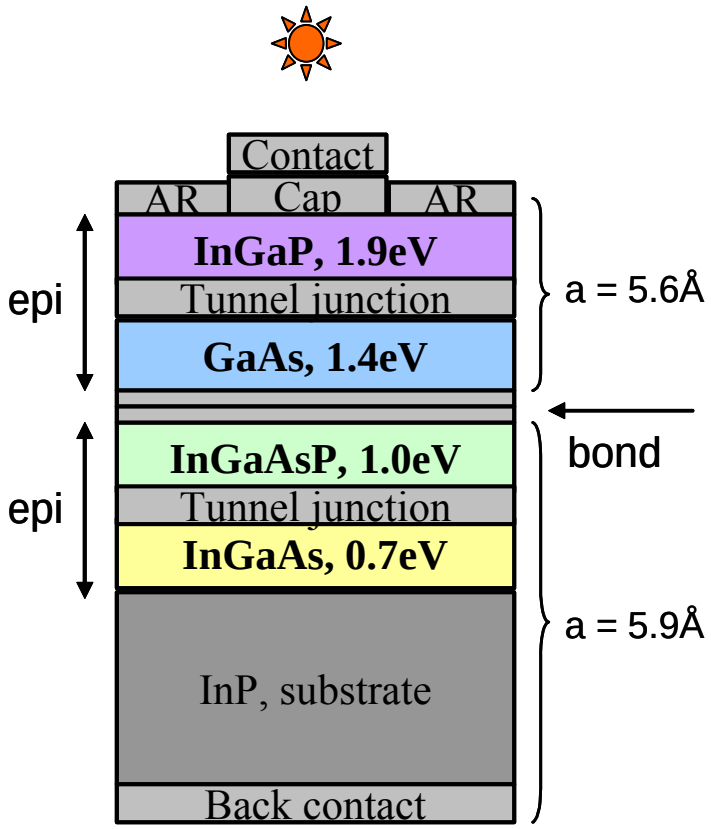

Fig. 2.10 Schematic cross section of the InGaP/GaAs/InGaAsP/InGaAs four-junction solar cell structure.

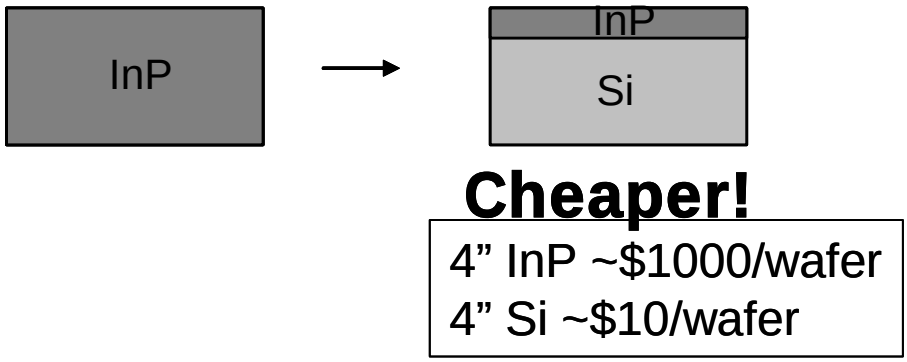

Fig. 2.11 Schematics of the cost reduction scheme by replacing conventional bulk InP substrates with an alternative InP/Si substrate.

Chapter 3 GaAs/InP wafer bonding

3-1. Introduction

In the previous chapter, I explained why multijunction solar cells are efficient and lattice-mismatched materials stacking would be good, how difficult to obtain high-quality (i.e. low dislocation density) crystal layered structures of lattice-mismatched materials by epitaxial growth, and the possibility of direct wafer bonding technique to overcome this problem to give us the pathway to ultrahigh efficiency solar cells. In this chapter, I would like to describe my investigation on direct wafer bonding of GaAs and InP applicable for multijunction solar cell applications.

Aim of this study

For solar cell applications, the interfaces among semiconductor layers have to be highly conductive not to reduce the cells' energy conversion efficiency by dissipate the transferred electronic carriers as heat due to the Ohmic loss. Therefore I investigated the wafer bonding process of GaAs and InP to obtain Ohmic GaAs/InP junctions with low resistance.

3-2. Experimental

Before studying the direct bonding of solar subcells, direct bonding of bulk GaAs and InP wafers was investigated. (001) n-type GaAs and InP wafers doped respectively with Si and S were used. The basic doping concentrations were 2x 10^{18} cm^{-3} Si in GaAs and 4.5x 10^{18} cm^{-3} S in InP (both denoted as "n"). Interfacial bonding layers prepared by

MOCVD (metal-organic chemical vapor deposition) growth of thin epitaxial Se-doped GaAs layers on GaAs with and S-doped InP on InP with doping concentration of 1x 10^{19} cm^{-3} (denoted as "n^+"), schematically shown in Figure 3.1, were also investigated. These n^+ heavy doped bonding layers were 20 nm thick for GaAs and 500 nm thick for InP.

The GaAs and InP wafers were first coated with photoresist (Shipley 1813) with a spincoater with a spinning velocity 3000 rpm for 1 min followed by soft bake at 115 ^oC for 90 sec. This photoresist coating is to protect the bonding surfaces of GaAs and InP from particles generate in the following dicing process because interfacial particles would degrade the bonding strength. The wafers were then diced into ~1 cm^2 area. Then the applied photoresist was removed sequentially placed in boiling acetone with a beaker placed on a hotplate at 115 ^oC for 10 min, in renewed acetone with a beaker placed in an ultrasonic bath for 15 min, in methanol with a beaker placed in an ultrasonic bath for 15 min, and rinsed with D. I. (de-ionized) water. This series of washing process has also a function of surface degreasing, as well as photoresist removal. Then the native oxide was removed by dipping the GaAs and InP pieces in 7 vol%-HCl (aq) and 10 vol%-HF (aq), respectively, for 30 sec. At this point, both of the GaAs and InP wafers are observed to be highly hydrophobic. Then the wafers were brought into contact with their polished sides face to face with the (011) edges aligned, as schematically shown in Figure 3.2. The joined GaAs/InP pairs were annealed at ~0.5 MPa at 270 ^oC in atmosphere for 10 hours followed by annealing in 10% H_2 diluted by N_2 (denoted as "H_2/N_2") or N_2 at 450-600 ^oC for 30 min. Some bonded pairs were subject to only one of these two annealing

processes. A photograph of the wafer bonding facility used in this study is shown in Figure 3.3.

The electrical properties of the bonded interfaces were investigated for the different annealing conditions by measuring the current-voltage (I-V) characteristics. Bonded pairs with both high and low doping concentrations at the subsequent bond interfaces were investigated. Indium solder pads were used for Ohmic contact from the electrical probes and the stage of the I-V measuring facility to the semiconductor materials, GaAs and InP. Figure 3.4 shows a schematic of the materials configuration in the electrical measurements for the bonded GaAs/InP wafers.

Secondary-ion mass spectroscopy (SIMS) depth profile measurements were performed across the bonded interfaces of GaAs/InP to analyze the chemical composition of the bonding interfaces. Cesium ions were used for sputtering to obtain depth profiles of hydrogen and oxygen. This SIMS measurement was conducted by Bob (Robert) Reedy at NREL (National Renewable Energy Laboratory).

3-3. Results and discussion

For multijunction solar cells, formation of mechanically robust, low resistance interfaces is a critical aspect for structure stability and high energy conversion efficiency. I-V characteristics were compared among the bonded nGaAs/nInP pairs with various annealing conditions. Ohmic contact was obtained only for the pair annealed at 0.5 MPa

at 270 ^{o}C followed by annealing at 600 ^{o}C in H_2/N_2, as shown in Figure 3.5, which indicates a significant effect of hydrogen at high temperature.

Figure 3.6 depicts the depth profiles of hydrogen and oxygen concentrations across the bonded nGaAs/nInP heterointerfaces measured by SIMS before and after the annealing in H_2/N_2 at 600 ^{o}C. This result shows a significant reduction of the interfacial hydrogen and oxygen following the 600 ^{o}C anneal in H_2/N_2. The integrated dose of oxygen after the 600 ^{o}C annealing corresponds to a layer with thickness of around 1 nm, which is a reasonable value to induce tunneling current to enable one to obtain Ohmic heterointerfaces, perhaps with some oxide breakdown by the applied voltage. [1, 2] A general picture for the chemical evolution of the bonded bulk GaAs/InP interface could be as follows: Upon room temperature bond initiation, the GaAs/InP interface is characterized by mainly by van der Waals bonding. A covalently bonded GaAs/InP interface is subsequently formed in annealing at 270 ^{o}C under pressure, mediated by a thin interfacial oxide, as indicated by SIMS analysis. This is supported also by the fact that the interface of the bonded pair has enough strength to endure the shear force applied in the mechanical polishing process for the SIMS measurement. Applied pressure is presumed to increase the interfacial contact area, as omission of an annealing step under pressure resulted in non-Ohmic I-V characteristics. Higher-temperature annealing in H_2/N_2 reduces hydrogen and oxygen at the bonded interface leading to higher interfacial conductance.

Heavy doping at the GaAs and InP interfaces to be subsequently bonded was also found to significantly enhance the GaAs/InP interfacial conductivity. Figure 3.7 shows the I-V curves of the bonded GaAs/InP interfaces for the n^+GaAs/n^+InP pairs after pressure annealing at 270 ^oC only and pressure annealing at 270 ^oC followed by annealing in H_2/N_2 at 450 ^oC. This conductivity enhancement can be explained by analysis of the heterojunction band offset at the GaAs/InP interface. Electron transport rather than hole transport dominates the current flow in the n-type GaAs and InP used in this study. (n.b., the conduction-band edge of GaAs is 0.3 eV above that of InP for intrinsic materials. [3]) One-dimensional simulations of the heterojunction bandbending indicate a significant decrease in the interface potential barrier width at higher doping concentrations, especially on the GaAs side of a GaAs/InP heterojunction. [4] This barrier thinning enables interfacial tunneling, rather than thermionic emission, leading to higher conductivity across the heterojunction interfaces. [5, 6]

Ideally, Ohmic GaAs/InP heterojunctions would be formed by bonding at lower temperature to avoid possible degradation of the cell interfaces and p-n junctions for multijunction solar cell applications. The approach taken here yielded Ohmic interfaces with < 0.10 Ohm-cm^2 interface resistance at as low as 450 ^oC and < 1.0 Ohm-cm^2 by solely pressure annealing at 270 ^oC in n^+GaAs/n^+InP structures, as shown in Figure 3.5

3-4. Conclusions

In this section, low resistance Ohmic GaAs/InP junctions were obtained overcoming ~4% lattice mismatch using direct wafer bonding technique. The key factors were

reduction of the interfacial oxygen and hydrogen by annealing in reduction atmosphere and high doping for the interfacial bonding layers to induce tunneling current. The obtained bonded GaAs/InP structures are suitable for lattice-mismatched multijunction solar cell applications with their highly conductive interfaces. Simple considerations suggest that for such a cell the currently-reported interfacial resistance smaller than 0.1 Ohm-cm^2 would result in a negligible decrease in overall cell efficiency of ~0.02%, under 1-sun illumination. [7]

3-5. References

[1] E. Rosenbaum and L. F. Register, *IEEE Trans. Electr. Dev.* **44**, 317, 1997.

[2] E. Miranda, J. Sune, R. Rodriguez, M. Nafria, and X. Aymerich, *Appl. Phys. Lett.* **73**, 490, 1998.

[3] S. Tiwari and D. Frank, *Appl. Phys. Lett.* **60**, 630-632, 1992.

[4] PC1D Version 5.2 (University of New South Wales), 1998.

[5] A. Y. C. Yu, *Solid-St. Electron.* **13**, 239-247, 1970.

[6] H. Sasaki et al, *Appl. Phys. Lett.* **31**, 211-213, 1977.

[7] P. R. Sharps, M. L. Timmons, J. S. Hills, and J. L. Gray, *Proceedings of the 26th IEEE Photovoltaic Specialists Conference* (IEEE, New York, 1997), p. 895.

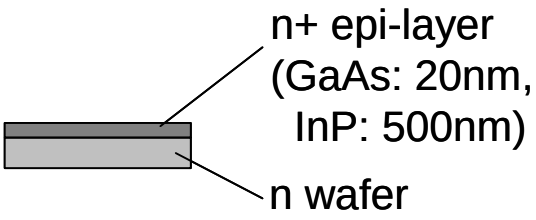

Fig. 3.1 Cross-sectional schematic of the III-V semiconductor compound wafer with a heavy doped bonding layer.

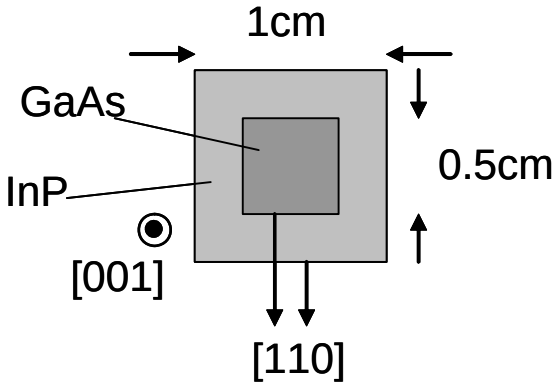

Fig. 3.2 Typical configuration of the bonded pair of semiconductor compound wafers.

Fig. 3.3 Photograph of the wafer bonder used in this study.

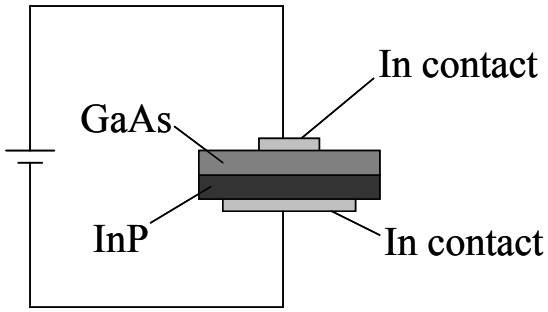

Fig. 3.4 Cross-sectional schematic of the materials configuration in the electrical measurements for the bonded GaAs/InP wafers.

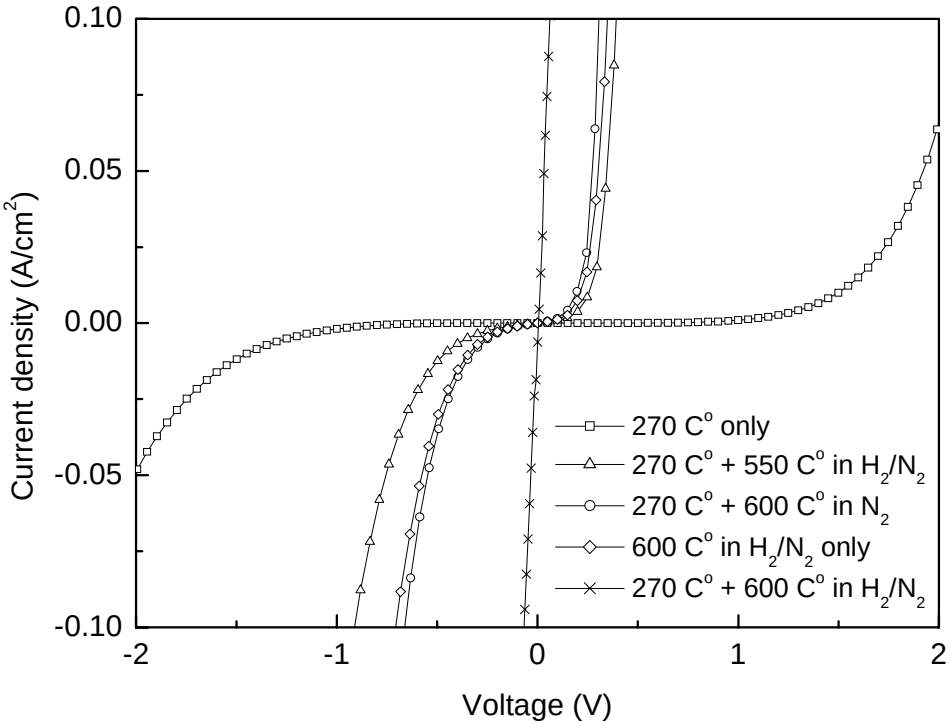

Fig. 3.5 I-V characteristics of the bonded GaAs/InP heterointerfaces for nGaAs/nInP. Positive bias voltage was applied from the GaAs side.

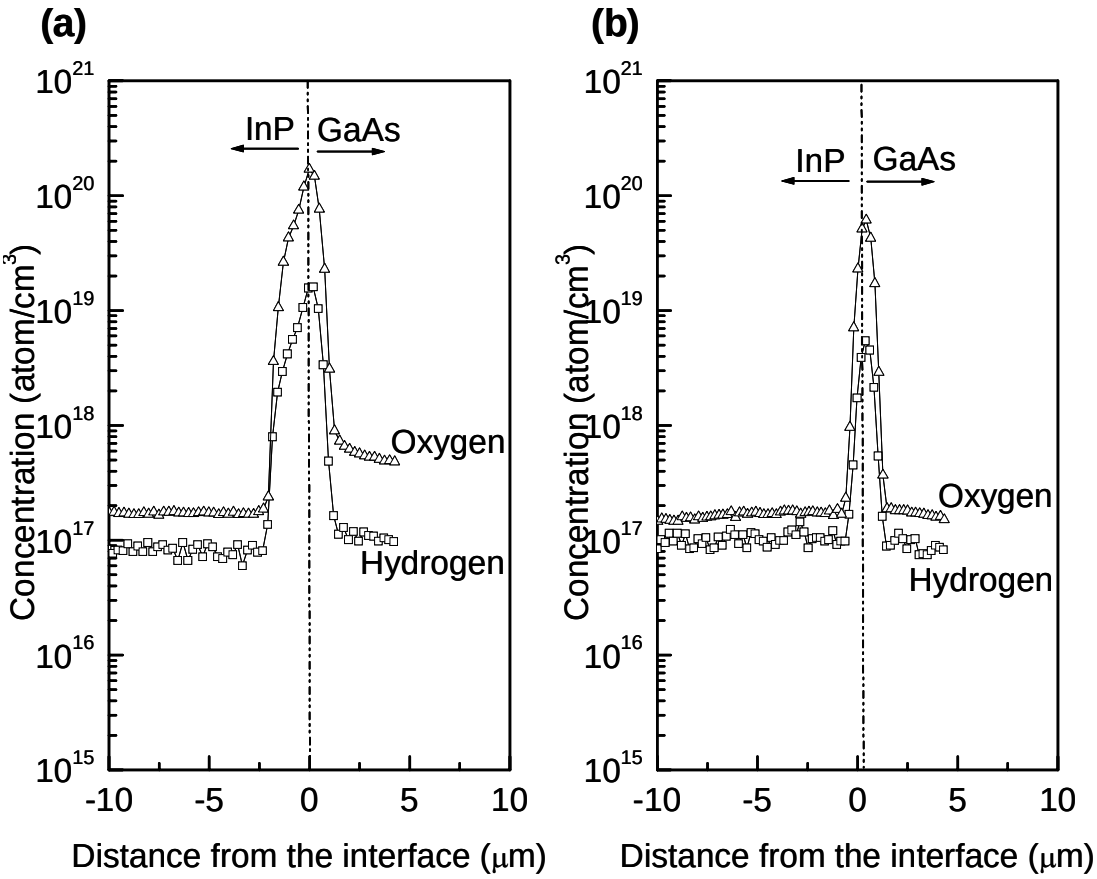

Fig. 3.6 Elemental concentration profiles across the bonded nGaAs/nInP heterointerfaces measured by SIMS (a) before and (b) after the annealing in H_2/N_2 at 600 ^oC. The profiles look extended along the depth than they actually are due to the roughness of the sputtered surface due to the thinning process by mechanical polishing.

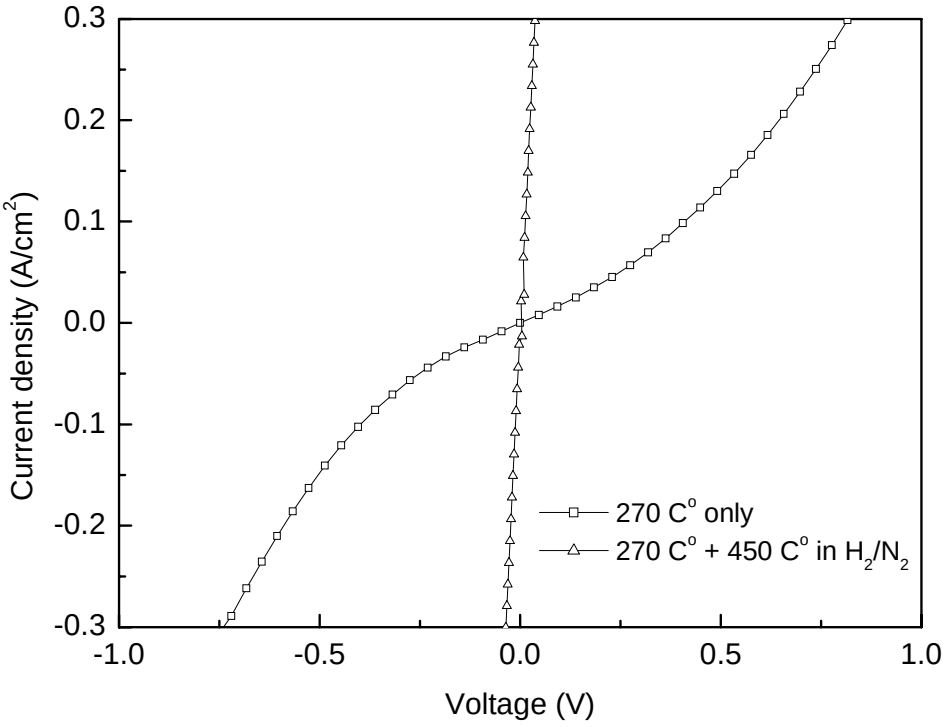

Fig. 3.7 I-V characteristics of the bonded GaAs/InP heterointerfaces for n^+GaAs/n^+InP. Positive bias voltage was applied from the GaAs side.

Chapter 4 Direct-bonded dual-junction GaAs/InGaAs solar cells

4-1. Introduction

In the previous chapter, low resistance, Ohmic GaAs/InP junctions were successfully fabricated via direct wafer bonding. In this chapter, the obtained GaAs/InP wafer bonding technique is actually applied for lattice-mismatched multijunction solar cell fabrication. GaAs subcells lattice matched to and grown on GaAs substrates and $In_{0.53}Ga_{0.47}As$ subcells lattice matched to and grown on InP substrates are bonded to form GaAs/ $In_{0.53}Ga_{0.47}As$ lattice-mismatched dual-junction solar cells.

Aim of this study

This chapter shows the very first demonstration of multijunction solar cell fabrication via direct wafer bonding. The characterization results for the fabricated solar cells are also presented.

4-2. Experimental

In the second phase of this study for GaAs/InP direct wafer bonding following Chapter 3, a two-terminal monolithic, dual-junction tandem solar cell was fabricated from direct bonding of single-junction GaAs and InGaAs subcells. The GaAs and InGaAs subcells were prepared by Daniel Aiken at Emcore Photovoltaics and Mark Wanlass at NREL (National Renewable Energy Laboratory), respectively. Figures 4.1 (a) and (b) show

schematic cross sectional diagrams for the GaAs and InGaAs subcells, respectively. The GaAs subcell consisted of p and n type layers of GaAs epitaxially grown on a (001) GaAs substrate by MOCVD. The InGaAs subcell ($In_{0.53}Ga_{0.47}As$) had a bandgap energy of 0.74 eV and consisted of p and n type layers of InGaAs layers lattice-matched to (001) InP. Specifically, the GaAs subcell was terminated with a Se-doped GaAs layer with 1 x 10^{19} cm^{-3} carrier concentration and the InGaAs subcell was terminated with a S-doped InP layer with carrier concentration of 2 x 10^{19} cm^{-3}. The GaAs and InGaAs subcells had n-on-p structures and the GaAs subcell had a n^+/p^+ tunnel junction to switch its bottom polarity from p-type into n-type for the bonding interface.

These subcells were bonded as described in Chapter 3 and annealed at 0.5 MPa at 380 ^oC for 10 hours. This relatively high bonding temperature was chosen to minimize the gas bubbles found at the bonding interface. After bonding of the two subcells, the GaAs substrate was removed to complete a GaAs/InGaAs/InP heterostructure forming the dual-junction solar cell, as schematically shown in Figure 4.2. The GaAs subcells had been grown on 625 μm thick 3-inch (001) GaAs wafers and then the GaAs wafers were mechanically grinded down to 150 μm thick from the back side at Emcore Photovoltaics in order to minimize the time required for the selective etch to remove the GaAs wafer totally after bonding while sustaining the strength to survive through the bonding process. Actually, I have an experience to bond 100 μm thick GaAs wafers, but the handling was a sort of difficult and I accidentally broke a lot of wafers. After the wafer bonding process of the GaAs subcell with the InGaAs subcell, the 150 μm thick GaAs substrate part was removed by chemical etching by H_3PO_4-H_2O_2-H_2O (1 : 4 : 5, volume fraction) at room

temperature around for 1 hour. Regular commercial 85% H_3PO_4 and 30% H_2O_2 chemical bottles and 18 Mega Ohm de-ionized (D. I.) water were used. I dipped the bonded GaAs/InGaAs structure in the chemical solution until I saw the shiny smooth surface of the InGaP etch-stop layer. The etching solution was regularly agitated for two purposes: one is to prevent spatial migration of the chemicals, which would significantly decelerate the etching reaction, due to the large H_3PO_4 weight and the other is to keep the areal uniformity of etching rate.

Then I deposited metal top and bottom contacts to the bonded dual-junction solar cell structures by thermal evaporation of Au. 150 nm thick Au was deposited by thermal evaporation with a deposition rate of ~5 Å/s on both of the cell front and back sides. No photolithography process was used, but a simply physical mask was applied for the evaporation to form a square ring-type front contacts. It should be noted that I missed to remove the 50 nm thick GaAs contact layer, which is supposed to exist only underneath of the front metal contact, simply due to my lack of knowledge and experience at the moment of this project. Proper removal of this contact layer would have increased the solar cell photocurrent and efficiency by minimize the wasted light absorption in the contact layer. Such front contact layers were properly removed for the projects of InGaAs solar cells on InP/Si substrates (Chapter 6) and plasmonic GaAs solar cells (Chapter 7). The cells were then annealed in H_2/N_2 at 350 ^oC for 30 min to form Ohmic metal contacts. It should be noted that the process conditions for the metallization and annealing were not optimized mainly because the number of the GaAs and InGaAs subcell samples delivered from Emcore and NREL was limited. Through the plasmonic GaAs project, to be described in Chapter 7, I have got a feeling that this annealing temperature of 350 ^oC may

have been too high and probably caused some electrical shunting at the p-n junctions due to Au diffusion to reduce the open-circuit voltage of the cell.

Photovoltaic I-V characteristics of the bonded GaAs/InGaAs dual-junction cell were measured with 0.337 cm^2 active illumination area under AM1.5 Global solar spectrum with 1-sun total intensity (100 mW cm^{-2}). For comparison, photovoltaic I-V characteristics of the unbonded GaAs and InGaAs subcells were also measured. Each of the subcells was processed in the same way as the bonded GaAs/InGaAs cell. The GaAs subcell was mounted on a handling glass substrate with gold film via conductive silver-epoxy glue, for its inversely-grown structure, and the original GaAs substrate was removed by the same chemical etching used for the bonded dual-junction cells. A cross-sectional schematic of this reference GaAs cell is shown in Figure 4.3. Regular plain smooth glass micro slides such as Corning 2947 with a thickness of ~1 mm were diced into ~ 1cm X 1cm size and 150 nm thick Au was deposited by thermal evaporation with a deposition rate of ~5 Å/s on the glass slides. The silver-epoxy glue was roughly a 1:1 (volume ratio) mixture of Epoxy Technology H20E-175 Part A and Part B, which bonded the inversely grown GaAs cells and the Au-deposited glass plates by being cured on a 180 ^oC hotplate for 2 hours in the atmosphere.

4-3. Results and discussion

Figures 4.4 and 4.5 show AFM images of the bonding surface of the GaAs top subcell and the InGaAs bottom subcell. The measured root-mean-square (RMS) roughness for each subcell was around 10 Å or a little less than that for both of the GaAs subcell and

the InGaAs subcell. This surface roughness was smooth enough to give successful direct wafer bonding, while other test cell samples with RMS roughness around 100 Å were not successfully bonded with similar process conditions. Additionally, the RMS roughness for the GaAs and InP commercial epi-ready wafers used for the wafer bonding study in Chapter 3 was 3-5 Å.

The photovoltaic I-V characteristics of the bonded GaAs/InGaAs dual-junction solar cell are shown in Figure 4.6 (inset). The device parameters for this cell were J_{sc} = 12.5 mA cm^{-2}, V_{oc} = 1.20 V, FF = 0.62, and η = 9.3 %, where J_{sc}, V_{oc}, FF and η are short-circuit current, open-circuit voltage, fill factor and energy conversion efficiency, respectively. The low fill factor may be accounted for by series resistance in the contacts, which can be lowered by contact redesign. The interfacial resistance for bulk GaAs/InP bonded under the conditions used for the cell was only around 10% of the total series resistance of the cell estimated from the photovoltaic I-V characteristics. The V_{oc}s of the unbonded GaAs and InGaAs subcells were 0.91 V and 0.27 V. Thus, the V_{oc} of the bonded GaAs/InGaAs dual-junction cell was approximately equal to the sum of the open circuit voltages for the GaAs and InGaAs subcells. This V_{oc} result indicates that the bonding process does not degrade the cell material quality since any generated crystal defects that act as recombination centers would reduce V_{oc}. [1, 2] Also, the bonded interface has no significant carrier recombination rate to reduce the open circuit voltage.

The spectral response for the bonded dual-junction cell and unbonded GaAs and InGaAs subcells is given in Figure 4.6. The bottom InGaAs subcell as well as the top GaAs

subcell of the bonded tandem cell was found to be photovoltaically active. This result indicates a highly transparent bonded GaAs/InGaAs interface. The result of the bonded cell is similar to the unbonded subcells in spectral response and indicates only a small loss of quantum efficiency (~10 %) by the cell stacking with direct wafer bonding. The poor quantum efficiency, specifically for the higher energy region, may be caused by a high surface recombination rate at the top surface. [3] Anti-reflective coating, surface passivation and optimization of cell assembly parameters, such as metal contacts and current matching, would give further improvement of the cell efficiency.

4-4. Conclusions

In this chapter, we demonstrated use of direct wafer bonding in a tandem solar cell for the first time. Such an approach can also be applied to other photovoltaic heterojunctions where lattice mismatch accommodation is also a challenge, such as the InGaP/GaAs/InGaAsP/InGaAs four-junction tandem cell, schematically shown in Figure 4.7, by bonding a GaAs-based lattice-matched InGaP/GaAs subcell to an InP-based lattice-matched InGaAsP/InGaAs subcell.

4-5. References

[1] R. B. Bergmann, *Appl. Phys. A* **69**, 187, 1999.

[2] R. Brendel, *Jpn. J. Appl. Phys.* **40**, 4431, 2001.

[3] K. A. Bertness, S. R. Kurtz, D. J. Friedman, A. E. Kibbler, C. Kramer, and J. M. Olson, *Appl. Phys. Lett.* **65**, 989, 1994.

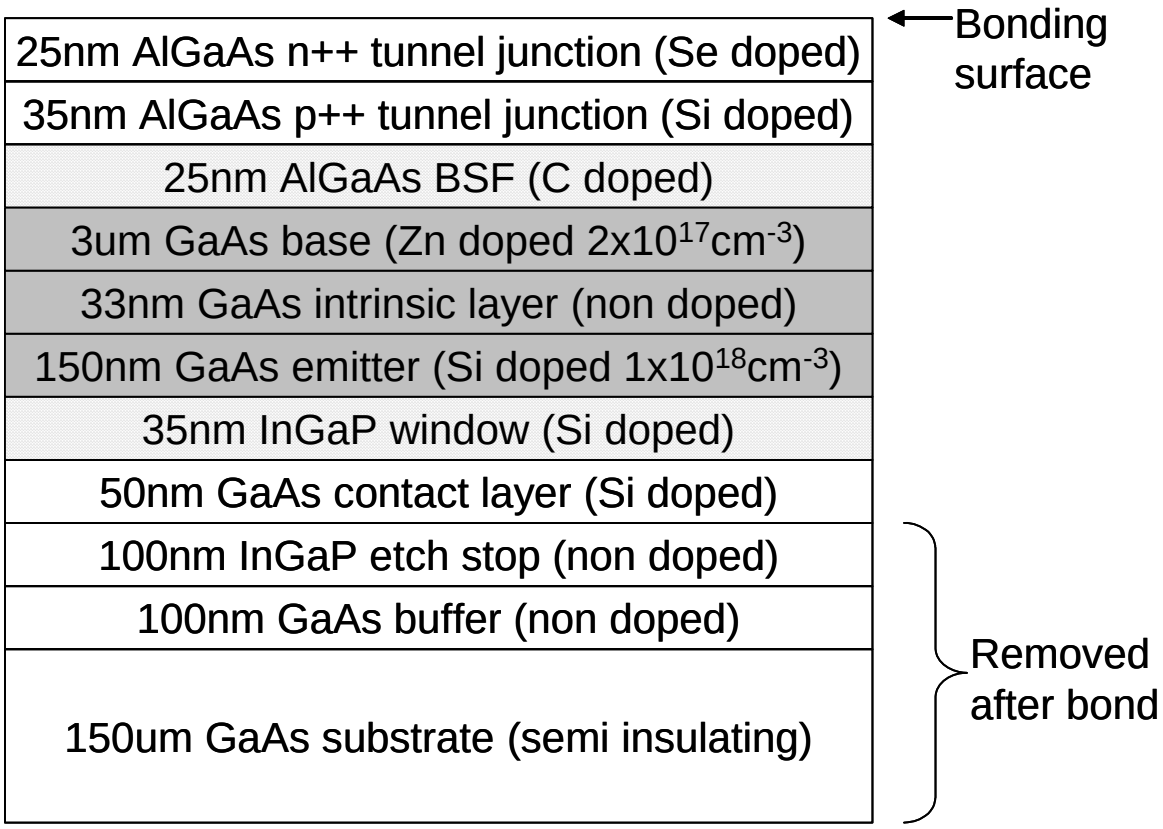
25nm AlGaAs n++ tunnel junction (Se doped)
35nm AlGaAs p++ tunnel junction (Si doped)
25nm AlGaAs BSF (C doped)
3um GaAs base (Zn doped 2x10^17cm^-3)
33nm GaAs intrinsic layer (non doped)
150nm GaAs emitter (Si doped 1x10^18cm^-3)
35nm InGaP window (Si doped)
50nm GaAs contact layer (Si doped)
100nm InGaP etch stop (non doped)
100nm GaAs buffer (non doped)
150um GaAs substrate (semi insulating)
Bonding surface
Removed after bond

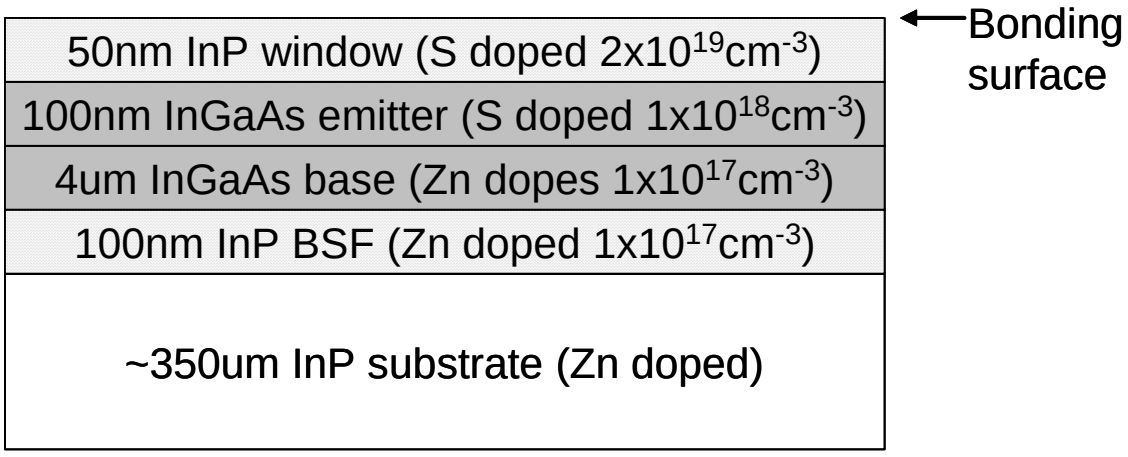

Fig. 4.1 Schematic cross-sectional diagrams for the (a) GaAs and (b) InGaAs subcells.

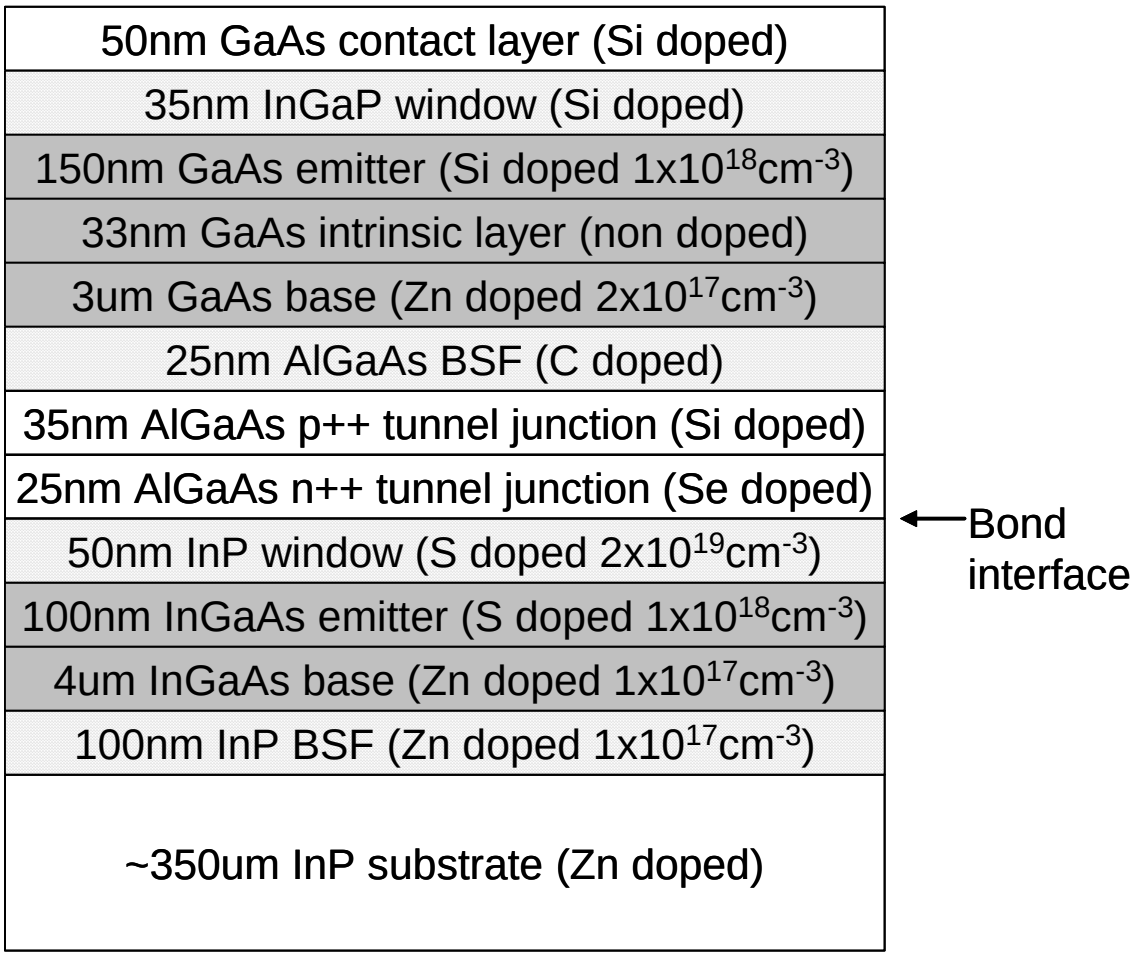

Fig. 4.2 Schematic cross-sectional diagram of the bonded dual-junction GaAs/InGaAs solar cell.

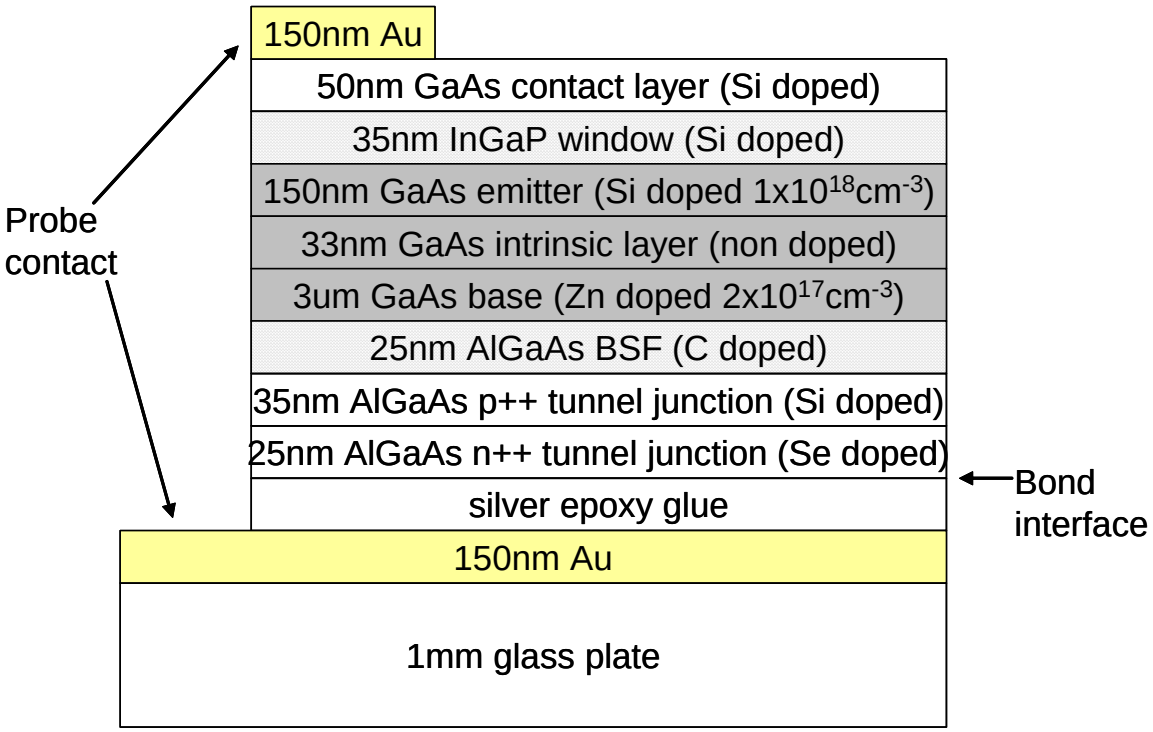

Fig. 4.3 Cross-sectional schematic of the reference GaAs cell.

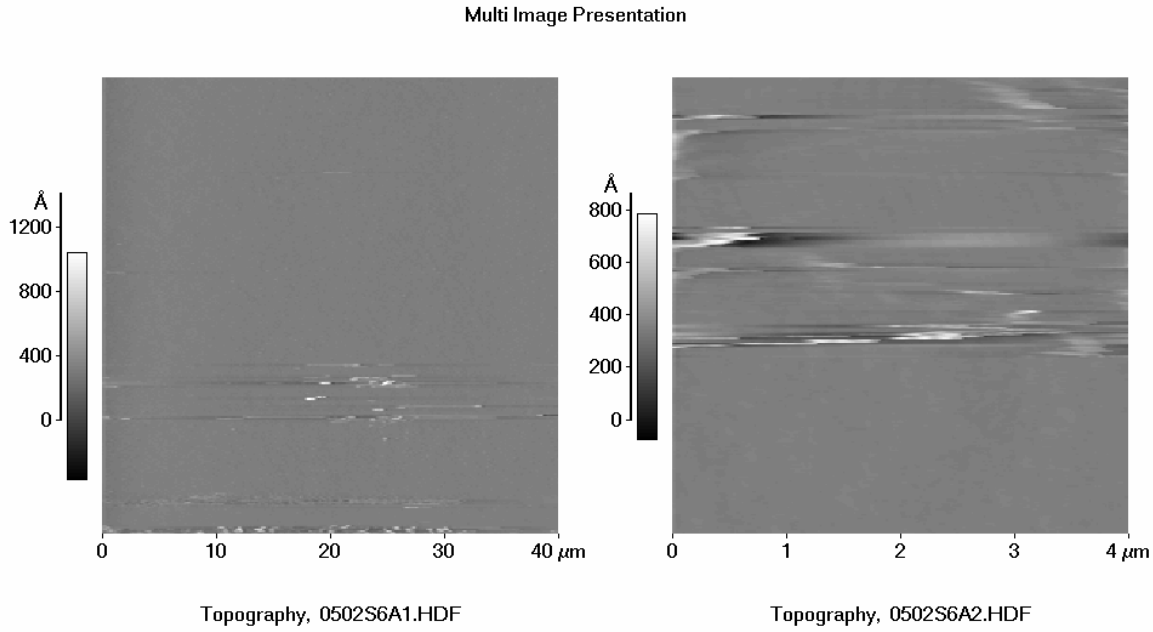

Fig. 4.4 AFM topological images of the bonding surface for the GaAs top subcell. The RMS roughness was around 10 A. Note that the abrupt horizontal lines are due to instrumental artificial noise and should be neglected.

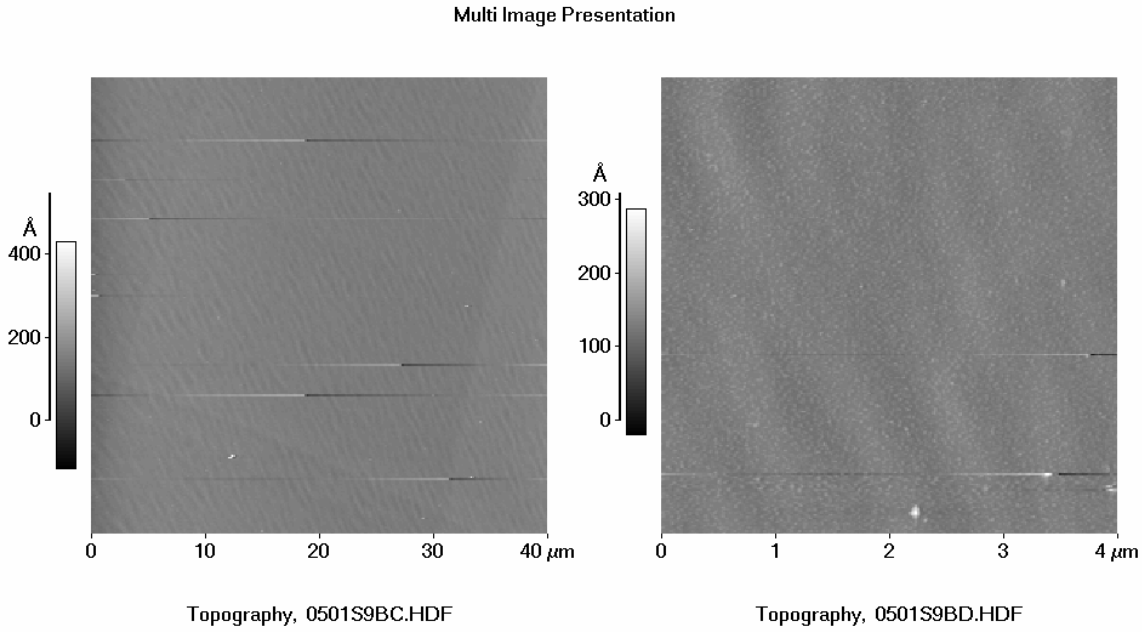

Fig. 4.5 AFM topological images of the bonding surface for the InGaAs bottom subcell. The RMS roughness was around 10 A. Note that the abrupt horizontal lines are due to instrumental artificial noise and should be neglected.

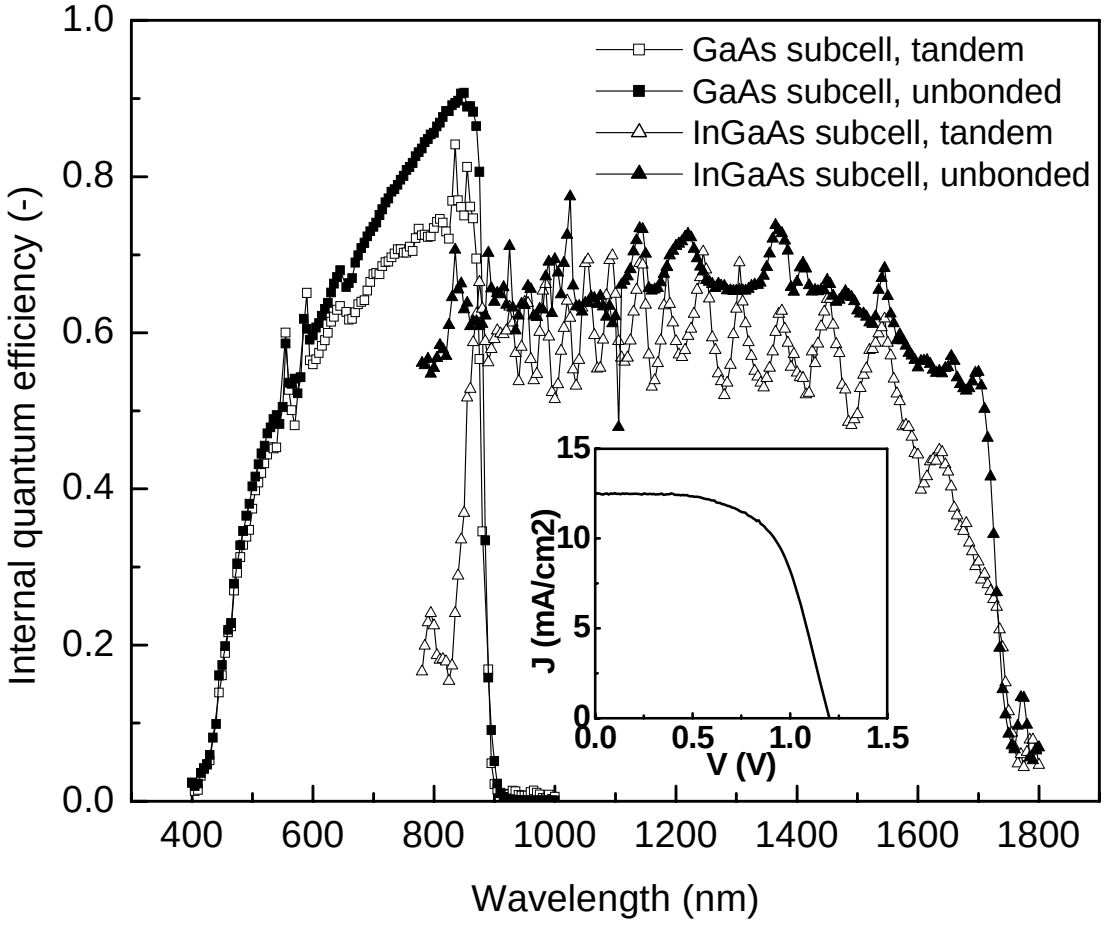

Fig. 4.6 Spectral response for the bonded GaAs/InGaAs dual-junction solar cell and unbonded GaAs and InGaAs subcells and (inset) I-V curve for the bonded GaAs/InGaAs solar cell at 1 sun, AM1.5G.

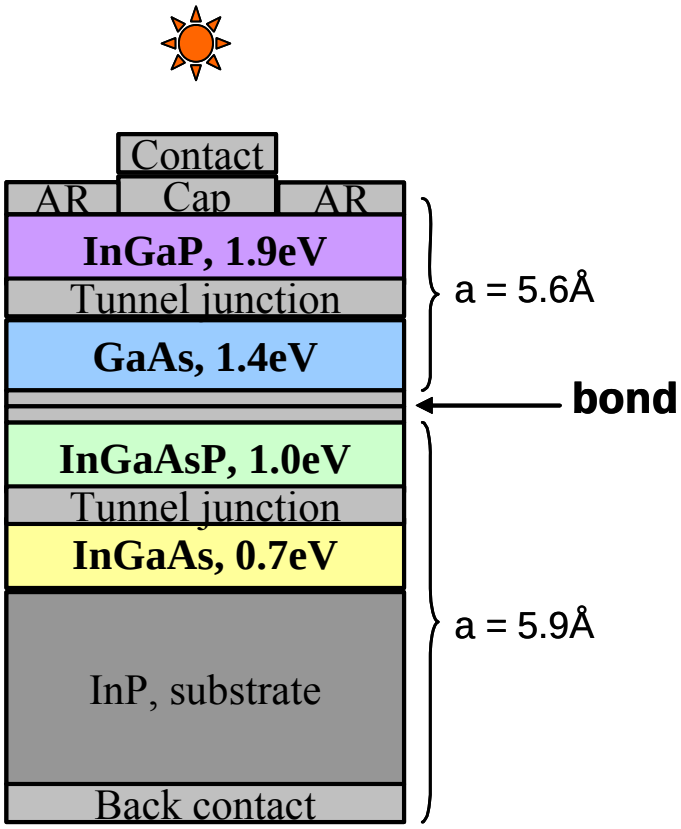

Fig. 4.7 Schematic cross-sectional diagram of an ultrahigh efficiency InGaP/GaAs/InGaAsP/InGaAs four-junction solar cell.

Chapter 5 InP/Si bonding and InP layer transfer

5-1. Introduction

In the previous chapters, I explained that multijunction solar cells of III-V semiconductor compounds exhibit very high energy conversion efficiencies. However, production cost is an important key factor as well as energy conversion efficiency for wide use of such solar cells specifically for terrestrial use. Let us take a look at the schematic diagram of the four-junction solar cell again in Figure 5.1. Simply looking at the thickness of each layer, we notice that the InP substrate dominates the most fraction of the total thickness of the cell with it's thickness of a couple of hundreds micron relative to the other layers of a couple of micron thick at most. Therefore we would like to reduce the cost of the InP substrate, which has a large fraction of the fabrication cost for the solar cell.

Engineered substrates consisting of thin films of InP on Si handle substrates (InP/Si substrates or epitaxial templates) have the potential to significantly reduce the cost and weight of compound semiconductor solar cells relative to those fabricated on bulk InP substrates. InGaAs solar cells on InP have superior performance to Ge cells at photon energies greater than 0.7 eV. The current record efficiency cell for 1 sun illumination was achieved using an InGaP/GaAs/InGaAs triple junction cell design with an InGaAs bottom cell [1]. Thermophotovoltaic (TPV) cells from the InGaAsP-family of III-V materials grown epitaxially on InP substrates would also benefit from such an InP/Si substrate [2]. Substitution of InP/Si substrates for bulk InP in the fabrication of such a

four-junction solar cell could significantly reduce the substrate cost. For example, typical price of a 4-inch InP wafer is ~$1000/wafer, relative to ~$10/wafer for a 4-inch Si wafer, as of Aug. 2007. Switching the major part of growth substrates from InP or other III-V materials into Si also has such advantages as follows. Si is mechanically more robust than III-V semiconductor compound materials. Si has higher thermal conductivity than III-V materials do and therefore would have less energy conversion efficiency loss due to increased temperature of solar cells specifically for optical concentrator use. Si has lighter (~1/2) weight than III-V materials do, which would particularly be a benefit for space use.

Direct heteroepitaxial growth of InP thin films on Si substrates has not produced the low dislocation-density high quality layers required for active InGaAs/InP in optoelectronic devices due to the ~8% lattice mismatch between InP and Si [3]. Wafer bonding on the other hand is not subject to lattice matching limitations associated with epitaxial growth, and has been used to fabricate materials that consist of crystalline semiconductors on amorphous materials and also to integrate crystalline materials of different lattice constants. For the integration of both crystalline-amorphous and crystalline-crystalline pairs, defects caused by the lack of crystallographic registry are isolated to the wafer-bonded interface. Thus, provided the wafer-bonded interface does not play an active role in the operation of the device, the independent materials and devices fabricated in them can in principle have performance typical of devices made on or in the bulk material.

Layer transfer of a high quality single crystal InP film onto a Si bulk substrate can be accomplished through wafer bonding of InP to Si and exfoliation of a thin film from the InP wafer induced by implantation of light elements such as hydrogen and helium [4-6]. The implantation process results in a high density of point defects near the region where exfoliation occurs, however most of this region can be removed by thinning the transferred film. Furthermore, the point defects generated by the implantation process have previously been shown to have minimal impact on the quality of InP grown on transferred thin films of InP [7]. This is likely because during the epitaxial process, vacancies in the growth surface are occupied by the appropriate anion or cation adatom. Because only a few μm of InP are consumed in the transfer of a film and subsequent reclaim of the InP substrate, a single InP wafer could be reused repeatedly to generate many InP/Si substrates, thus reducing the material cost of InP in devices grown on those substrates.

Overview of this study

First I fabricated InP/Si direct-bonded, layer-transferred epitaxial substrates, but delamination in the MOCVD growth process is observed. Aonex Technologies, Inc., one of my collaborators and whom I have been sharing technical information with each other throughout this project, successfully made InP/SiO_2/Si substrates and were good in the growth of InGaAs solar cells. For the detail of the InGaAs solar cell growth on the prepared InP/SiO_2/Si substrates and cells' characterization will be described in the following chapter.

5-2. InP/Si direct-bonded alternative substrate

5-2-1. Experimental

Ion-implantation-induced exfoliation of InP

The basic process schematic for the InP layer transfer to fabricate alternative InP/Si epitaxial substrate (epitaxial templates) is shown in Figure 5.2. Epi-ready p-type (Zn doped) 2-inch InP (100) wafers with doping concentration of $4x10^{18}$ cm^{-3} were purchased from InPACT, Inc. He^+ and H^+ ions were implanted into the doses of $1x10^{17}$ cm^{-2} and $1.5x10^{16}$ cm^{-2}, respectively, with implantation energies and currents of 115 keV, 80 μA and 80 keV, 150 μA, respectively. The implantation was done into the polished side of the InP wafers. The ion implantation was done by Leonard J. Kroko, Inc. These implantation doses and currents were carefully chosen through trial and error based on the two points:

1. The implantation dose has to be large enough to exfoliate the InP wafers in the following bonding/annealing process
2. The implantation current has to be low enough to avoid partial exfoliation of the InP wafers due to the accumulated heat by implantation energy flux

Therefore, ideally it would be better to have higher implantation dose and lower implantation current. However the process time, which is proportional to implantation dose divided by implantation current, reflects the implantation cost and therefore those two parameters had to be optimized. The implantation energies or voltages determines the implantation depth and were chosen to give ~1 um implantation depth for both of He^+ and H^+ using SRIM, a Monte-Carlo simulation package for implantation depth profiles. For this study, p-type InP wafers were mainly used since III-V semiconductor compound

solar cells are typically grown to n-type photovoltaic active layers at the top and p-type layers at the bottom. It should be however noted that I succeeded in layer transfer also of n-type (S doped) InP with the same process conditions. I have not investigated deeply, but helium-only implantation may also work, as seen in the InP/SiO_2/Si substrate fabrication by Aonex Technologies, Inc. described in the following section.

Wafer bonding and layer transfer

p-type conductive (doping concentration > $1x10^{18}$ cm^{-3}) Si (001) epi-ready wafers were used as the supporting substrate. After implantation, the InP wafers were first coated with photoresist (Shipley 1813) with a spincoater with a spinning velocity 3000 rpm for 1 min followed by soft bake at 115 ^oC for 90 sec. This photoresist coating is to protect the bonding surface of InP from particles generate in the following dicing process because interfacial particles would degrade the bonding strength. The wafers were then diced into quarters of the original 2 inch diameter size. Then the applied photoresist was removed sequentially dipped in acetone for 10 min and then in methanol for 10 min, and rinsed with D. I. (de-ionized) water. This series of washing process has also a function of surface degreasing, as well as photoresist removal. Then the native oxide was removed by dipping both the InP and Si wafers in 10 vol%-HF (aq) for 30 sec. At this point, both of the GaAs and InP wafers are observed to be highly hydrophobic. Surface activation by oxygen plasma was also tested, but this surface treatment prior to wafer bonding oxidized the wafers and made the two wafer surfaces to be bonded repulsive like same polarity of magnets and therefore was not adopted in this study. Then the wafers were brought into contact with their polished sides face to face with the (011) edges aligned. The joined

InP/Si pair was annealed at ~1 MPa at 400 ^{o}C in atmosphere for 10 hours to make InP/Si bond and also to exfoliate an InP thin film by thermal expansion of the implanted ions. The wafer bonding facility used in this study was same as the one used in Chapters 3 and 4 and its photograph is shown in Figure 3.1 in Chapter 3. As the result of this process, a structure of a ~900 nm thick InP thin film bonded on top of a Si substrate is obtained, as its photograph is shown in Figure 5.3. Because of the quite thin thickness of the exfoliated InP film, in principle we could fabricate hundreds of the alternative InP/Si epitaxial substrates from a single InP wafer, which has potential of a significant production cost reduction of III-V semiconductor compound solar cells.

Smoothening of InP surface

The as-transferred InP/Si alternative substrates have rough InP surface inappropriate for subsequent epitaxial growth. Also, due to the implantation-induced damage around at the exfoliation surface in InP wafers, removal of such damage region is needed for proper subsequent epitaxial growth. [5, 8] I therefore attempted to remove the damage region as well as smoothening the InP surface by using chemical etching and also by chemical mechanical polishing (CMP). Chemical etching was carried out using combinations of oxidizers such as H_2O_2, dissolving strong acids such as HCl and diluents such as H_3PO_4 at room temperature. CMP process was carried out using a PM5 polisher (Logitec, Inc.) with a soft polyurethane polishing pad ("Politex" cloth, Eminess Technologies, Inc.) rotated at ~10 rpm using (chemicals) with an applied pressure of ~50 kPa in the Nanofabrication Laboratory in UCLA. The InP/Si substrates were mounted on either a 4-inch glass plate or silicon wafer via crystal bond and then attached to a wafer jig. A

chemical solution consisting of 1:10 (vol.) sodium hypochlorite (NaOCl) (5-6% aq.) - H_2O and 1:2 (vol.) citric acid ($C_6H_8O_7$) (10% aq.) -H_2O was regularly applied to the polishing pad to assist polishing. [9] No abrasive particle was used.

Contact-mode atomic force microscopy (AFM) measurement was used to determine the surface roughness for the as-transferred and smoothened InP surface of the InP/Si alternative substrates.

InGaAs growth on the InP/Si alternative substrates

To test the quality of the fabricated InP/Si alternative substrate as an epitaxial growth substrate relative to bulk InP substrates, lattice-matched InP/$In_{0.53}Ga_{0.47}As$/InP double heterostructures (DHs) were grown with metalorganic chemical vapor deposition (MOCVD). This MOCVD growth was done by Daniel Law at Spectrolab, Inc. The DHs were grown simultaneously on the layer-transferred (100) InP / (100) Si structures and also on a bulk (100) InP control wafer. The InP/InGaAs/InP DH was capped by an InGaAs layer.

5-2-2. Results and discussion

Smoothening of InP surface

Figure 5.4 shows a typical AFM topological image for InP surface of the as-transferred InP/Si alternative substrate. The measured root-mean-square (RMS) roughness was around 100 Å, which is much larger than the typical value for epi-ready substrates, 1-10 Å. Therefore I tried to smoothen this rough surface for subsequent epitaxial growth by

using liquid-phase chemical etching and chemical mechanical polishing (CMP) techniques.

Chemical etching solutions for III-V and IV group semiconductors such as GaAs, InP, Si and Ge commonly consist of oxidizers to first form semiconductor oxide solvable with acids, acids to dissolve the semiconductor oxide and diluents, typically weak acids, to adjust the etching rate and surface roughness. For the case of InP etching and smoothening, first $InPO_4$ or In_2O_3 is formed at the surface of InP by an oxidizer such as H_2O_2 and then this oxide is dissolved by a strong acid such as HCl, as schematically depicted in Figure 5.5. [10, 11]

Table 5.1 shows the list of the chemical solutions used in this study for InP smoothening. Out of this list, only HCl-H_2O_2-H_3PO_4 [11-14] and HCl-H_2O_2-CH_3COOH [15-17] were found to exhibit notable smoothening effect. AFM images for the morphological evolution of the InP surface by the HCl-H_2O_2-H_3PO_4 etching is shown in Figure 5.6. The finished RMS roughness of the InP surface was ~30 Å for both 1:2:2 (volume fraction) solution at the point of 1 min dip and 1:7:2 solution at 1 min or later. The etching rate was determined to be 360 nm/min and 35 nm/min for 1:2:2 and 1:7:2 solutions, respectively. 1:7:2 HCl-H_2O_2-CH_3COOH solution (40 nm/min) also resulted in ~30 Å RMS roughness at 4 min, while no smoothening was observed for 1:2:2 HCl-H_2O_2-CH_3COOH (1300 nm/min). Dilution of the acid (dissolver) seemingly gives more or less smoother etching. This result can be attributed to mass-transfer-limited chemical reaction, where etch rates at peaks are higher than etch rates at valleys and hence the surface is

smoothened. Larger oxidizer fraction relative to acid may also have higher smoothening effect due to dissolution-limited circumstance since oxidation process is more sensitive to electron concentration, surface orientation, crystal defects and so forth, which would cause higher areal nonuniformity for etching rate. [18, 19]

As described above, proper chemical etching could successfully smoothen the InP surface of the InP/Si alternative substrate down to RMS roughness ~30 Å relative to ~100 Å as layer-transferred. However, this roughness is still not quite ideal for subsequent epitaxial growth compared with 1-10 Å RMS roughness for commercial ”epi-ready” bulk substrates. Therefore, I also tried chemical mechanical polishing (CMP), which is commonly used in semiconductor industry for epi-ready surface preparation. Figure 5.7 shows AFM topological images for some of the successful resulted InP surface of the InP/Si substrates. RMS roughness as small as 3 Å at best has been achieved. Etch pits were occasionally found presumably stemming from intrinsic etch pits existing in the InP wafers selectively etched in CMP. This obtained RMS roughness is quite comparable to the commercially-available “epi-ready” grade semiconductor substrates, which means appropriate for epitaxial growth. It should be however noted that CMP process has somehow poor reproducibility for resulted surface. The polishing rate and areal uniformity are very sensitive to the condition and only a slight difference of the process condition we would not notice could give a drastic difference to the result. Therefore it is crucial to choose stable conditions for CMP operation through trials.

Growth of InP/InGaAs double heterostructures

Figure 5.8 (a) and (b) show typical cross-sectional scanning electron microscopy (SEM) images for the grown InP/InGaAs DH on the InP/Si substrate. Also shown in Figure 5.9 (a) and (b) are optical photographs of an InP/Si substrate etched by HCl-H_3PO_4-H_2O_2 (1:2:2 vol.) for 20 sec before and after InP/InGaAs DH growth, respectively. It was found that a significant fraction of the grown InP/InGaAs DH film is delaminated from the InP/Si substrate, as also seen in Figure 5.8 (b).

This delamination of the growth films is attributed to the mismatch of the coefficients of thermal expansion (CTE) between InP and Si. Figure 5.10 shows the thermal expansion of semiconductor materials. [20] As seen in Figure 5.10, the InP film will have compressive strain from the Si substrate due to temperature increment for the MOCVD growth from the bonding temperature since the thermal expansion slope is larger for InP than Si and then tensile strain as the temperature goes down to room temperature after the growth. The film delamination is considered to have happened either or both of these heating or/and cooling process due to the strain in the film.

There are a couple of potential solutions to this film delamination problem, such as insertion of a bonding layer to accommodate the CTE mismatch, thinning the InP film to give flexibility to endure the strain, bonding initiation at higher temperature, and reduction of growth temperature. Successful InGaAs growth on InP/Si alternative substrates was achieved using SiO_2 bonding layer by a research team at Aonex Technologies, Inc., one of my collaborators, which is described in the next section.

5-3. InP/SiO_2/Si substrates

5-3-1. Experimental

InP (001) substrates and thermally oxidized Si (001) handle substrates were used for the fabrication of InP/Si substrates for growth of InGaAs solar cell test structures. However, experiments were also conducted with Si (001) substrates that had been coated with a silicon dioxide (SiO_2) film using plasma-enhanced chemical vapor deposition (PECVD) from a tetraethyl orthosilicate (TEOS) precursor. The PECVD oxide was subsequently densified by annealing and subjected to a chemical mechanical polish (CMP) to give a particle-free smooth bonding surface. Use of a SiO_2 film was found to improve the thermal stability of the bonded interface relative to structures fabricated with a direct semiconductor-semiconductor bond. InP/Si substrates fabricated with handle substrates having thermal or CVD-deposited oxides resulted in >90% layer transfer and good subsequent thermal stability. The first step in the InP/Si substrate fabrication was the ion implantation of the InP wafer with He^+ at an energy between 115 and 180 keV to a dose of at least $1.0x10^{17}$ cm^{-2}. Prior to wafer bonding the surfaces of both the InP and the Si handle substrates were prepared by wet chemical cleaning to remove organic and particulate contamination followed by activation of the bonding surfaces with an atmospheric pressure plasma exposure. Bonding between the InP and the Si handle was then initiated at a temperature of 150 ^oC or greater. The two substrates were then annealed under uniaxial pressure greater than 1 MPa to promote the formation of covalent bonds between the InP and Si substrates and induce the exfoliation of a thin layer (~900 nm) of InP thus forming the InP/Si substrate. A typical image of an InP/Si substrate fabricated by transferring a thin InP film to a Si substrate with a SiO_2 bonding

layer is shown in Figure 5.11. The film was transferred from an InP substrate implanted with He^+ to a dose of $1.0x10^{17}$ cm^{-2} at an energy of 180 keV.

5-3-2. Results and discussion

The ion implantation induced exfoliation process results in lattice damage in the transferred film with a damage peak roughly coinciding with region where exfoliation occurs. Thus, in the as-transferred InP/Si structure there is a distribution of lattice defects with a peak at the surface of the transferred film decreasing to a minimum defect density in the material adjacent to the bonded interface. Figure 5.12 shows a representative cross-sectional transmission electron (XTEM) micrograph of a film transferred from InP implanted with 115 keV He^+ to a dose of $1.0x10^{17}$ cm^{-2}. The inset selected area diffraction (SAD) pattern shows that the InP adjacent to the bonded interface is single-crystalline. Close inspection of the defect structure using high-resolution XTEM imaging showed that the strain contrast is caused by a both extended defects that can be directly imaged and point defects such as vacancies and interstitials. It is essential that the damage in the as-transferred InP thin film in InP/Si engineered substrates be minimized prior to epitaxial growth of III-V materials. In particular, extended defects that intersect the growth surface are problematic for growth. For the InP/Si substrates used for growth of InGaAs test cells, the damaged surface region of the as-transferred InP film was removed leaving a film of ~400 nm thickness. The transferred films were thinned using a combination of inductively-coupled plasma reactive ion etching (ICP-RIE) for damage removal and a wet chemical etch for surface smoothing. Contact-mode atomic force microscopy (AFM) measurements of the InP/Si substrates showed that the as-transferred

roughness of >100 Å RMS was reduced to 50-100 Å RMS following the etching process. More importantly, the most heavily damaged material at the surface of the InP transferred layer was removed.

On contrast to my InP/Si direct-bonded structures, this InP/SiO2/Si structure exhibited significantly higher stability in the high-temperature (~650 ^{o}C) MOCVD process and resulted in no delamination of the InP transferred thin film part. The SiO_2 of the bonding layer is amorphous and absorbs contaminations such as light gases at the bonded interface, which would otherwise be a cause of debonding or delamination by generating gas bubbles, due to the high diffusivity and solubility of light gases in amorphous SiO_2. We chose SiO_2 as the bonding layer also because SiO_2 can be easily formed on Si wafers and activation techniques for bonding SiO_2 surface has been well established.

5-4. Conclusions

800nm-thick InP thin films were successfully layer-transferred onto Si substrates through hydrogen/helium induced exfoliation as low-cost epitaxial templates. Both of conductive p-type/p-type and n-type/n-type of InP/Si structures were prepared, which are applicable for solar-cell applications. Surface roughness of as-transferred InP films was around 100 Å, which was not ideal for subsequent epitaxial growth. This InP surface roughness was improved through chemical etching and CMP (Chemical Mechanical Polishing). Chemical etchants including oxidizer, dissolving acid, weak-acid diluent were found to smoothen the InP surface down to 30 Å RMS from 100 Å of as-transferred films.

Furthermore, less-than-10 Å RMS was achieved by CMP.

At this point, this approach of direct-bonded InP/Si substrate structures have not been successful yet as seen in the delamination of InP films in MOCVD due to the thermal expansion mismatch between InP and Si. However, if we could enhance the interfacial strength and stand in the growth process by such methods as thinning the InP film to give flexibility to endure the strain, bonding initiation at higher temperature, and reduction of growth temperature, InP/Si direct-bonded substrates would be more useful than the InP/SiO_2/Si substrates since InP/Si substrates have conductive bonded interface and therefore can take front/back metal contact configuration for the cell fabrication, not the complicated front/front configuration.

InP/SiO_2/Si substrates with PECVD-deposited SiO_2 layers on Si were also successfully fabricated and they were thermally more stable than the InP/Si substrates, enough to survive in the MOCVD process for InGaAs growth without delamination of the InP film, which indicates a feasible thermal stability of this alternative substrate for III-V semiconductor compound solar cell growth.

5-5. References

[1] J. F. Geisz, S. R. Kurtz, M. W. Wanlass, J. S. Ward, A. Duda, D. J. Friedman, J. M. Olson, W. E. McMahon, T. E. Moriarty, and J. T. Kiehl, *Appl. Phys. Lett.* **91**, 023502, 2007.

[2] M. W. Wanlass, J. S. Ward, K. A. Emery, M. M. Al-Jassim, K. M. Jones, and T. J. Coutts, *Sol. Ener. Sol. Cell.* **41**, 405, 1996.

[3] M. Sugo, Y. Takanashi, M. M. Al-Jassim, and M. Yamaguchi, *J. Appl. Phys.* **68**, 540, 1990.

[4] Q. Y. Tong, Y. L. Chao, L. J. Huang, and U. Gosele, *Electron. Lett.* **35**, 341, 1999.

[5] A. Fontcuberta i Morral, J. M. Zahler, S. P. Ahrenkiel, M. W. Wanlass, and H. A. Atwater, *Appl. Phys. Lett.* **83**, 5413, 2003.

[6] A. Fontcuberta i Morral, J. M. Zahler, M. J. Griggs, H. A. Atwater, and Y. J. Chabal, *Phys. Rev. B* **72**, 085219, 2005.

[7] S. Hayashi, R. Sandhu, M. Wojtowicz, G. Chen, R. Hicks, M. S. Goorsky, *J. Appl. Phys.* **98**, 093526, 2005.

[8] J. M. Zahler et al, *Appl. Phys. Lett.* **91**, 012108, 2007.

[9] S. Hayashi et al, *Proc. 16th International Conference on Indium Phosphide and Related Materials*, May 31 - June 4, Kagoshima, Japan, 358-361, 2004.

[10] A. Mouton et al, *Jpn. J. Appl. Phys.* **29** (10), 1912, 1990.

[11] X. Cao and I. Thayne, *Microelect. Eng.* **67-68**, 333, 2003.

[12] S. Uekusa et al, *J. Electrochem. Soc.* **132** (3), 671, 1985.

[13] P. Buchmann and A. J. N. Houghton, *Electron. Lett.* **18**, 850, 1982.

[14] A. Fontcuberta i Morral, private communication.

[15] K. Iga et al, *Jpn. J. Appl. Phys.* **18** (10), 2035, 1979.

[16] E. I. Miller and K. Iga, *Appl. Phys. Lett.* **37** (4), 339, 1980.

[17] T. Kambayashi et al, *Jpn. J. Appl. Phys.* **19** (1), 79, 1980.

[18] B. Schwartz and H. Robbins, *J. Electrochem. Soc.* **123** (12), 1903, 1976.

[19] M. S. Kulkarni and H. F. Erk, *J. Electrochem. Soc.* **147** (1), 176, 2000.

[20] Y. Touloukian, ed., *Thermophysical properties of matter*, IFI/Plenum, New York, 1970.

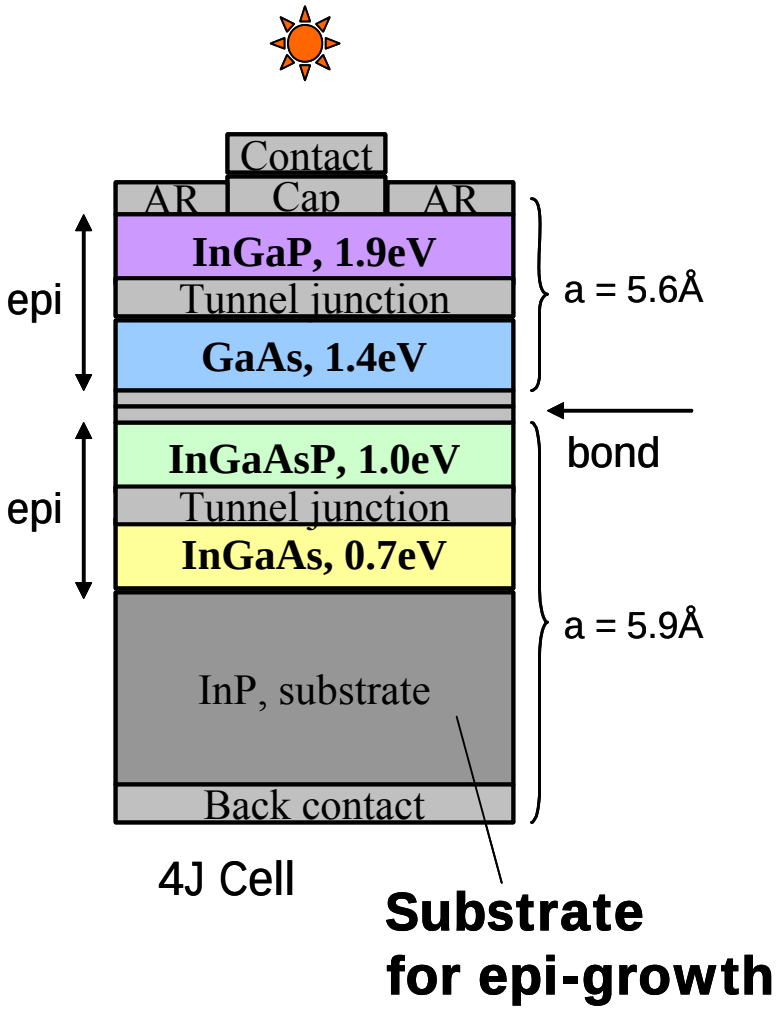

Fig. 5.1 Schematic cross-sectional diagram of a InGaP/GaAs/InGaAsP/InGaAs four-junction solar cell.

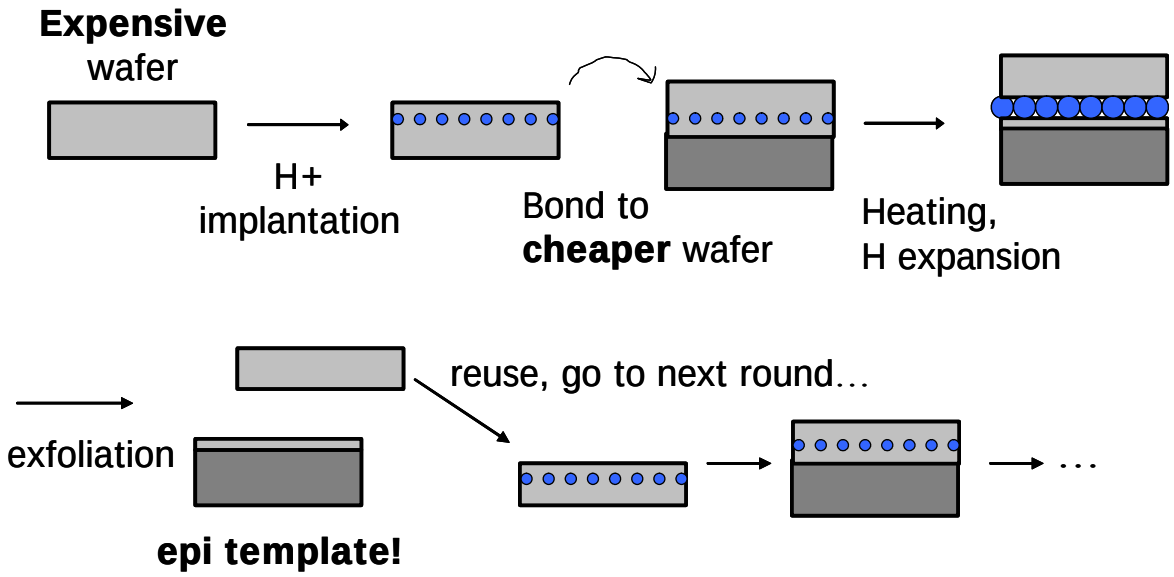

Fig. 5.2 Schematic of the layer transfer process.

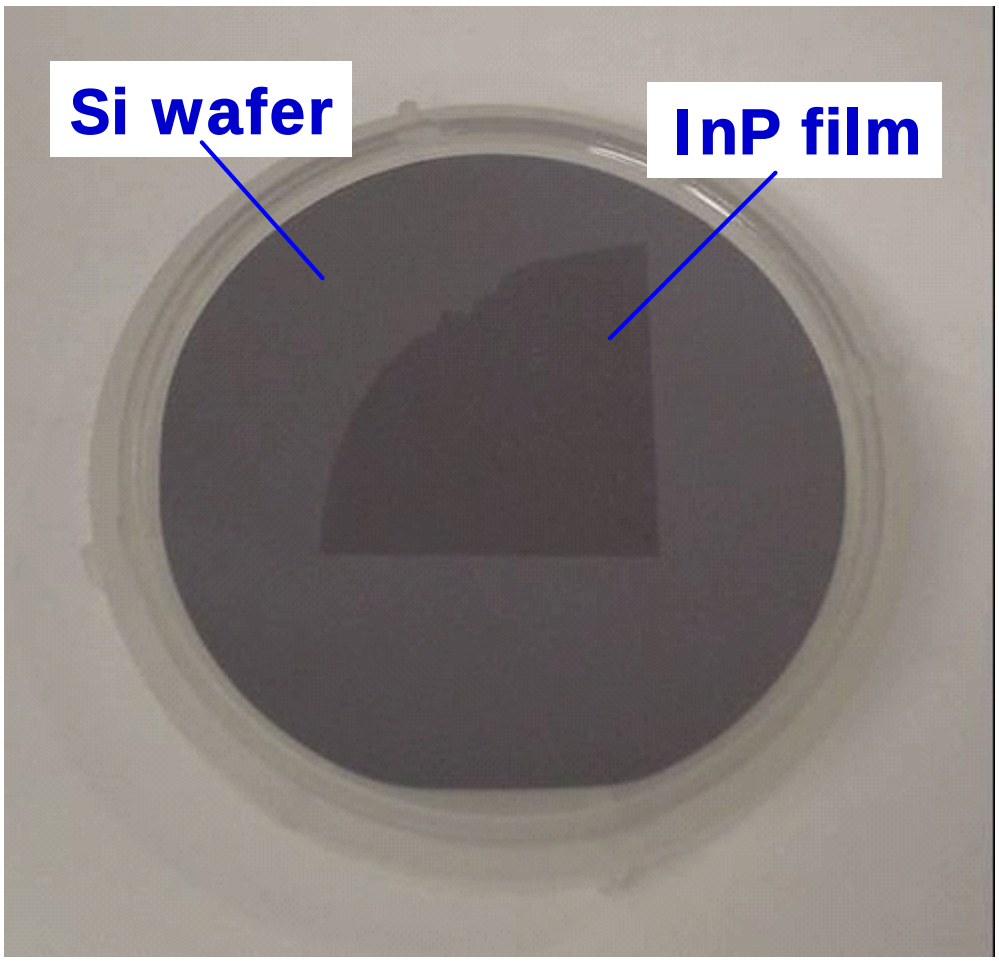

Fig. 5.3 Photograph of a layer-transferred InP/Si alternative substrate.

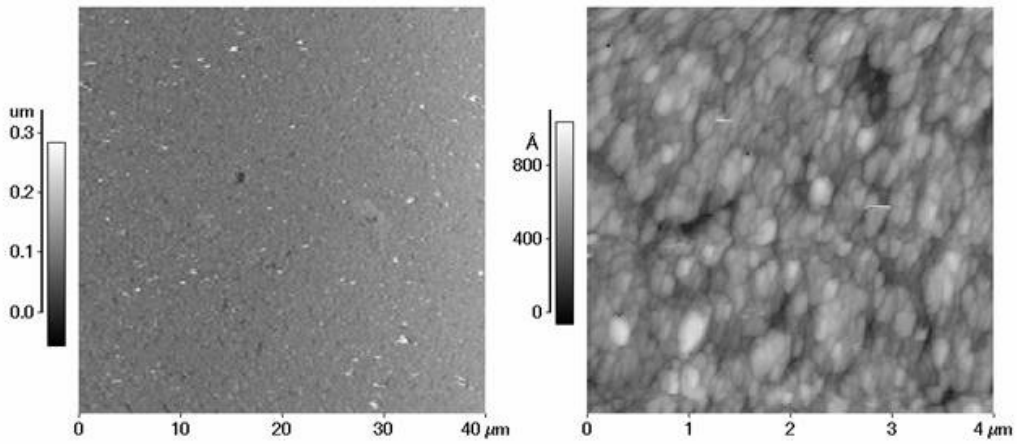

Fig. 5.4 Typical AFM topological image for InP surface of the as-transferred InP/Si alternative substrate.

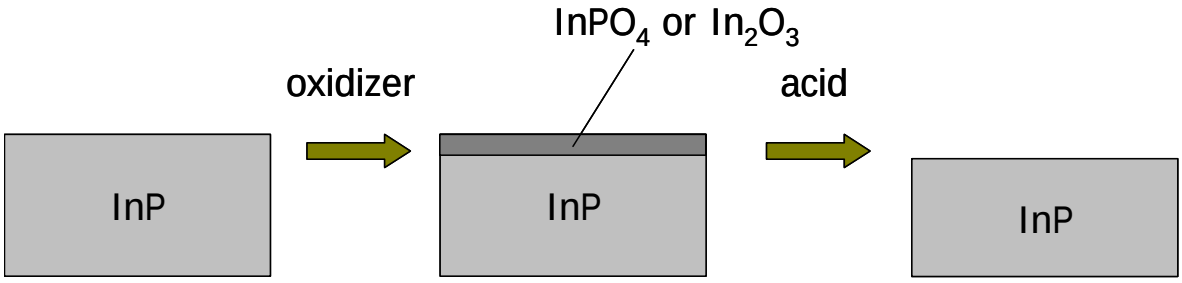

Fig. 5.5 Schematic flow of InP chemical etching.

agent 1	agent 2	agent 3
HCl	H2O2	H3PO4
HCl	H2O2	CH3COOH
HF	H2O2	CH3COOH
HF	H2O2	H3PO4
HCl	H3PO4	CH3COOH

Table 5.1 List of the chemical solutions for InP smoothening used in this study. Agent 1, 2 and 3 are dissolver, oxidizer and diluent, respectively.

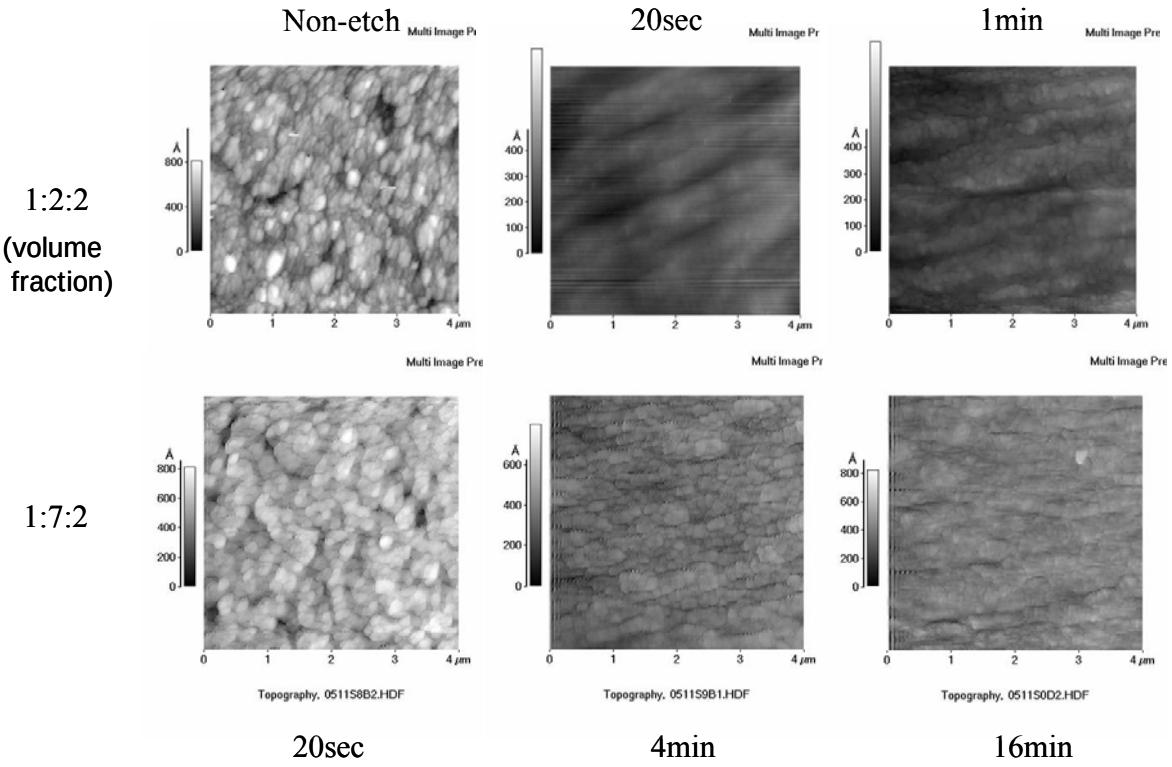

Fig. 5.6 AFM images for the morphological evolution of the InP surface by the HCl-H_2O_2-H_3PO_4 etching. Note that the scale ranges are set to be equal among images.

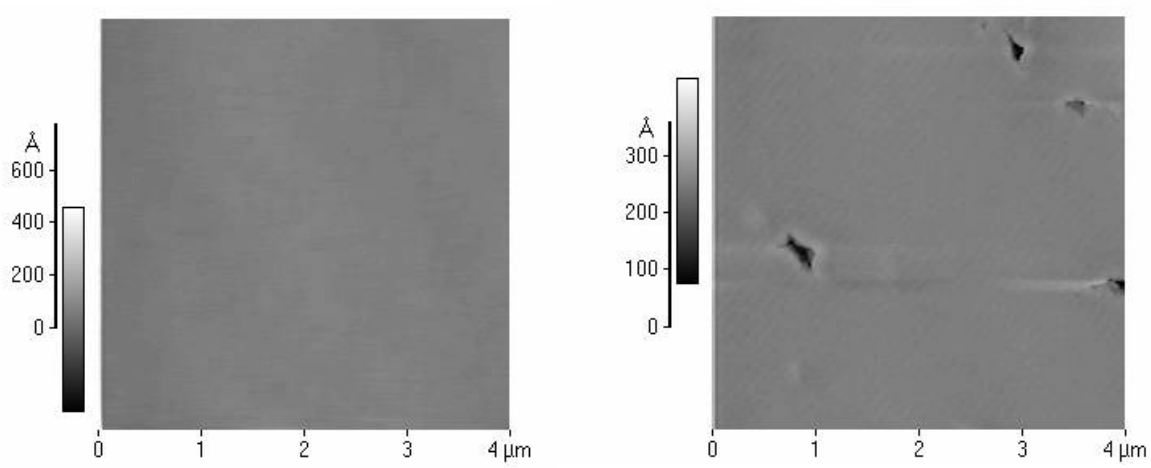

Fig. 5.7 AFM topological images for successfully smoothened InP surface of InP/Si alternative substrates by CMP. RMS roughness was 3-5 A. (Right) Etch pits were occasionally found presumably stemming from intrinsic etch pits existing in the InP wafers selectively strongly etched in CMP.

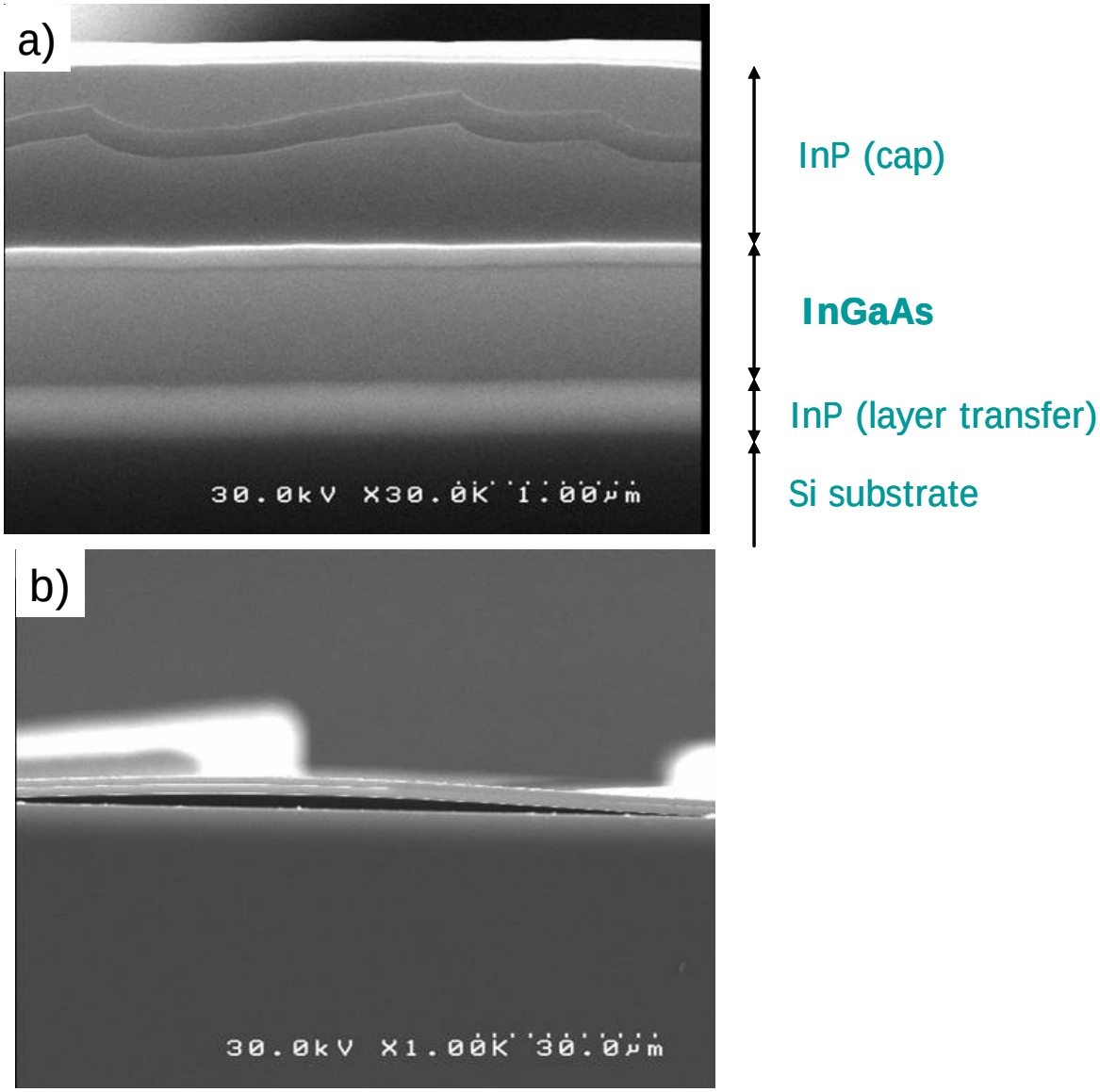

Fig. 5.8 Cross-sectional scanning electron microscopy (SEM) images for the grown InP/InGaAs DH on the InP/Si substrate.

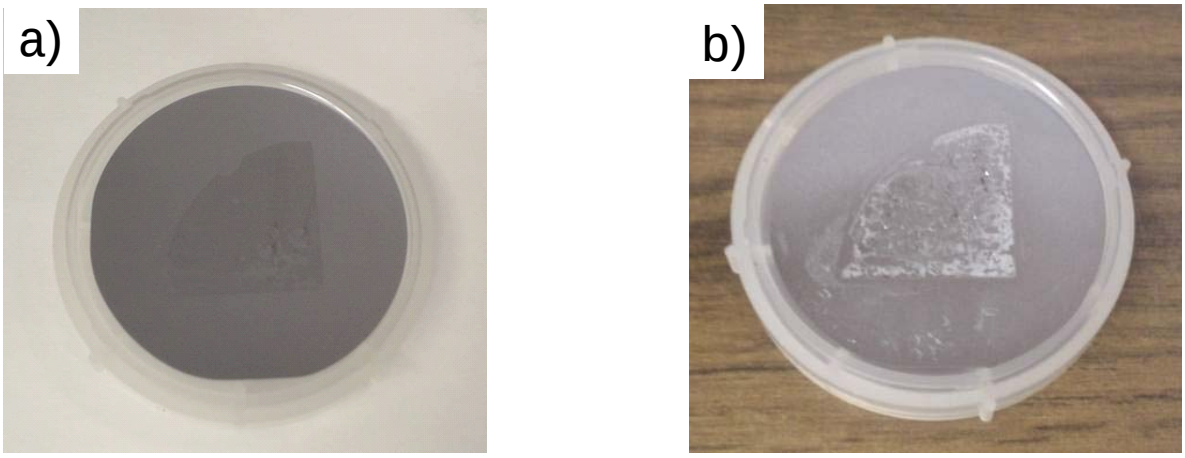

Fig. 5.9 Optical photographs of an InP/Si substrate etched by HCl-H_3PO_4-H_2O_2 (1:2:2 vol.) for 20 sec (a) before and (b) after InP/InGaAs DH growth.

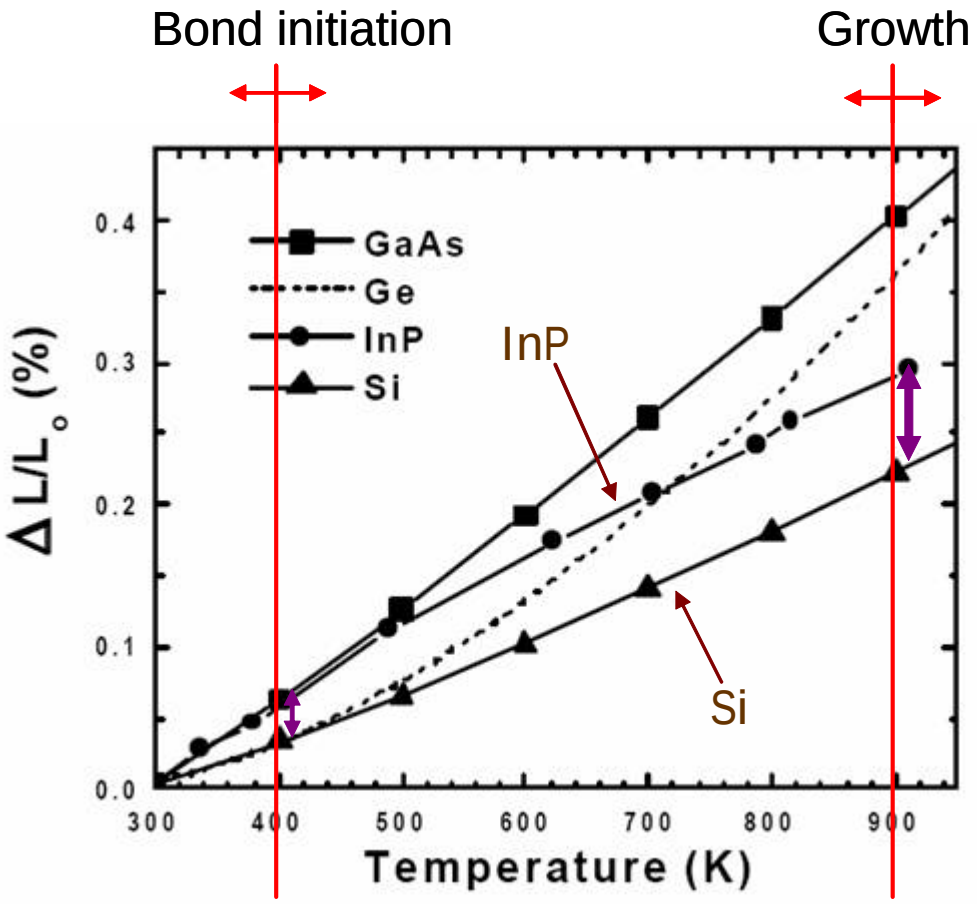

Fig. 5.10 Thermal expansion of semiconductor materials.

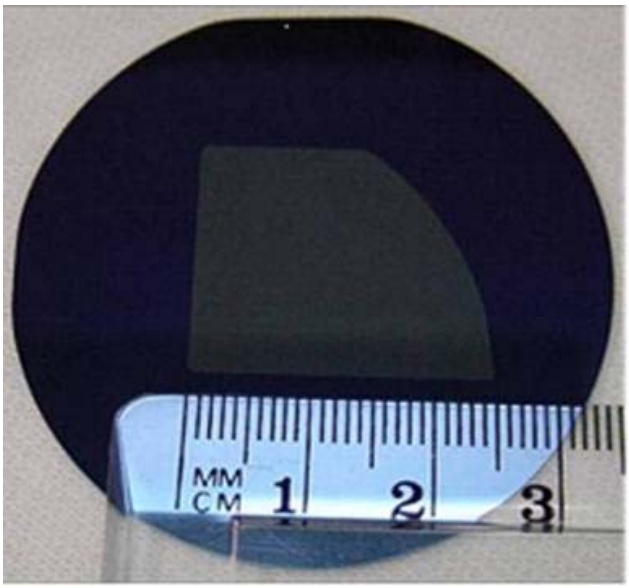

Fig. 5.11 Optical micrograph of a layer-transferred InP/Si substrate; one-quarter of a 50 mm diameter InP layer was transferred onto a 50 mm diameter Si substrate.

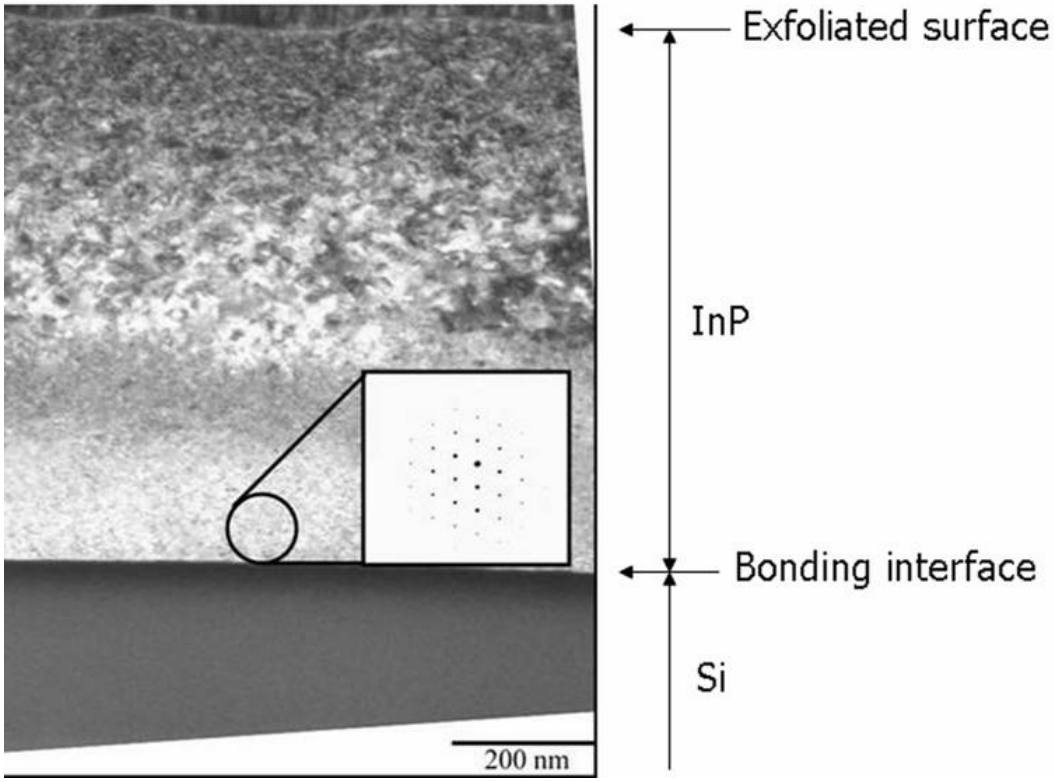

Fig. 5.12 Cross-sectional transmission electron microscope image of an InP/Si substrate fabricated using InP implanted with 115 keV He^{+} to a dose of 1.0x 10^{17} cm^{-2} showing the strain contrast caused by defects created during ion implantation and (inset) selected-area diffraction image indicating that the InP adjacent to the bonded interface (within ~200 nm) is crystalline.

Chapter 6 InGaAs solar cells grown on InP/SiO_2/Si bonded substrates

6-1. Introduction

In the previous chapter, we successfully fabricated alternative inexpensive InP/SiO_2/Si substrate structures for III-V semiconductor epitaxial growth. Now we are ready to fabricate III-V semiconductor compound solar cells on very inexpensive substrate, silicon, using that technology of InP layer transfer. In this study, we grew $In_{0.53}Ga_{0.49}As$ single-junction solar cells lattice matched to InP on the fabricated InP/SiO_2/Si alternative substrate structures prepared with wafer bonding and layer transfer.

Aim of this study

The aim of the study of this chapter is to demonstrate III-V solar cell growth on the prepared alternative inexpensive substrates of InP/SiO_2/Si and show the validity of the alternative substrate through characterization of the grown cells compared with reference cells grown on commercially available epi-ready InP bulk substrates.

6-2. Experimental

To test the performance of III-V compound active photovoltaic device layers grown on the wafer-bonded InP/Si substrates in functional solar cell structures, single-junction InGaAs solar cells were grown on both InP/Si substrates and commercial bulk epi-ready InP (001) substrates as a reference by metal-organic chemical vapor deposition

(MOCVD). Each of the solar cells had an n-type $In_{0.53}Ga_{0.47}As$ emitter and a p-type $In_{0.53}Ga_{0.47}As$ base with bandgap energy of 0.74 eV, nominally lattice-matched to (001) InP. Although we have not investigated the strain in these epitaxial InGaAs layers in detail yet, it is supposed that they are under tensile strain due to the difference in thermal expansion between InP and Si from the analysis with a similar heterostructure in Reference 1. The cells were designed to enable convenient and low-resistance contact to both base and emitter through the top surface of the cell. A schematic of the InGaAs cell structure is shown in Figure 6.1. The cell growth begins with a 1 μm thick InP buffer layer doped n-type with a target carrier concentration of 1 x 10^{19} cm^{-3} that functions as a current spreading layer for lateral back side contact. Back side and front side contacts were made using Ti/Au contacts on n-type InGaAs doped with a target carrier concentration of 1 x 10^{19} cm^{-3}. Typical optical micrographs of the front contact pads and grids of the InGaAs solar cells grown on the InP/Si substrates and on bulk InP (001) substrates are shown in Figure 6.2. An InGaAs tunnel-junction was used to switch the carrier type from the p-type in the base to n-type in the back side contact structure, allowing the front and back contacts to be fabricated with a single lithographic process. The remainder of the structure was typical of a single-junction InGaAs cell consisting of an InP window layer, a 300 nm thick n-type InGaAs emitter doped with a carrier concentration of 5 x 10^{18} cm^{-3}, a 3 μm thick p-type InGaAs base doped with a carrier concentration of 1 x 10^{17} cm^{-3}, and a 50 nm thick p-type InP back side field layer doped with a carrier concentration of 1-2 x 10^{18} cm^{-3}. No anti-reflective coating was used in the fabrication of the test cells. A typical image of the InGaAs solar cells grown on the InP/Si substrate is shown in Figure 6.3.

6-3. Results and discussion

Light current-voltage (I-V) characteristics of the InGaAs cells grown on the InP/Si substrates and on bulk InP (001) substrates were measured under AM1.5 Global illumination truncated at 850 nm by a long-pass filter, to mimic the optical configuration of subcells under a GaAs cell. The resulting I-V data are shown in Figure 6.4. The device parameters for the InGaAs cell grown on the wafer-bonded InP/Si substrate were J_{sc} = 24.9 mA cm^{-2}, V_{oc} = 0.30 V and FF = 0.66, where J_{sc}, V_{oc} and FF are short-circuit current, open-circuit voltage and fill factor, respectively. This performance was comparable to that of the InGaAs cells grown on bulk InP (001) substrates, J_{sc} = 21.5 mA cm^{-2}, V_{oc} = 0.31 V and FF = 0.70. Figure 6.5 shows the spectral responses for the InGaAs solar cells grown on the InP/Si substrate and a bulk InP substrate.

The larger J_{sc} and the higher quantum efficiency for the cell grown on the InP/Si substrate are attributed to enhanced light trapping effects in the wafer-bonded cell structure, due primarily to reflection at the bonding interfaces. Noting the large refractive index difference at the InP/SiO_2/Si bonding interface, $n_{InP} \sim 3.5$, $n_{SiO2} \sim 1.5$ and $n_{Si} \sim 3.5$ in the IR region, the reflectivity at the InP/SiO_2/Si interface was estimated as follows [2].

$$R_{tot} = \left| \frac{r_1 + r_2 e^{-2i\delta}}{1 + r_1 r_2 e^{-2i\delta}} \right|^2, \quad (1)$$

where

$$r_j = \frac{N_{j-1} - N_j}{N_{j-1} + N_j} \quad (2)$$

and

$$\delta = \frac{2\pi}{\lambda} n_1 d_1 . \quad (3)$$

The subscript j denotes the layer, where the InP, SiO_2 and Si layers correspond to j = 0, 1 and 2, respectively. Note that the refractive indices N_j are generally complex functions of wavelength and are expressed as $N_j = n_j + ik_j$, where both n_j and k_j are real. λ is the wavelength in vacuum and the thickness of the SiO_2 layer, d_1, was set to 420 nm as determined by ellipsometry measurement. For the optical constants of $In_{0.53}Ga_{0.47}As$, the data in Reference 3 was used with a modification of the imaginary part of the dielectric constant, ε_2, fit to the power law around at the absorption edge [4],

$$\varepsilon_2(\omega) \propto \frac{(\hbar\omega - E_g)^{1/2}}{(\hbar\omega)^2} . \quad (4)$$

The bandgap energy E_g of $In_{0.53}Ga_{0.47}As$ was set to be 0.73 eV. The optical constants of Si, SiO_2 and InP were adopted from Reference 5. The reflectivity at the $In_{0.53}Ga_{0.47}As$/InP interface was also estimated as a reference simply by determining $|r_1|$ from Equation 2, where the $In_{0.53}Ga_{0.47}As$ and InP layers correspond to j = 0 and 1, respectively. Based on this calculation the reflectivity of the InP/SiO_2/Si interface is estimated to be ~0.5 at maximum in the IR range for normal incidence due to the large refractive index differences at the InP/SiO_2 and SiO_2/Si interfaces, as shown in Figure 6.6. On the other hand, the reflectivity at the $In_{0.53}Ga_{0.47}As$/InP interface is negligibly small compared with that at the InP/SiO_2/Si bonding interface, as seen in Figure 6.6, due to the small difference in the refractive indices between $In_{0.53}Ga_{0.47}As$ and InP, $n_{In0.53Ga0.47As} \sim n_{InP} \sim$ 3.5 in the IR region. Particularly the reflectivity of the InP/SiO_2/Si interface significantly increases after 1200 nm, which well explains the enhanced photocurrent for the InGaAs

cell grown on the InP/Si substrate relative to that on a bulk InP substrate seen in the spectral responses of Figure 6.5.

Absorption in the $In_{0.53}Ga_{0.47}As$ layer was also calculated using a one-dimensional optical computational package [6]. This simulation was performed for a structure consisting of air/ $In_{0.53}Ga_{0.47}As$ (3650 nm)/ InP (1400 nm)/ SiO_2 (420 nm)/ Si for the cell on the InP/Si substrate and air/ $In_{0.53}Ga_{0.47}As$ (3650 nm)/ InP for the reference cell grown on a bulk InP substrate. The enhanced photocurrent and the oscillatory variation of the spectral quantum efficiency for the InGaAs cell on the InP/Si substrate were well-modeled by a simple one-dimensional optical calculation of the absorbance of the $In_{0.53}Ga_{0.47}As$ layer in the $In_{0.53}Ga_{0.47}As/InP/SiO_2/Si$ structure relative to the $In_{0.53}Ga_{0.47}As/InP$ reference structure, as shown in Figure 6.5.

Light trapping effects might also be enhanced by the slightly rougher top surface for cells grown on InP/Si substrates, attributable to the increased roughness of the InP/Si substrate growth surface (~10 nm-rms), relative to the bulk, epi-ready InP (001) substrates (<1 nm-rms) [7, 8]. This light I-V characteristic result indicates that the fabricated InP/Si substrates are promising alternative substrates to InP bulk wafers for InGaAs solar cell fabrication. The obtained J_{sc} of 24.9 mA cm^{-2} for the InGaAs cell on the InP/Si substrate is large enough to current match to state-of-art InGaP/GaAs two-junction cells [9, 10]. This InGaAs cell is therefore a strong candidate for the bottom cell of an ultrahigh efficiency three-junction cell with its significantly higher V_{oc} than the conventional Ge bottom cell [11-13].

6-4. Conclusions

We have demonstrated InGaAs solar cell fabrication on layer-transferred InP/Si substrates. Such InP/Si substrates could be used as substrates for InGaAsP/InGaAs dual-junction solar cells lattice-matched to InP as well as conventional InP single-junction cells. Ultimately, InP/Si substrates are extendable to fabrication of ultrahigh efficiency four-junction AlInGaP/GaAs/InGaAsP/InGaAs cells via a direct bond interconnect between subcell structures of InGaAsP/InGaAs grown on InP/Si and AlInGaP/GaAs grown on GaAs to form the overall four junction cell structure.

6-5. References

[1] A. Fontcuberta i Morral, J. M. Zahler, S. P. Ahrenkiel, M. W. Wanlass, and H. A. Atwater, *Appl. Phys. Lett.* **83**, 5413, 2003.

[2] O. S. Heavens, *Optical Properties of Thin Solid Films*, Butterworths Scientific Publications, London, 1955.

[3] M. A. Afromowitz, *Solid State Comm.* **15**, 59-63, 1974.

[4] S. Adachi, *J. Appl. Phys.* **66** (12), 6030-6040, 1989.

[5] E. D. Palik, ed., *Handbook of Optical Constants of Solids*, Academic Press, Orland, 1985.

[6] SpectraRay II, SENTECH Instruments GmbH, 2006.

[7] E. Yablonovitch and G. D. Cody, *IEEE Trans. Electron. Devices* **ED-29**, 300, 1982.

[8] J. H. Hu and R. G. Gordon, *Solar Cells* **30**, 437, 1991.

[9] T. Takamoto, E. Ikeda, H. Kurita, and M. Ohmori, *Appl. Phys. Lett.* **70**, 381, 1997.

[10] D. B. Jackrel, S. R. Bank, H. B. Yuen, M. A. Wistey, J. S. Harris, A. J. Ptak, S. W. Johnson, D. J. Friedman, S. R. Kurtz, *J. Appl. Phys.* **101**, 114916, 2007.

[11] D. J. Friedman and J. M. Olson, *Prog. Photovolt.* **9**, 179, 2001.

[12] J. M. Olson, D. J. Friedman, and S. R. Kurtz, in *Handbook of Photovoltaic Science and Engineering*, edited by A. Luque and S. Hegedus (Wiley, New York), p. 359, 2003.

[13] R. R. King, R. A. Sherif, G. S. Kinsey, S. R. Kurtz, C. M. Fetzer, K. M. Edmondson, D. C. Law, H. L. Cotal, D. D. Krut, J. H. Ermer, and N. H. Karam, *Proceedings of the International Conference on Solar Concentrators for the Generation of Electricity or Hydrogen* (NREL, Golden), 2005.

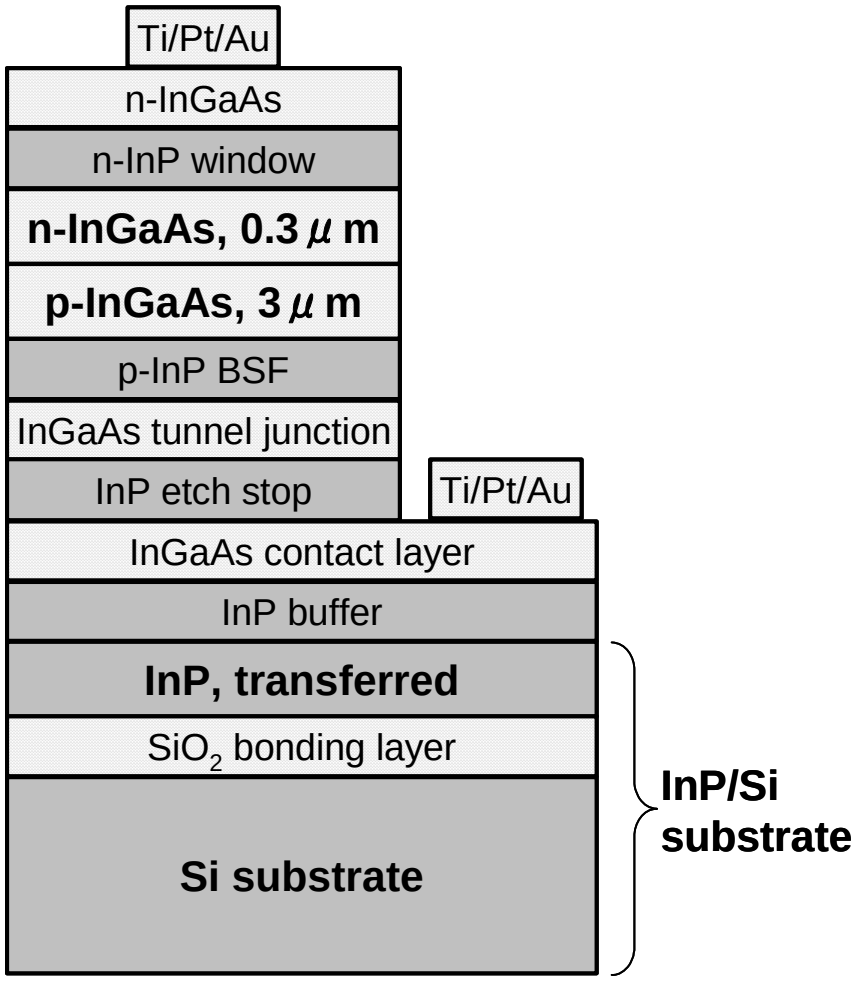

Fig. 6.1 Schematic cross-sectional view of the InGaAs solar cell grown on the InP/Si substrates.

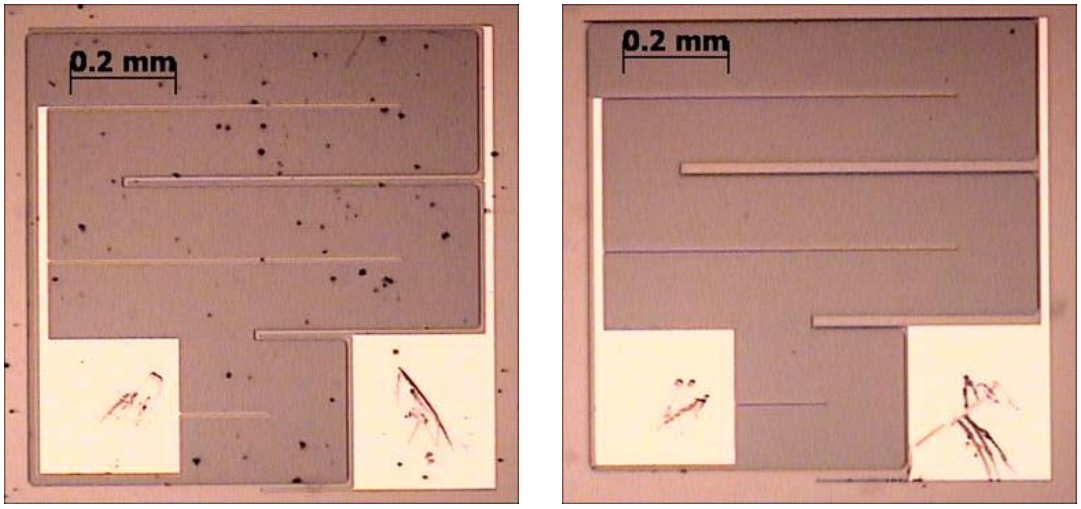

Fig. 6.2 Optical micrographs of the InGaAs cells, including contact pads and grids, fabricated on (left) an InP/Si substrate and (right) a bulk InP (001) substrate. The contact pad on the left is the n-side contact and the pad on the right is the p-side contact.

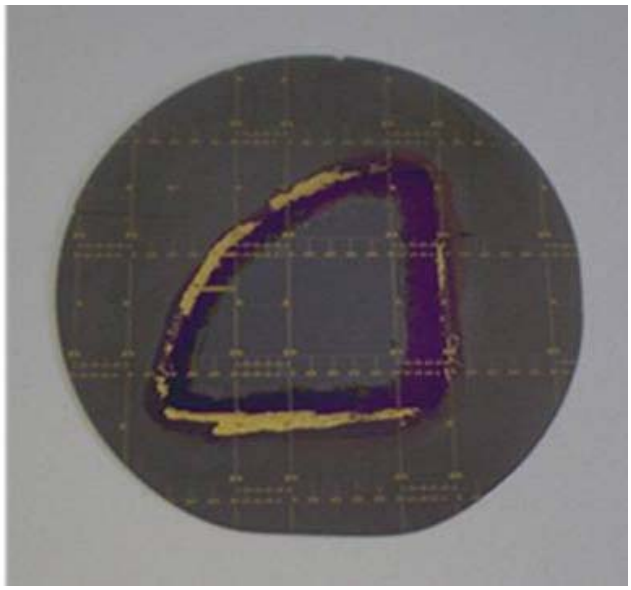

Fig. 6.3 Optical micrograph of the InGaAs solar cells grown on an InP/Si substrate.

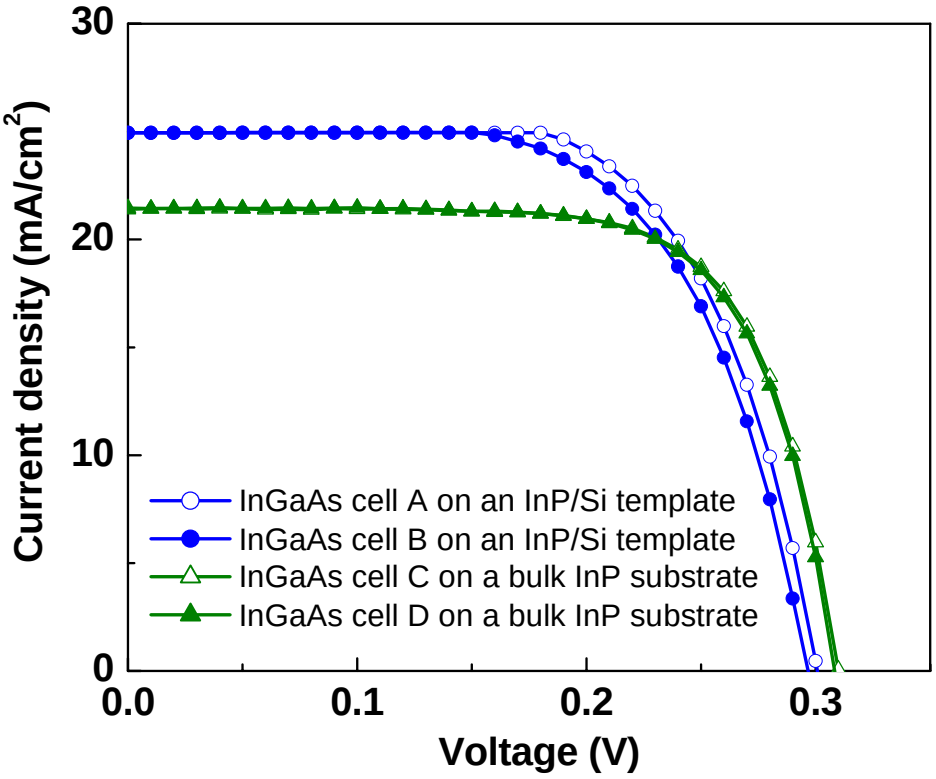

Fig. 6.4 Typical light I-V curves for the $In_{0.53}Ga_{0.47}As$ solar cells grown on an InP/Si substrate and on a commercial epi-ready InP substrate. The I-V measurements were performed under AM1.5G illumination truncated at 850 nm.

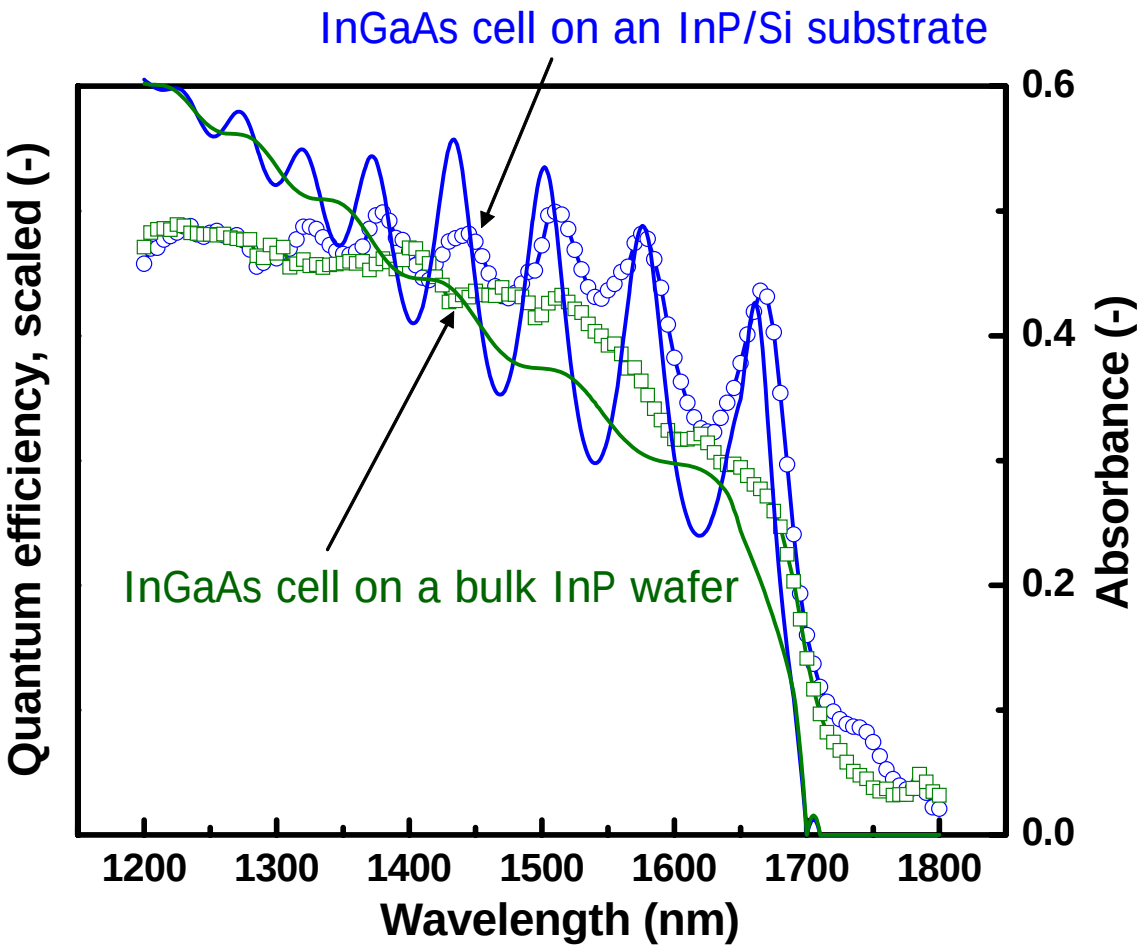

Fig. 6.5 Measured spectral responses for the $In_{0.53}Ga_{0.47}As$ solar cells grown on an InP/Si substrate and on a commercial epi-ready InP substrate. The calculated absorbance of the $In_{0.53}Ga_{0.47}As$ layer for $In_{0.53}Ga_{0.47}As/InP/SiO_2/Si$ (solid line) and $In_{0.53}Ga_{0.47}As/InP$ (dot line) structures are also plotted.

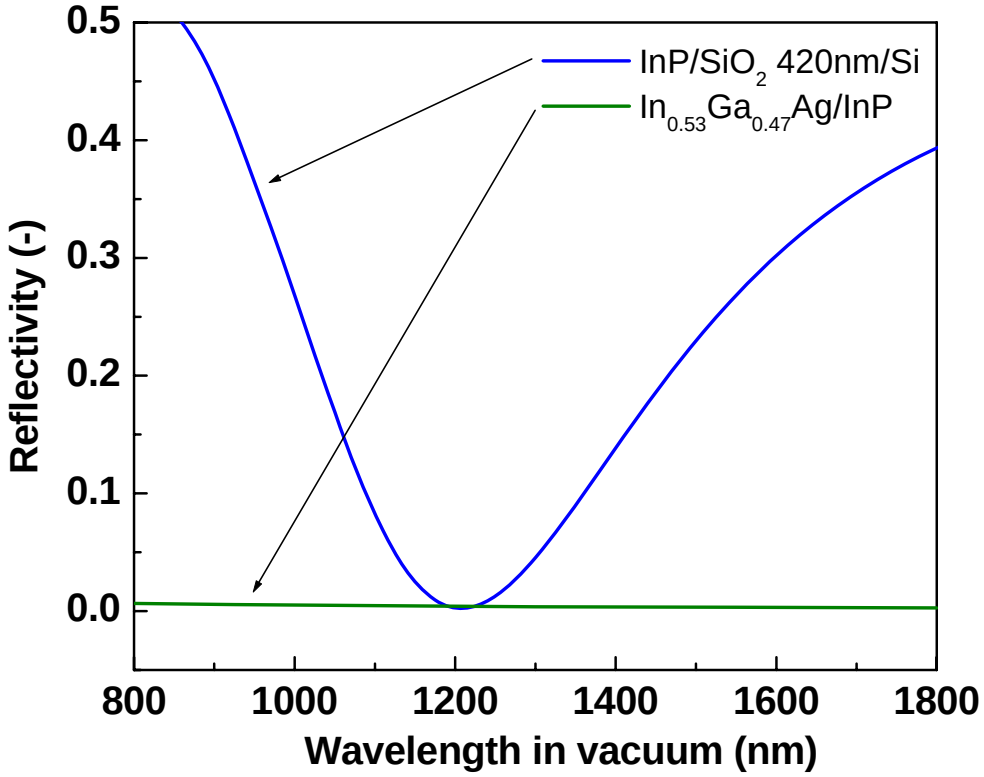

Fig. 6.6 Calculated reflectivities of the InP/SiO_2/Si and $In_{0.53}Ga_{0.47}As$/InP interfaces.

Chapter 7 Plasmonic GaAs Solar Cells

7-1. Introduction

7-1-1. Plasmonics for solar cell applications

Metal nanoparticles are known to exhibit distinctive optical characteristics, such as surface-enhanced Raman scattering (SERS) and second harmonic generation (SHG), relative to the bulk form of metals. [1-3] Representatives of the use of metal nanoparticles are biomolecular manipulation, labeling and detection with SERS. [4, 5] Other optoelectronic fields inspired by metal nanoparticles are also emerging, such as multiphoton absorption and fluorescence excitation for microscopy, microfabrication and optical data storage [6, 7].

These characteristics highly rely on the surface plasmon absorption, an enhanced absorption of light or electromagnetic fields by coupling between the incident photons and collective oscillation of free electrons at the metal surface. [8, 9] It was theoretically suggested that electromagnetic energy can be guided along periodic chain arrays of closely spaced metal nanoparticles that convert the optical mode into non-radiating surface plasmons. [10] Such plasmonic devices exploit light localization in the dipole-dipole coupling, or collective dipole plasmon oscillations of electrons, in neighboring nanoscale metal particles at the plasmon frequency. Plasmon waveguides consisting of closely spaced Ag nanoparticles with diameters around 30 nm have been experimentally observed to guide electromagnetic energy over distances of several hundred nanometers via near-field particle interactions. [11] Furthermore it has been suggested that light can

be routed efficiently around sharp corners of nanoparticle chain arrays. [12] Such plasmon waveguide technologies can potentially be utilized for construction of all-optical nanoscale network. [13-15]

Solar cell structures have been suffering from such a trade-off on the thickness of the active photovoltaic layers as follows. Thinner photovoltaic layers will have less light absorption while thicker layers will have more bulk carrier recombination, as schematically depicted in Figure 7.1. Both of these two factors would be losses for the solar cell electrical output converted from the incident sunlight energy. Therefore the thickness of the active photovoltaic layer is usually optimized to maximize the energy conversion efficiency through that trade-off.

Metallic nanostructures can excite surface plasmons and can dramatically increase the optical path length in thin active photovoltaic layers to enhance overall photoabsorption, as described in the following sections. This effect has potential for cost and weight reduction with thinned layers and also for efficiency enhancement associated with increased carrier excitation level in the absorber layer.

In this study, we have investigated two types of "plasmonic" solar cells described as follows.

7-1-2. Plasmonic solar cells with metal nanoparticles

Metal nanoparticles placed on solar cell surfaces can act as “antennas” to collect the incident light with their large extinction cross section near the surface plasmon resonance and then scatter the incident light into a wide range of angles to increase the optical path length in the absorber layer. This effect has potential for cell cost and weight reduction resulting from use of thinner absorber layers and also for efficiency enhancement associated with increased carrier excitation level. Several research groups have observed photocurrent enhancement for Si cells by this scheme. [16-22] Applications of such plasmonic metal nanoparticles to other types of solar cells such as dye-sensitized solar cells and organic solar cells have been also reported. [23-25] No such study however has been done, to the best of our knowledge, for III-V semiconductor compound solar cells even though the very same trade-off between the absorption length and the carrier diffusion length exists also in III-V cells. In this study we specifically investigate the effect of arrays of subwavelength-size metal particles on GaAs solar cell absorption and photocurrent.

7-1-3. Plasmonic solar cells with metallic back structures

By placing a metallic layer at the bottom of a photovoltaic layer as schematically depicted in Figure 7.2, incident light can couple into surface plasmons propagating at the semiconductor/metal interface via some subwavelength-size feature such as nanoscale grooves. [15, 26-28] In this way, we can convert the direction of energy flux from normal to lateral direction relative to the photovoltaic layer. This is a novel concept to utilize such surface plasmon propagation for solar cell applications to harvest more energy from the sun in thin photovoltaic active layers. [29]

Some types of conventional solar cells such as silicon solar cells also have metallic back reflectors to increase optical path, while III-V semiconductor compound solar cells such as GaAs cells have thin photovoltaic active layers on top of thick substrate. However, the plasmon-induced absorption enhancement by metallic back structures observed in this study would occur significantly only for strongly absorbing or direct bandgap semiconductors accounting for the energy dissipation in metals. We calculated energy dissipation fraction of coupled surface plasmon polaritons propagating at material interfaces into metals and semiconductors as follows. Electrical energy dissipation (energy per volume per time) is written as;

$$P(x,z) = \frac{1}{2}\omega\varepsilon''\varepsilon_0\left|\vec{E}(x,z)\right|^2, \quad \text{(Eq. 1)}$$

where ω is frequency of the field, ε'' is imaginary part of relative permittivity or dielectric function of the medium considered, ε_0 is permittivity of vacuum, and $E(x, z)$ is the electric field. [30] The x-axis and z-axis were taken to be parallel and normal to the plane of the metal/semiconductor interface, respectively, as schematically shown in Figure 7.3. In this calculation, I considered semi-infinite thick semiconductor and metal layers for simplicity. The electric field components are written as follows, with the subscripts *1* for metal and *2* for dielectric.

$$E_{x,j} = E_0 \exp\left\{i\left(k_x x - k_{z,j}|z| - \omega t\right)\right\} \quad \text{(Eq. 2)}$$

$$E_{z,1} = -\frac{k_x}{k_{z,1}} E_0 \exp\{i(k_x x - k_{z,1}|z| - \omega t)\} \quad \text{(Eq. 3)}$$

$$E_{z,2} = \frac{k_x}{k_{z,2}} E_0 \exp\{i(k_x x - k_{z,2}|z| - \omega t)\} \quad \text{(Eq. 4)}$$

$(j = 1,2)$

Since *E (x, j)* and *E (z, j)* are in phase,

$$\left|\vec{E}_j\right|^2 = \left|E_{x,j}\right|^2 + \left|E_{z,j}\right|^2. \quad \text{(Eq. 5)}$$

Decomposing the complex wavenumbers *k* into their real and imaginary parts,

$$\begin{aligned} E_{x,j} &= E_0 \exp\{i(k_x x - k_{z,j}|z| - \omega t)\} \\ &= E_0 \exp(-k_x'' x)\exp(-k_{z,j}''|z|)\exp\{i(k_x' x - k_{z,j}'|z| - \omega t)\}, \end{aligned} \quad \text{(Eq. 6)}$$

$$\begin{aligned} E_{z,1} &= -\frac{k_x}{k_{z,1}} E_0 \exp\{i(k_x x - k_{z,1}|z| - \omega t)\} \\ &= -\frac{k_x}{k_{z,1}} E_0 \exp(-k_x'' x)\exp(-k_{z,1}''|z|)\exp\{i(k_x' x - k_{z,1}'|z| - \omega t)\} \end{aligned}, \quad \text{(Eq. 7)}$$

$$\begin{aligned} E_{z,2} &= \frac{k_x}{k_{z,2}} E_0 \exp\{i(k_x x - k_{z,2}|z| - \omega t)\} \\ &= \frac{k_x}{k_{z,2}} E_0 \exp(-k_x'' x)\exp(-k_{z,2}''|z|)\exp\{i(k_x' x - k_{z,2}'|z| - \omega t)\} \end{aligned}. \quad \text{(Eq. 8)}$$

From Equations 5-8,

$$\left|\vec{E}_1\right|^2 = \left|E_{x,1}\right|^2 + \left|E_{z,1}\right|^2 = \left(1 + \left|\frac{k_x}{k_{z,1}}\right|^2\right) {E_0}^2 \exp\left(-2k_x'' x\right)\exp\left(-2k_{z,1}''\left|z\right|\right), \quad \text{(Eq. 9)}$$

$$\left|\vec{E}_2\right|^2 = \left|E_{x,2}\right|^2 + \left|E_{z,2}\right|^2 = \left(1 + \left|\frac{k_x}{k_{z,2}}\right|^2\right) {E_0}^2 \exp\left(-2k_x'' x\right)\exp\left(-2k_{z,2}''\left|z\right|\right). \quad \text{(Eq. 10)}$$

The energy dissipation at the interface (energy per area per time) for each side of material is therefore written as;

$$\begin{aligned} P_j(x) &= \int_0^\infty \frac{1}{2}\omega\varepsilon_j''\varepsilon_0\left|\vec{E}_j(x,z)\right|^2 dz \\ &= \frac{1}{2}\omega\varepsilon_j''\varepsilon_0\left(1 + \left|\frac{k_x}{k_{z,j}}\right|^2\right) {E_0}^2 \exp\left(-2k_x'' x\right)\int_0^\infty \exp\left(-2k_{z,j}'' z\right)dz \end{aligned} \quad \text{(Eq. 11)}$$

Then energy dissipation fraction for the dielectric or semiconductor material is;

$$\frac{P_2}{P_1 + P_2} = \frac{\varepsilon_2''\left(1 + \left|\frac{k_x}{k_{z,2}}\right|^2\right)\int_0^\infty \exp\left(-2k_{z,2}'' z\right)dz}{\varepsilon_1''\left(1 + \left|\frac{k_x}{k_{z,1}}\right|^2\right)\int_0^\infty \exp\left(-2k_{z,1}'' z\right)dz + \varepsilon_2''\left(1 + \left|\frac{k_x}{k_{z,2}}\right|^2\right)\int_0^\infty \exp\left(-2k_{z,2}'' z\right)dz}. \quad \text{(Eq. 12)}$$

This energy dissipation fraction is simplified by using

$$\left|\frac{k_x}{k_{z,1}}\right|^2 = \left|\frac{\varepsilon_2}{\varepsilon_1}\right| \quad \text{(Eq. 13)}$$

and

$$\left|\frac{k_x}{k_{z,2}}\right|^2 = \left|\frac{\varepsilon_1}{\varepsilon_2}\right|, \quad \text{(Eq. 14)}$$

which are derived from

$$k_x = \frac{\omega}{c}\left(\frac{\varepsilon_1\varepsilon_2}{\varepsilon_1+\varepsilon_2}\right)^{1/2} \quad \text{(Eq. 15)}$$

and

$$k_{z,j}{}^2 + k_x{}^2 = \varepsilon_j\left(\frac{\omega}{c}\right)^2. \quad \text{(Eq. 16) [31]}$$

The semi-infinite integrals in Equation 12 are conducted as;

$$\int_0^\infty \exp\left(-2k_{z,j}{}'' z\right)dz = \frac{1}{2k_{z,j}{}''}. \quad \text{(Eq. 17)}$$

From Equations 13, 14 and 17, Equation 12 is simplified into;

$$\frac{P_2}{P_1+P_2}=\frac{\frac{\varepsilon_2''}{2k_{z,2}''}\left(1+\left|\frac{\varepsilon_1}{\varepsilon_2}\right|\right)}{\frac{\varepsilon_1''}{2k_{z,1}''}\left(1+\left|\frac{\varepsilon_2}{\varepsilon_1}\right|\right)+\frac{\varepsilon_2''}{2k_{z,2}''}\left(1+\left|\frac{\varepsilon_1}{\varepsilon_2}\right|\right)}. \quad \text{(Eq. 18)}$$

Using this formalism, the energy dissipation fraction in the semiconductor layer from the surface plasmons propagating at the semiconductor/metal interface was calculated for several combinations of semiconductors and metals, as shown in Figure 7.4. The wavelength dependent data of the dielectric functions of metals and semiconductors of Palik was used for this calculation. [32] It is found from this result that most energy is absorbed by GaAs rather than metals for the visible optical wavelength range, which solar cell applications concerns, particularly for the cases with Ag and Al. This means GaAs can effectively harvest the energy extracted from the coupled surface plasmons beating the Ohmic loss in metals with its strong absorption or large imaginary part of dielectric function. On the other hand, silicon, which is a weak absorber, has much lower energy absorption fraction suffering from Ohmic loss in metals. This is a great benefit for direct bandgap semiconductor materials, which are stronger absorbers, for such types of "plasmonic" solar cell applications.

7-2. Plasmonic GaAs solar cells with metal nanoparticle arrays

7-2-1. Experimental

Optically thin GaAs solar cells

To demonstrate absorption enhancement by metal nanoparticle scattering, 'optically thin' GaAs solar cells (i.e., absorber layer thickness << absorption length) with a 50nm-

thick p-type emitter on top of a 150nm-thick n-type base were grown by metalorganic chemical vapor deposition. Dense arrays of metal nanoparticles were then deposited onto the $Al_{0.8}Ga_{0.2}As$ window layer of the GaAs cells through porous alumina membranes by thermal evaporation. A schematic of the optically thin GaAs cell structure is shown in Figure 7.5. This cell structure consisted of a 50nm-thick p-type emitter on top of a 150nm-thick n-type base epitaxially grown on a (001) n-type GaAs substrate by metalorganic chemical vapor deposition (MOCVD). The remainder of the structure was typical of a single-junction GaAs solar cell consisting of a 30 nm thick p-type $Al_{0.8}Ga_{0.2}As$ window layer and a 500 nm thick n-type $Al_{0.8}Ga_{0.2}As$ back side field (BSF) layer. Front and back side electrical contacts were made using 150 nm thick Au contacts formed by thermal evaporation with a standard optical lithography for the front contact. No anti-reflective coating was used in the fabrication of the cell structure.

Metal nanoparticle arrays

Dense arrays of metal nanoparticles were deposited onto the window layers for both types of the GaAs solar cells through porous alumina (Al_2O_3) membranes by thermal evaporation. The electrochemical fabrication of the porous membranes [33, 34] and metal nanoparticle deposition were conducted by Keisuke Nakayama of Caltech. Details of the porous alumina membrane preparation and characterization are described somewhere else. [35] The Ag particle diameter ranged from 60-150 nm, and interpartice spacing ranged from 100-300 nm, with particle shape in the form of upright circular cylinders. The Ag nanoparticle dimensions were quite uniform across each cell sample due to the uniformity of the pore size and spacing in the alumina membranes, for which pore diameters were

carefully controlled during the membrane preparation. The height of the metal nanoparticles was controlled simply with the deposition thickness in the thermal evaporation process. Figure 7.6 shows scanning electron microscope (SEM) images of the Ag nanoparticle arrays with a diameter of 60 nm and heights ranging through 10 nm to 75 nm deposited on the GaAs solar cells.

In this way, we obtained quite uniform, dense arrays of metal nanoparticles. We can control the particle diameter and spacing by the fabrication conditions of the porous membranes, and particle height simply by deposition thickness. All previously reported studies for solar cells with metal nanoparticles [16-25] simply used thermal annealing after evaporation of thin metal films to form metal nanoparticles through thermal aggregation. Relative to this method, the advantages of our metal nanoparticle fabrication scheme are represented by the excellent uniformity and controllability for the particle shape and size and no need for post annealing.

Characterization of the metal nanoparticles and the cells

Spectral response measurements for the fabricated “optically-thin” GaAs solar cells with and without metal nanoparticles of Ag and Al were taken to determine the effect of metal nanoparticles. Transmission measurements for the Ag and Al nanoparticles were obtained from samples deposited on glass slides whose dimensions were similar to those used for the cell measurements.

7-2-2. Optical model

To understand the role of the metal nanoparticles on the GaAs solar cells thoroughly, a simple optical model to represent the absorption enhancement in the photovoltaic layers with metal nanoparticles on top has been developed. As an overview, we calculated the absorbance in the GaAs cells considering scattering and absorption by the metal particles, accounting the particles' surface coverage, reflectivity at the air/GaAs interface, angular dependence of scattered light, extinction efficiency factor, which is extinction cross-section of the particles normalized by the geometrical cross-section (means how large the incident light feels for the particles), and radiation efficiency, which represents how much light interacting with the particles is scattered rather than being absorbed. We calculated these factors for oblate spheroid particles in the quasistatic limit using an effective medium approximation accounting for the influence of both air and GaAs. The calculation details follow.

For simplification, we considered only GaAs photovoltaic layer neglecting the AlGaAs window layer. (Note that the refractive indices of GaAs and AlGaAs are similar.)

Absorption fraction of the incident light in a GaAs layer with a thickness of L is simply;

$$A_0(\lambda) = 1 - \exp(-\alpha(\lambda)L), \quad \text{(Eq. 19)}$$

where α is the absorption constant of GaAs and λ is the wavelength in vacuo. The angular distribution of the light intensity scattered by sub-wavelength sized particles in the quasistatic limit is known to be;

$$I_{sca} \propto \left(1+\cos^2\theta\right) I_0 , \quad \text{(Eq. 20)}$$

where the angle θ is measured from the forward to the scattered directions. [36] The absorption fraction for the scattered light is;

$$A_\theta(\lambda) = \int_0^{\pi/2} \frac{1+\cos^2\theta}{\int_0^{\pi}\left(1+\cos^2\theta\right)d\theta} \left\{1-\exp\left(-\alpha(\lambda)\frac{L}{\cos\theta}\right)\right\} d\theta , \quad \text{(Eq. 21)}$$

accounting that the optical path in the GaAs layer is increased from L into $L/cos\theta$. Total absorption fraction for the GaAs layer with nanoparticles on top with a surface coverage ξ is;

$$A_{tot}(\lambda) = \xi Q_{ext}(\lambda)\eta_{rad}(\lambda)A_\theta(\lambda) + \left(1-\xi Q_{ext}(\lambda)\right)\left(1-R(\lambda)\right)A_0(\lambda) \ (\xi Q_{ext} < 1), \quad \text{(Eq. 22)}$$

where Q_{ext} and η_{rad} are the extinction efficiency factor (extinction cross section divided by geometrical cross section) and the radiation efficiency (scattering cross section divided by extinction cross section) for the nanoparticles as defined in References 17 and 36, respectively. ξ was 0.4 and 0.3 for the 60nm- and 150nm-diameter cases, respectively, as determined from SEM images. Q_{ext} and η_{rad} were calculated for oblate ellipsoidal metal particles with a minor axis parallel to the incident light corresponding to the height of the experimental nanoparticles in the quasistatic limit using an effective medium approximation for the complex dielectric function of the surrounding medium as

$\varepsilon_{medium}(\lambda) = \frac{2\varepsilon_{air}(\lambda) + \varepsilon_{GaAs}(\lambda)}{3}$. [36] The wavelength-dependent complex dielectric functions of metals and GaAs were obtained from Reference 32. Particularly for Al nanoparticles, Q_{ext} and η_{rad} were calculated for concentric Al-Al_2O_3 core-shell ellipsoidal particles with an Al_2O_3 shell thickness of 4 nm accounting for surface oxidation of Al particles in the atmosphere. [37, 38] The reflectivity R at the air/GaAs interface is also accounted as follows since our GaAs solar cells had no anti-reflective coating or surface structure. Assuming normal incidence of light into a GaAs layer, the wavelength-dependent reflectivity is written as;

$$R(\lambda) \equiv \frac{I_r(\lambda)}{I_0(\lambda)} = \left| \frac{N_2(\lambda) - N_1(\lambda)}{N_2(\lambda) + N_1(\lambda)} \right|^2, \quad \text{(Eq. 23)}$$

where N is the complex refractive index of air or GaAs. Then we took the ratio of the absorbance of Equation 22 to the absorbance without particle to compare with the normalized photocurrent data.

7-2-3. Results and Discussion

Figure 7.7 shows the photocurrent spectra for the GaAs solar cells with metal nanoparticles of Ag and Al on top. This photocurrent data is normalized by the spectral response of the reference GaAs cell without metal nanoparticles. The maximum photocurrent enhancement of 260% is seen around at 900 nm for the GaAs cell with Ag nanoparticles with a diameter of 150 nm, a height of 20 nm and 30% surface coverage. The normalized photocurrent (J/J_0) is seen to be significantly higher for the cells with

150nm-diameter nanoparticles relative to those with a 60nm-diameter for almost entire spectral range, which can be attributed to the considerably higher radiation efficiency, the ratio of the scattering cross-section to the extinction cross-section, for larger metal nanoparticles as discussed in a following section.

The transmission spectra for the Ag nanoparticle arrays with a particle diameter of 60 nm and various particle heights deposited on glass slides is shown in Figure 7.8. Surface plasmon resonance in the metal nanoparticles is seen as the dips around at 400-500 nm, while no notable scattering is observed for near-IR region. In Figure 7.7, a dip presumably due to plasmon resonance for the cell with 60nm-diameter Ag particles is seen around at 600 nm, whose discrepancy from the transmission spectra is attributed to the effect of different substrates where GaAs has higher refractive index than glass to redshift the resonant frequency. The dip around at 350 nm for Ag nanoparticle arrays is due to absorption by interband transitions in Ag.

The computed normalized absorption spectra for GaAs solar cells with metal nanoparticles are superposed to the experimental normalized photocurrent for the corresponding cells in Figure 7.7. This model calculation well reproduces the experimental results qualitatively, including the peaks around at 300 nm and 900 nm and the dips around at 600 nm for 60nm-diameter Ag and 350 nm for 60nm-diameter Al. The dip around at 600 nm in the normalized photocurrent for the cell with 60nm-diameter Ag particles, presumably due to the surface plasmon resonance in the Ag particles, is not seen for 150nm-diameter. This experimental result is attributed to the significantly higher

η_{rad} (~0.9) for the 150nm-diameter case than that (~0.6) for the 60nm-diameter case suppressing the absorption loss in the Ag nanoparticles, as shown in Figure 7.9. For both of Ag and Al, higher photocurrent enhancement at 900 nm for 150nm-diameter cases than for 60nm-diameter cases is reproduced in the modeling, caused mainly by the higher Q_{ext} for the larger metal nanoparticles. It is important to note that both Ag and Al particle cells suffer from the loss back scattering from metal nanoparticles into the air as seen in Equation 20.

Based on these investigations, we have obtained enhancements in net photocurrent, not only for longer wavelength range, and efficiency for certain optimized conditions, as shown in Figure 7.10.

7-3. Plasmonic GaAs solar cells with metallic back structures

7-3-1. Experimental

Fabrication of the waveguide-like GaAs solar cell structure with a metal back layer, schematically shown in Figure 7.11 (a), started with an "inversely grown" GaAs cell shown in Figure 7.11 (b). This cell structure consisted of a 50nm-thick n-type base on top of a 50nm-thick p-type emitter epitaxially grown on a (001) p-type GaAs substrate by MOCVD. The remainder of the structure was typical of a single-junction GaAs solar cell consisting of a 30 nm thick p-type $In_{0.49}Ga_{0.51}P$ window layer and a 30 nm thick n-type $In_{0.49}Ga_{0.51}P$ BSF layer. This heavily doped $In_{0.49}Ga_{0.51}P$ BSF layer acts also as the electrical contact layer to the Ag back reflector layer.

A 500 nm thick Ag bonding layer was deposited by thermal evaporation on the $In_{0.49}Ga_{0.51}P$ BSF layer after removing the 3 um thick GaAs layer from the inversely grown GaAs cell structure in Figure 7.11 (b) using selective chemical etching with citric acid (50% weight aqueous solution) - H_2O_2 solution (4:1 vol.) at room temperature (~10 min). This cell structure with an Ag layer was then bonded to an Ag/Cr/Si supporting substrate consisting of a heavily doped p-type Si (001) substrate with a 5 nm thick Cr adhesion layer and a 500 nm thick Ag bonding layer deposited by sequent thermal evaporation. This wafer bonding technique is based on our investigation presented in References 39 and 40 and conducted under ~0.5 MPa uniaxial pressure at 200 C^o for 10 hours. Then the GaAs substrate was removed by selective chemical etching with H_3PO_4 - H_2O_2 (3:7 vol.) at 50 C^o for ~1 hour followed by H_3PO_4 - H_2O_2 - H_2O (1:4:5 vol.) at room temperature for ~1 hour. The solution compositions were chosen to maximize the etching rate of GaAs for the 3:7 solution and the etching selectivity between GaAs and InGaP for the 1:4:5 solution. [41, 42] The InGaP etch stop layer was then removed by HCl (conc.) at room temperature for ~1 min. Front and back side electrical contacts were made using 150 nm thick Au contacts formed by thermal evaporation with a standard optical lithography for the front contact. No anti-reflective coating was used in the fabrication of the cell structure.

A reference cell structure, shown in Figure 7.11 (c), is also prepared without removal of the 3 um thick GaAs layer, which mimics an absorbing substrate. For this reference cell structure, 500 nm thick Ag was deposited on the 3 μm thick GaAs layer and then bonded to the Ag/Cr/Si substrate followed by similar cell processes as the waveguide-like cell.

Figure 7.12 shows a cross-sectional SEM image for the fabricated waveguide-like GaAs solar cell with an Ag back layer. Figure 7.13 shows photographs of the waveguide-like GaAs solar cell with an Ag back layer and the reference cell with a 3 μm GaAs absorbing layer. The waveguide-like cell surface looks reddish to our eyes presumably due to back reflection of incident light unabsorbed in the GaAs cell by the Ag layer, while the reference cell surface is dark gray, typical for optically-thick GaAs solar cells.

Figure 7.14 shows AFM and SEM images of the surface of the InGaP BSF layer after removal of the 3 μm thick GaAs layer, which represents the roughness at the GaAs cell / Ag interface. This semiconductor/metal interface had a subwavelength-size roughness, with a peak-valley amplitude around 20 nm, so we expect coupling of the incident light into surface plasmon mode or photonic waveguide mode by multiple angle scattering to enhance absorption.

7-3-2. Results and Discussion

Figure 7.15 shows the typical light I-V curves for the waveguide-like GaAs cells with Ag back structure and the reference GaAs cells under AM1.5 Global solar spectrum with 1-sun total intensity (100 mW cm^{-2}). The short circuit current is significantly larger for the cells with Ag back structure. Incidentally, the open-circuit voltage varied due to random shunting, because we have not optimized the process conditions yet, but it does not affect short-circuit current much. Figure 7.16 shows the normalized photocurrent spectrum, which is the photocurrent of the waveguide-like cell divided by the

photocurrent of the reference cell. These light I-V and spectral response results show that the waveguide-like GaAs cell obtained overall photocurrent enhancement for entire wavelengths. A large peak around at 900 nm, the GaAs bandedge, seen in Figure 7.16 is presumably due to multiple-angle reflection at the Ag back layer. Figure 7.16 also shows another peak at 600 nm. Figure 7.17 shows the calculated dispersion relation at the GaAs/Ag interface and surface plasmon resonance is found at 600 nm, represented by the maximum of the wavevector parallel to the interface. One possible cause of this 600 nm peak is therefore surface plasmon resonance at the GaAs/Ag interface leading to absorption enhancement through incoupling of the incident light into propagating surface plasmon polaritons as described in Section 7-1-3. However, as we also calculated the absorption enhancement by Fabry-Perot effect in the thin active GaAs layer with reflecting back surface, a peak for the normalized absorbance is also found around at 600 nm, as seen in Figure 7.18. Due to this coincidence, we cannot determine which effect caused this 600 nm peak for the photocurrent enhancement for now. This question would be figured out by switching the metal from Ag into Al to shift plasmon resonance, or changing cell thickness to shift the Fabry-Perot peak for example.

Significantly, the waveguide structure solar cells presented in this chapter consist of III-V semiconductor compound materials as thin as a couple of hundreds nanometers, which indicates a possibility of significant production cost reduction relative to conventional III-V solar cells. Although the GaAs substrates were wasted by the etch back process after wafer bonding in this work, the layer transfer technologies developed in Chapters 5 and 6 could be employed to reuse a single GaAs substrate repeatedly.

7-4. Conclusions

In this chapter two types of "plasmonic" GaAs solar cell were investigated. Firstly, absorption enhancement by metal nanoparticle scattering in 'optically thin' GaAs solar cells was shown. Dense arrays of metal nanoparticles were deposited directly onto the $Al_{0.8}Ga_{0.2}As$ window layer of the GaAs cells through porous alumina membranes by thermal evaporation. Spectral response measurements revealed photocurrent enhancements up to 260% at 900 nm for a GaAs cell with Ag nanoparticles with 150 nm diameter, 20 nm height and 30% surface coverage, relative to reference GaAs cells with no metal nanoparticle array. This photocurrent enhancement and the spectral behavior of the normalized photocurrent are qualitatively reproduced by a simple optical model representing surface plasmon resonance of metal nanoparticles and multi-angle scattering. Particularly, larger subwavelength-size metal particles resulted in larger photocurrent due to higher radiation efficiencies both for Ag and Al. Secondly, waveguide-like GaAs solar cells with metallic back structures were introduced. Ultrathin GaAs cells with Ag back layers were fabricated through wafer bonding and layer transfer with selective etch back of the GaAs substrates. This waveguide-like GaAs cell showed net photocurrent enhancement throughout the solar spectral range relative to the reference GaAs cell with an absorbing GaAs back layer. A large peak for the normalized photocurrent around at the GaAs bandedge was found and attributed to multiple-angle reflection at the Ag back layer. A smaller peak was found at 600 nm and is due either to surface plasmon coupling or Fabry-Perot resonance effect.

7-5. References

[1] C. K. Chen et al, *Phys. Rev. Lett.* **46**, 145, 1981.

[2] A. Wokaun et al, *Phys. Rev. B* **24**, 849, 1981.

[3] F. J. Garcia-Vidal and J. B. Pendry, *Phys. Rev. Lett.* **77**, 1163, 1996.

[4] Y. W. C. Cao et al, *Science* **297**, 1536, 2002.

[5] W. Fritzsche and T. A. Taton, *Nanotechnology* **14**, R63, 2003.

[6] W. Wenseleers et al, *J. Phys. Chem. B* **106**, 6853, 2002.

[7] X. Yin et al, *Appl. Phys. Lett.* **81**, 3663, 2002.

[8] S. A. Maier and H. A. Atwater, *J. Appl. Phys.* **98**, 011101, 2005.

[9] H. A. Atwater, *Sci. Am.*, p. 56, April, 2007.

[10] M. Quinten et al, *Opt. Lett.* **23**, 1331, 1998.

[11] S. A. Maier et al, *Nat. Mater.* **2**, 229, 2003.

[12] S. A. Maier et al, *Mater. Sci. Eng. C* **19**, 291, 2002.

[13] W. L. Barnes et al, *Nature* **424**, 824, 2003.

[14] L. Dobrzynski et al, *Phys. Rev. E* **69**, 035601, 2004.

[15] D. Pacifici et al, *Nat. Photo.* **1**, 402, 2007.

[16] H. R. Stuart and D. G. Hall, *Appl. Phys. Lett.* **69**, 2327, 1996.

[17] H. R. Stuart and D. G. Hall, *Appl. Phys. Lett.* **73**, 3815, 1998.

[18] D. M. Schaadt et al, *Appl. Phys. Lett.* **86**, 063106, 2005.

[19] S. Pillai et al, *Appl. Phys. Lett.* **88**, 161102, 2006.

[20] D. Derkacs et al, *Appl. Phys. Lett.* **89**, 093103, 2006.

[21] K. R. Catchpole and S. Pillai, *J. Appl. Phys.* **100**, 044504, 2006.

[22] S. Pillai et al, *J. Appl. Phys.* **101**, 093105, 2007.

[23] M. Ihara et al, *J. Phys. Chem. B* **101**, 5153, 1997.

[24] C. Wen et al, *Sol. Ener. Mat. Sol. Cell.* **61**, 339, 2000.

[25] B. P. Rand et al, *J. Appl. Phys.* **96**, 7519, 2004.

[26] H. J. Lezec and T. Thio, Opt. Exp. 12, 3629, 2004.

[27] G. Gay et al, *Nat. Phys.* **2**, 262, 2006.

[28] L. Chen et al, Opt. Exp. 14, 12629, 2006.

[29] V. E. Ferry et al, *MRS Spring Meeting*, San Francisco, L3.2, Mar. 2008.

[30] A. D. Yaghjian, *IEEE Trans. Ant. Prop.* **55**, 1495, 2007.

[31] H. Raether, *Surface Plasmons on Smooth and Rough Surfaces and on Gratings*, Springer-Verlag, 1986.

[32] E. D. Palik, ed., *Handbook of Optical Constants of Solids* (Academic Press, Orland), 1985.

[33] H. Masuda and M. Satoh, Jpn. J. Appl. Phys. 35, L126-L129, 1996

[34] H. Masuda et al, Adv. Mater. 12 (14), 1031-1033, 2000

[35] K. Nakayama, K. Tanabe and H. A. Atwater, in preparation.

[36] C. F. Bohren and D. R. Huffman, *Absorption and Scattering of Light by Small Particles* (Wiley, New York), 1983, Chap. 3 and 5.

[37] L. P. H. Jeurgens et al, *Appl. Surf. Sci.* **144-145**, 1999, pp. 11-15.

[38] W. Zhu et al, *Appl. Phys. Lett.* **78**, 2001, pp. 3103-3105.

[39] K. Tanabe et al, *Appl. Phys. Lett.* **89**, 2006, pp. 102106-1-102106-3

[40] K. A. Diest, M. J. Archer, J. A. Dionne, Y. Park, M. J. Czubakowski and H. A. Atwater, submitted.

[41] Y. Mori and N. Watanabe, *J. Electrochem. Soc.* **125**, 1510-1514, 1978.

[42] Y. C. Hsieh et al, *J. Cryst. Growth* **289**, 96-101, 2006.

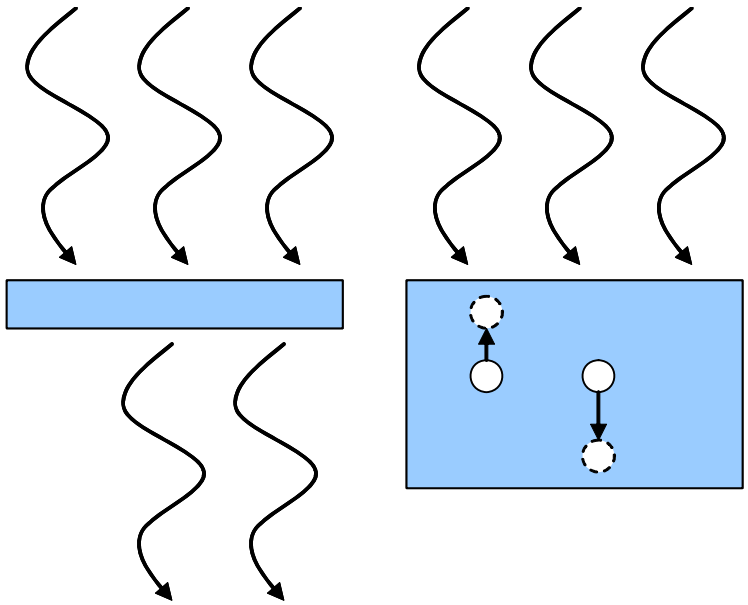

Fig. 7.1 Schematic for the trade-off issue in photovoltaic layer thickness. Thinner photovoltaic layers will have less light absorption (left) while thicker layers will have more bulk carrier recombination (right).

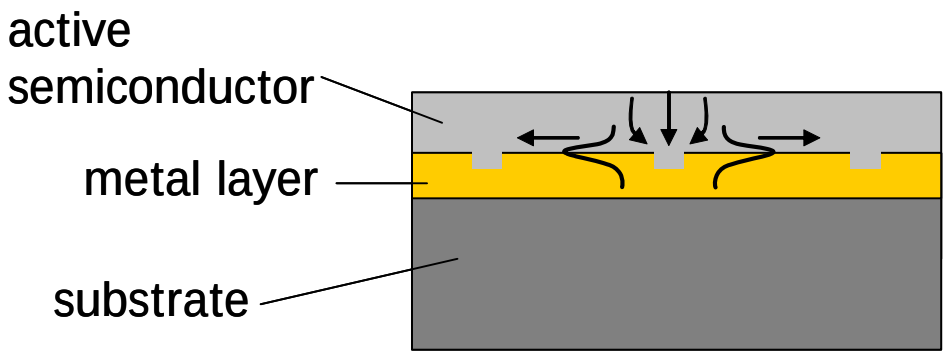

Fig. 7.2 Schematic cross-sectional of a solar cell structure with a back metal layer. The incident light is incoupled into surface plasmons propagating at the semiconductor/metal interface via subwavelength-size grooves to increase the optical path by switching the light direction from normal to the photovoltaic layer to lateral.

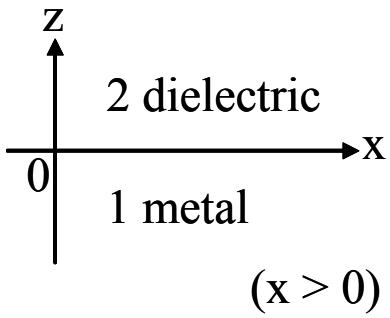

Fig. 7.3 Schematic of the layer configuration considered for the energy dissipation calculation.

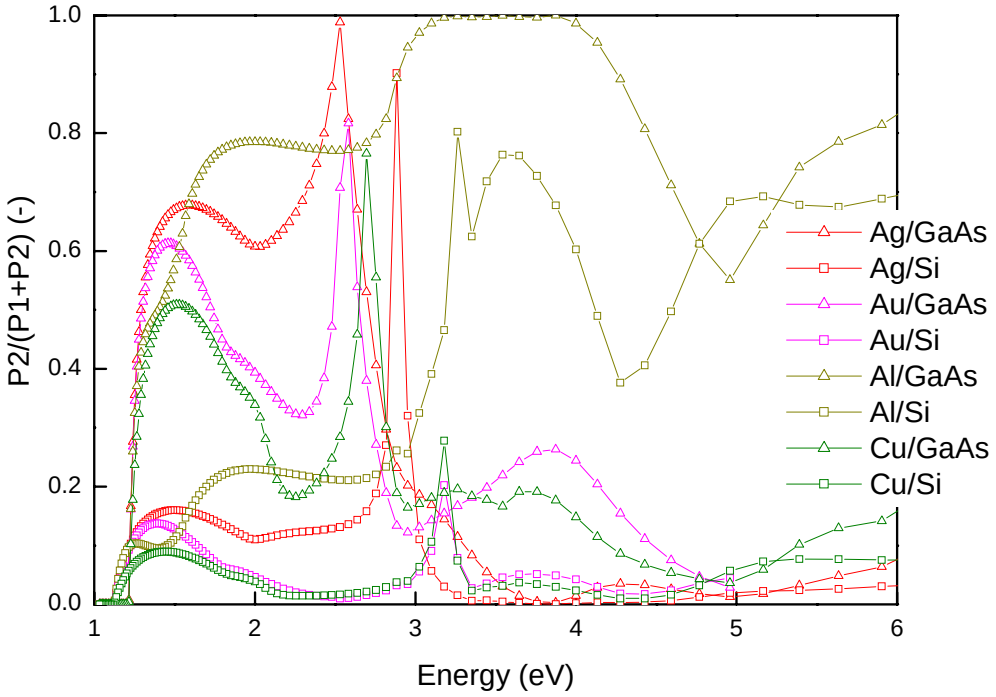
P2/(P1+P2) (-)
Energy (eV)
1.0
0.8
0.6
0.4
0.2
0.0
1
2
3
4
5
6
Ag/GaAs
Ag/Si
Au/GaAs
Au/Si
Al/GaAs
Al/Si
Cu/GaAs
Cu/Si

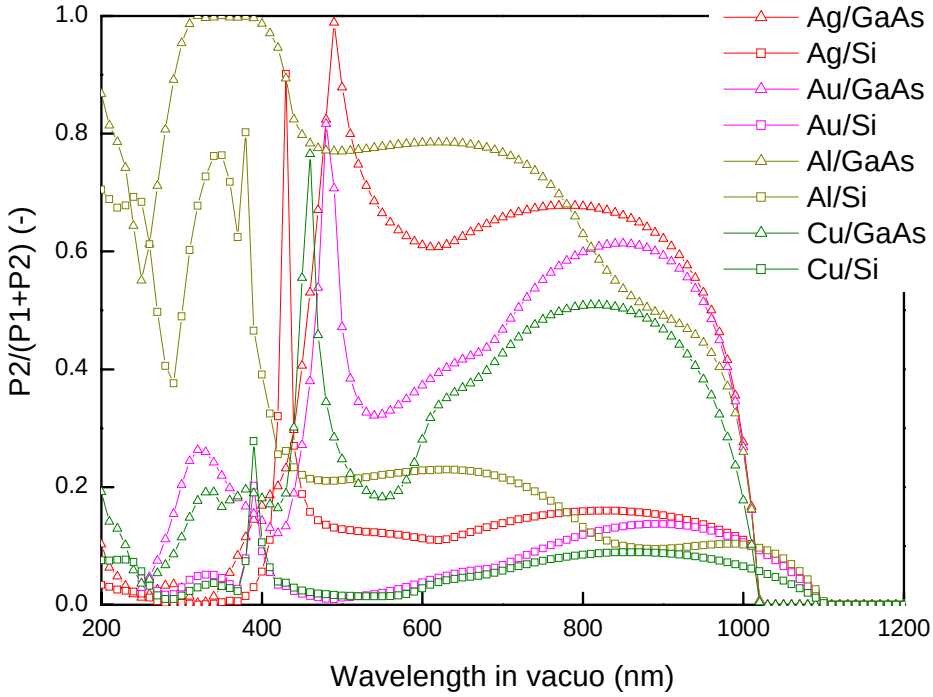

Fig. 7.4 Calculated energy dissipation fraction in the semiconductor layer from the surface plasmons propagating at the semiconductor/metal interface, depending on incident photon energy (a) and wavelength (b).

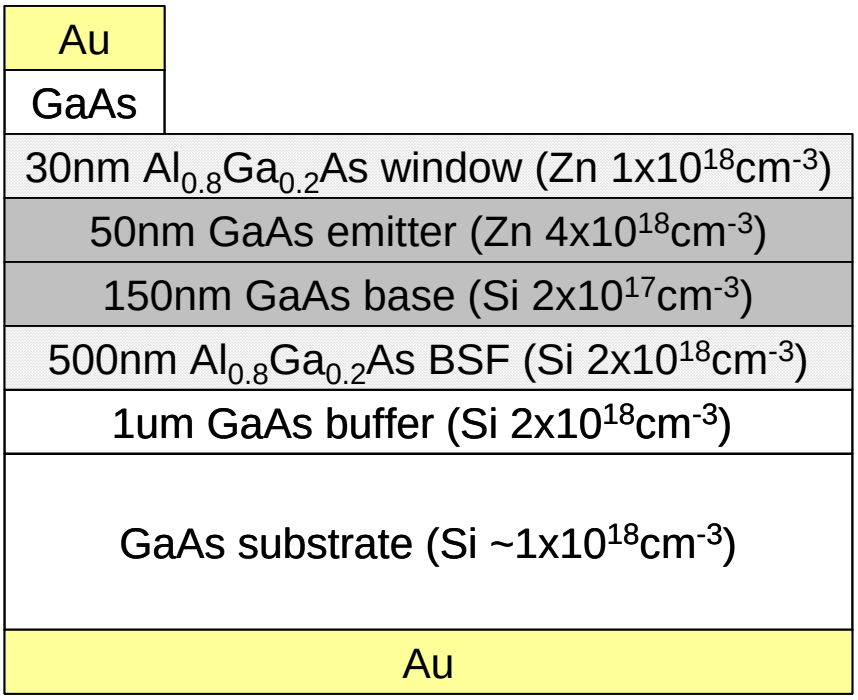

Fig. 7.5 Schematic cross-sectional diagram of the optically thin GaAs solar cell structure.

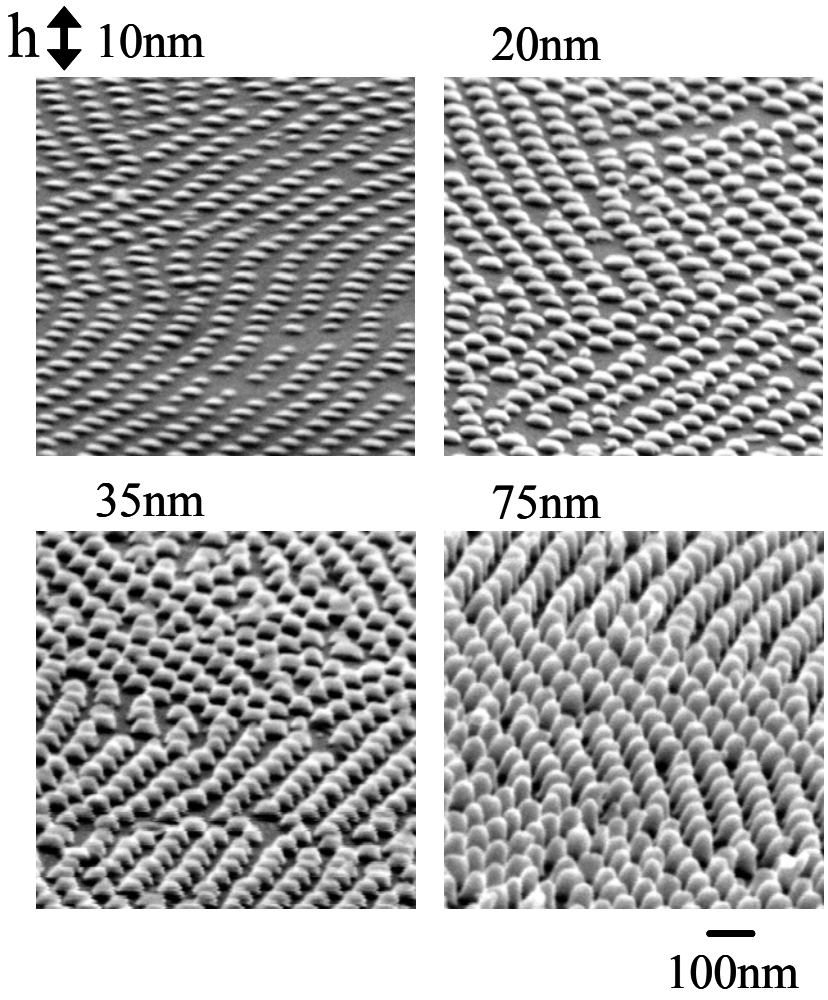

Fig. 7.6 Scanning electron microscope (SEM) images of the Ag nanoparticle arrays with a diameter of 60 nm and heights ranging through 10 nm to 75 nm deposited on the GaAs solar cells with a viewing angle of 75 degree.

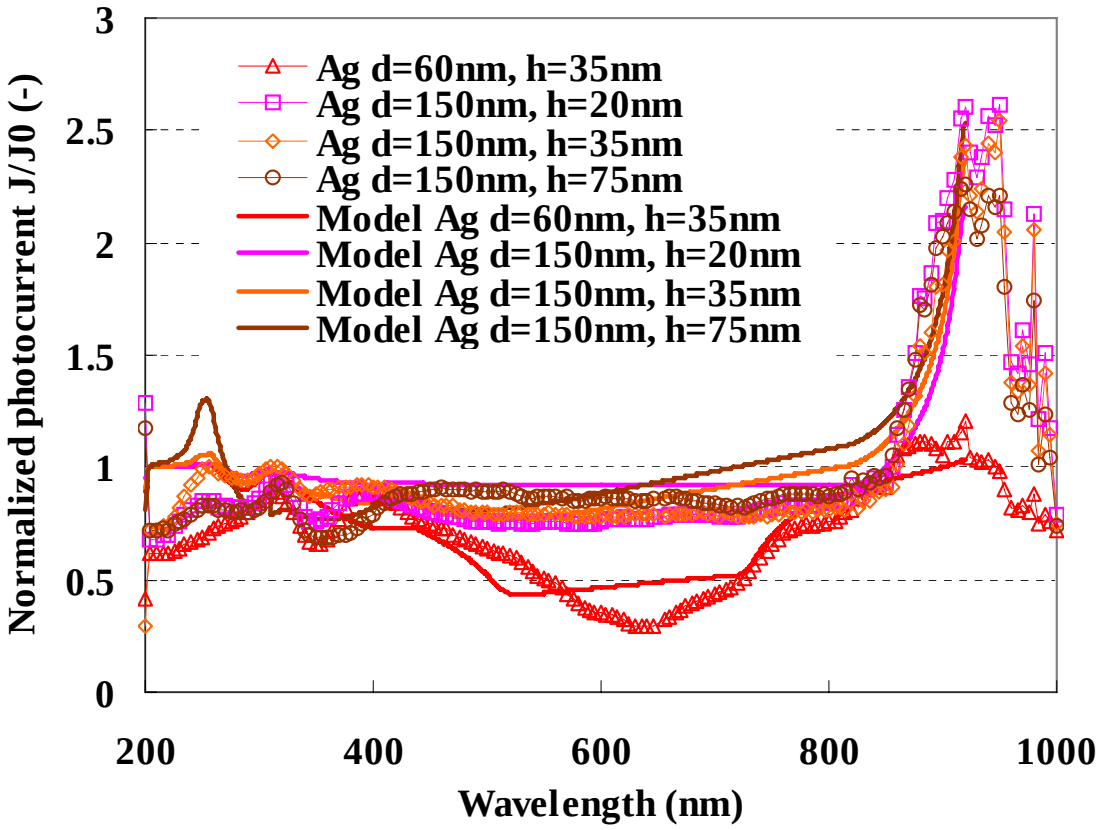
Normalized photocurrent J/J0 (-)
3
2.5
2
1.5
1
0.5
0
200
400
600
800
1000
Wavelength (nm)
Ag d=60nm, h=35nm
Ag d=150nm, h=20nm
Ag d=150nm, h=35nm
Ag d=150nm, h=75nm
Model Ag d=60nm, h=35nm
Model Ag d=150nm, h=20nm
Model Ag d=150nm, h=35nm
Model Ag d=150nm, h=75nm

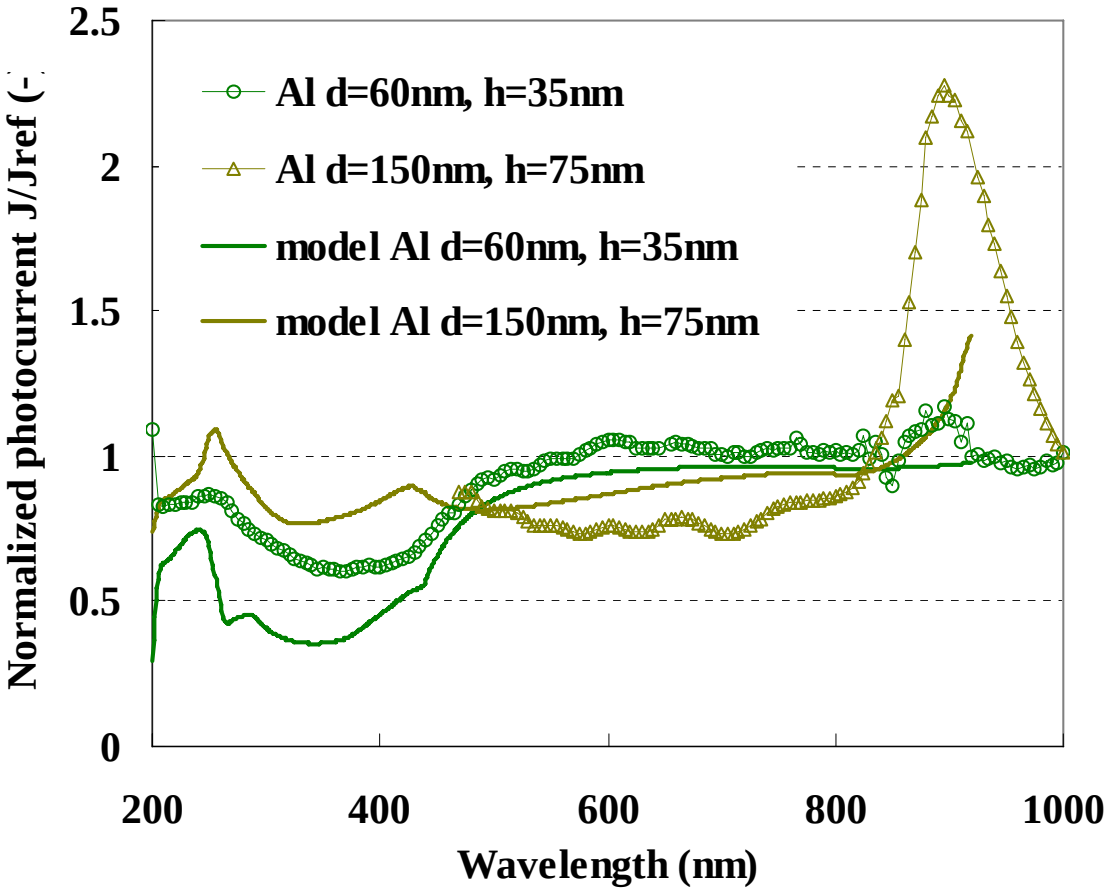

Fig. 7.7 Normalized photocurrent spectra for the GaAs solar cells with (a) Ag and (b) Al nanoparticles. Computed normalized absorbance curves in the GaAs solar cells with Ag and Al nanoparticles based on the optical model are also plotted.

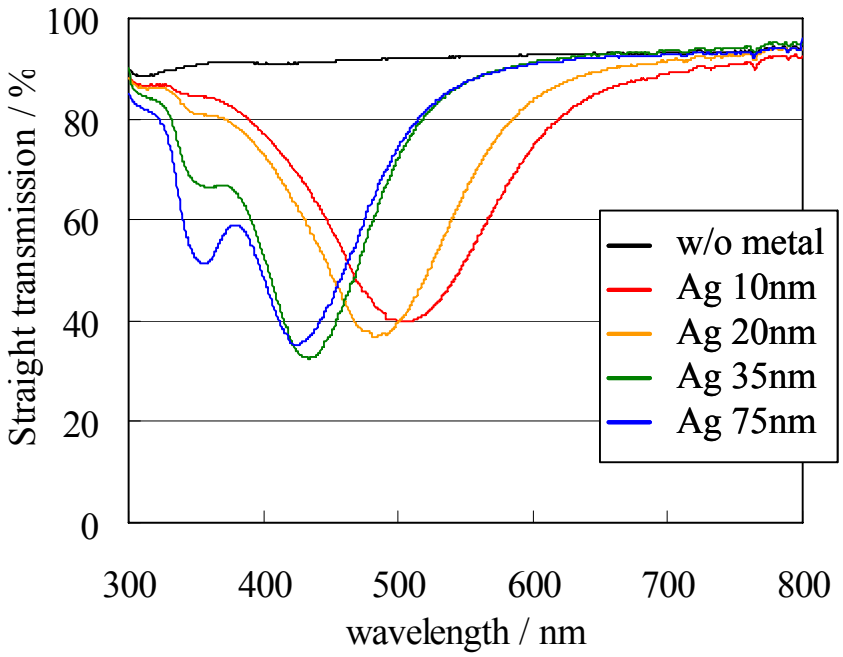

Fig. 7.8 Straight optical transmission spectra of Ag nanoparticle arrays with a particle diameter of 60 nm and various particle heights deposited onto glass substrates.

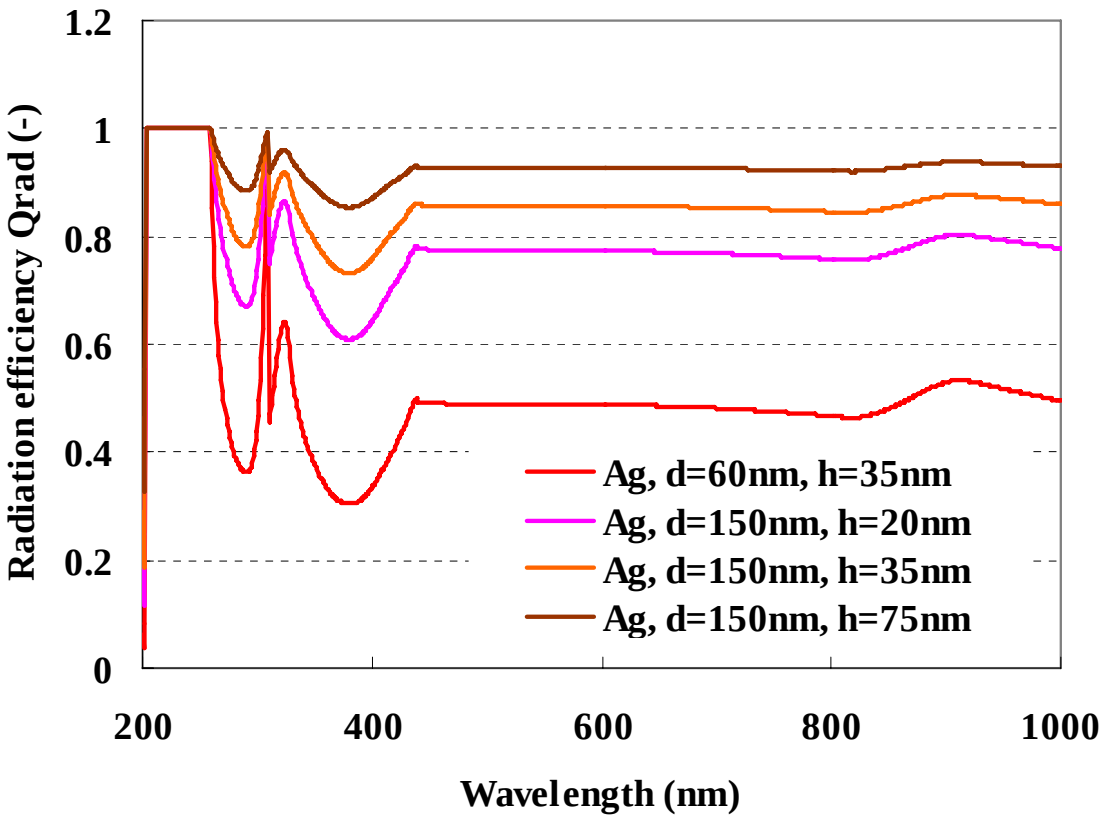

Fig. 7.9 Calculated radiation efficiency for Ag nanoparticles.

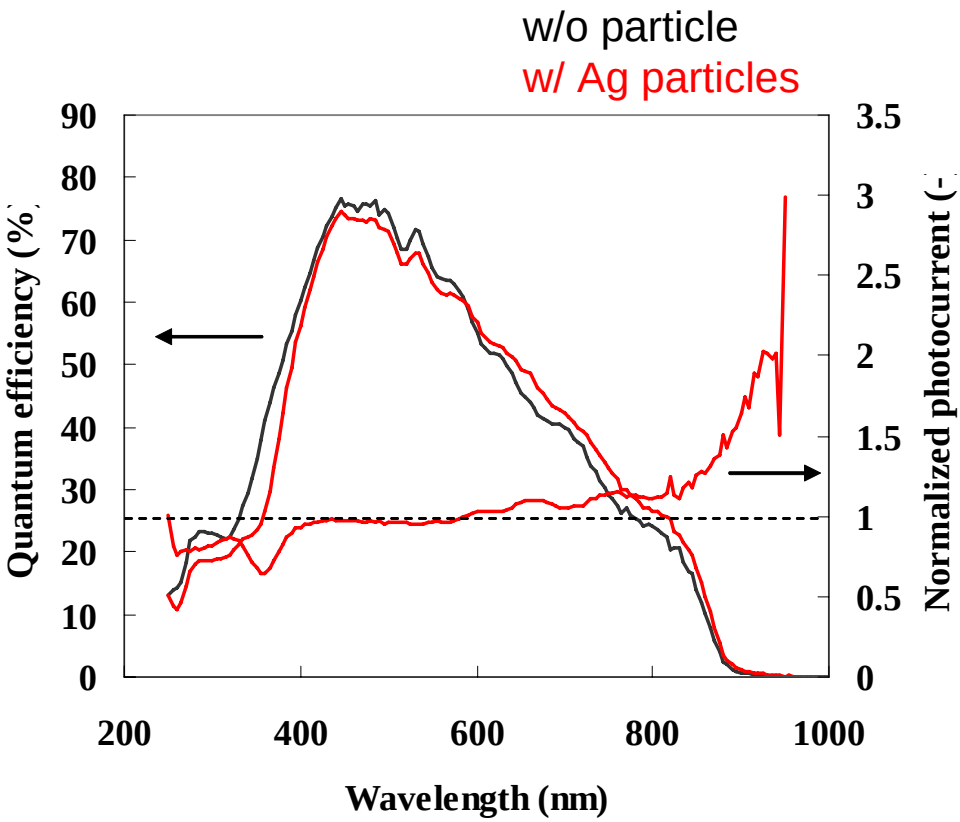
w/o particle
w/ Ag particles
Quantum efficiency (%)
Normalized photocurrent (-)
Wavelength (nm)
0
10
20
30
40
50
60
70
80
90
0
0.5
1
1.5
2
2.5
3
3.5
200
400
600
800
1000

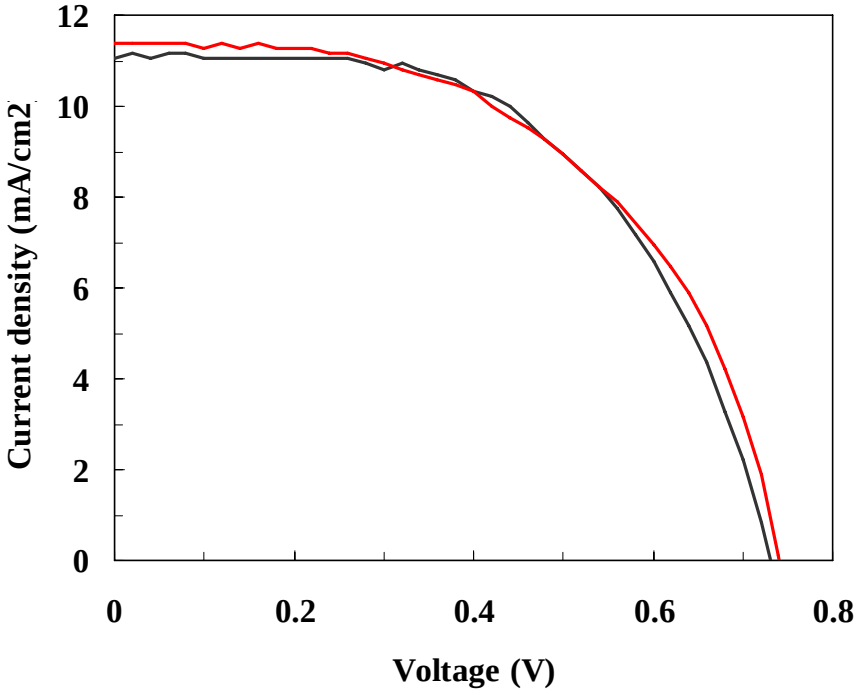

Fig. 7.10 (a) Normalized photocurrent and external quantum efficiency spectra and (b) light I-V characteristics under AM1.5G 1-sun solar spectrum for the GaAs solar cells with Ag nanoparticles with a diameter of 70 nm and height of 100 nm.

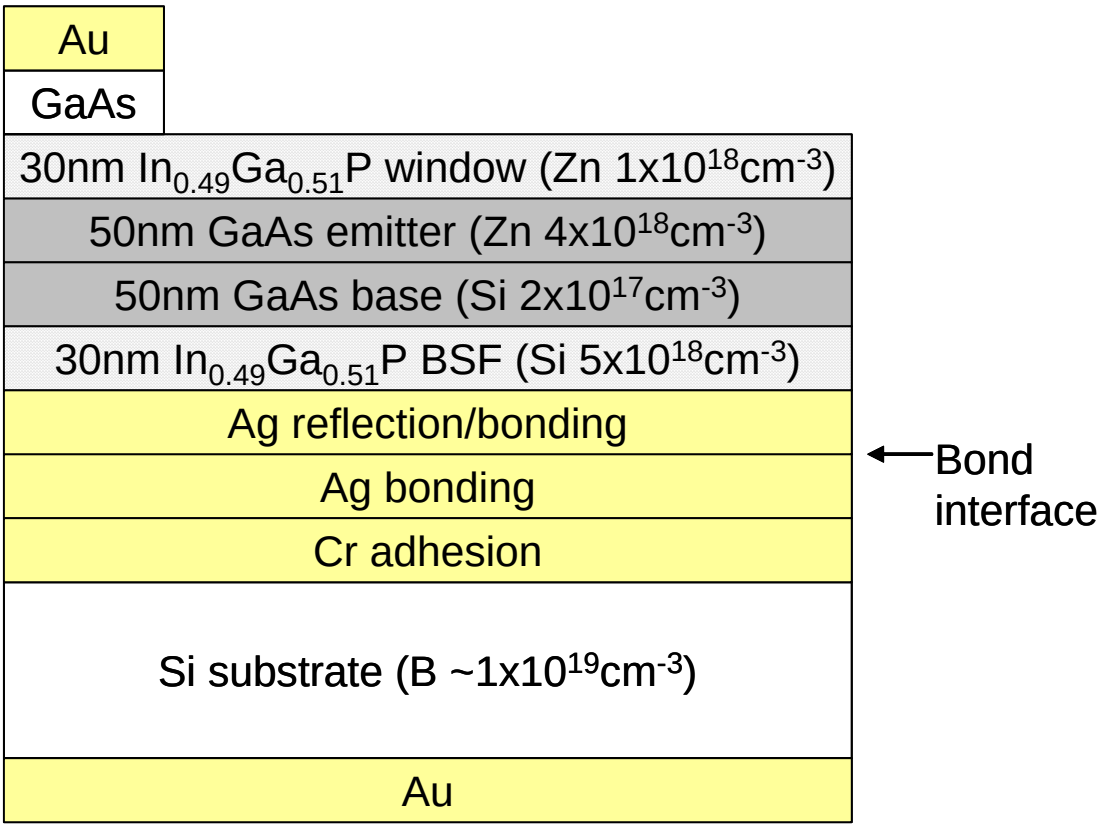
Au
GaAs
30nm $In_{0.49}Ga_{0.51}P$ window (Zn $1x10^{18}cm^{-3}$)
50nm GaAs emitter (Zn $4x10^{18}cm^{-3}$)
50nm GaAs base (Si $2x10^{17}cm^{-3}$)
30nm $In_{0.49}Ga_{0.51}P$ BSF (Si $5x10^{18}cm^{-3}$)
Ag reflection/bonding
Ag bonding
Cr adhesion
Si substrate (B ~$1x10^{19}cm^{-3}$)
Au
Bond interface

3um GaAs (Si $2x10^{18}cm^{-3}$)
30nm $In_{0.49}Ga_{0.51}P$ BSF (Si $5x10^{18}cm^{-3}$)
50nm GaAs base (Si $2x10^{17}cm^{-3}$)
50nm GaAs emitter (Zn $4x10^{18}cm^{-3}$)
30nm $In_{0.49}Ga_{0.51}P$ window (Zn $1x10^{18}cm^{-3}$)
300nm GaAs contact (Zn $5x10^{18}cm^{-3}$)
100nm $In_{0.49}Ga_{0.51}P$ etch stop (no doped)
1um GaAs buffer (Zn $2x10^{18}cm^{-3}$)
GaAs substrate (Zn ~$1x10^{18}cm^{-3}$)

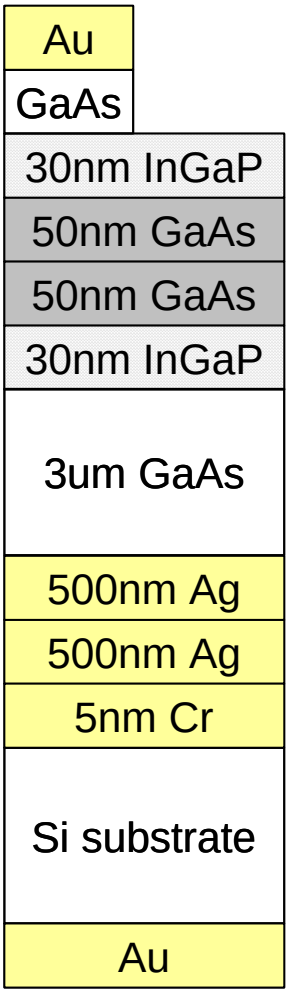

Fig. 7.11 Schematic cross-sectional diagrams of (a) the waveguide-like GaAs solar cell with metal back layer, (b) the inversely grown GaAs solar cell used for the waveguide-like cell structure and (c) the reference cell.

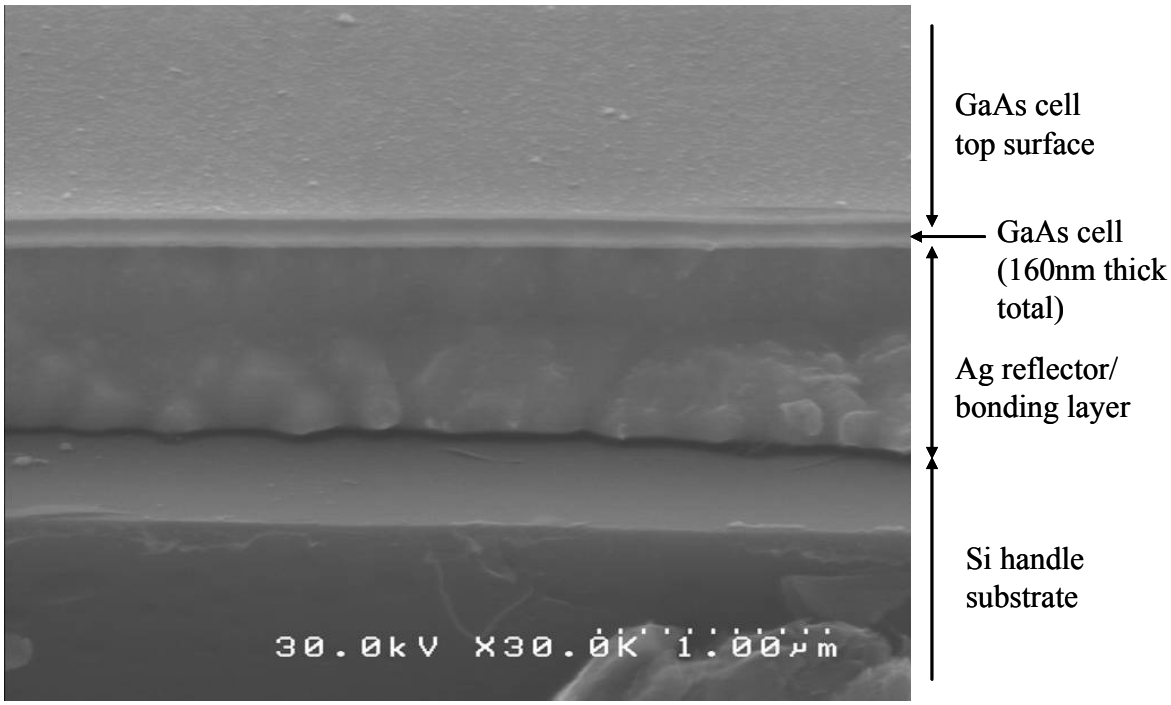

Fig. 7.12 Cross-sectional SEM image for the fabricated waveguide-like GaAs solar cell with an Ag back layer. Note that a selective chemical etching was applied for the purpose to clarify each layer.

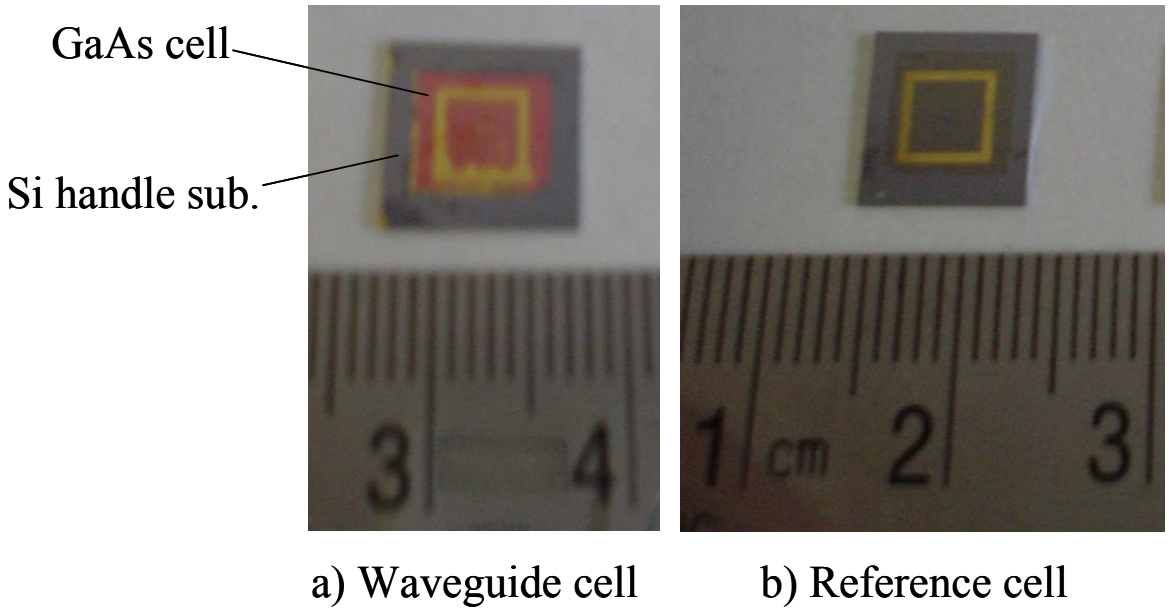

Fig. 7.13 Photographs of (a) the waveguide-like GaAs solar cell with an Ag back layer and (b) the reference cell with a 3 μm GaAs absorbing layer.

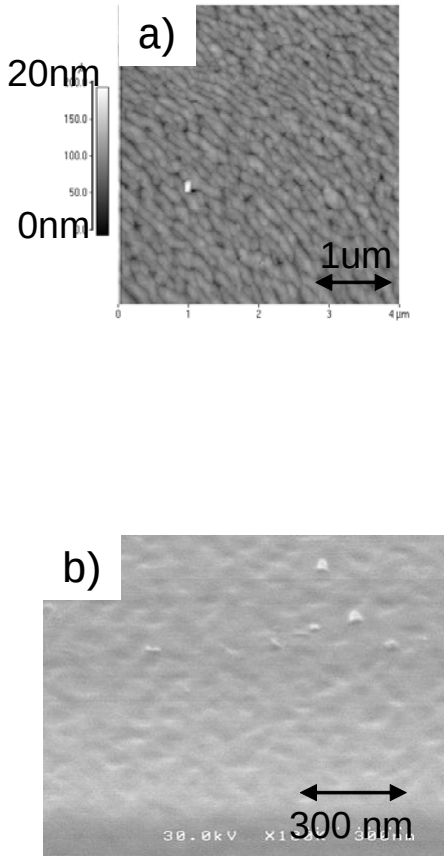

Fig. 7.14 (a) AFM and (b) SEM images of the surface of the InGaP BSF layer after removal of the 3 μm thick GaAs layer, which represents the roughness at the GaAs cell / Ag interface.

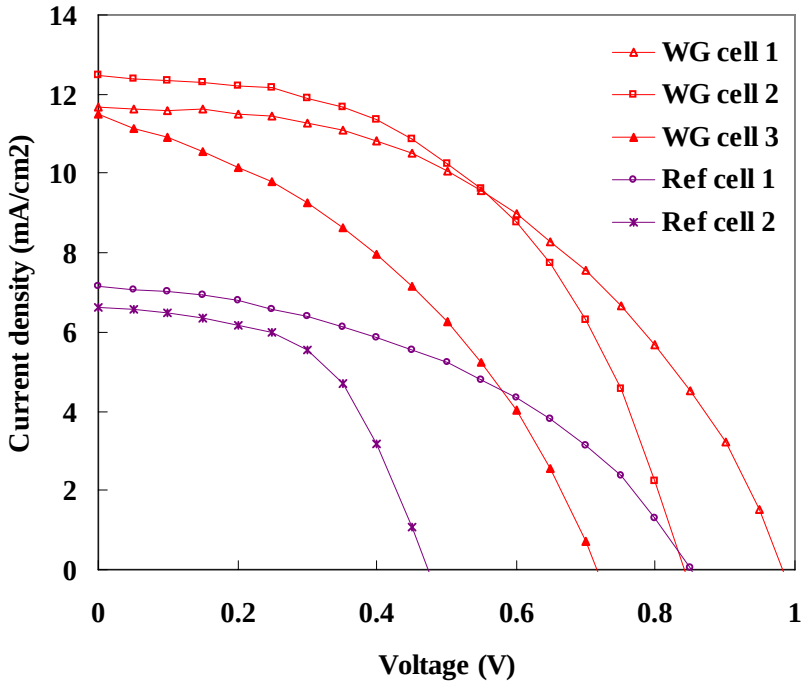

Fig. 7.15 Typical light I-V curves for the waveguide-like GaAs cells with Ag back structure and the reference GaAs cells under AM1.5 Global solar spectrum with 1-sun total intensity (100 mW cm^{-2}).

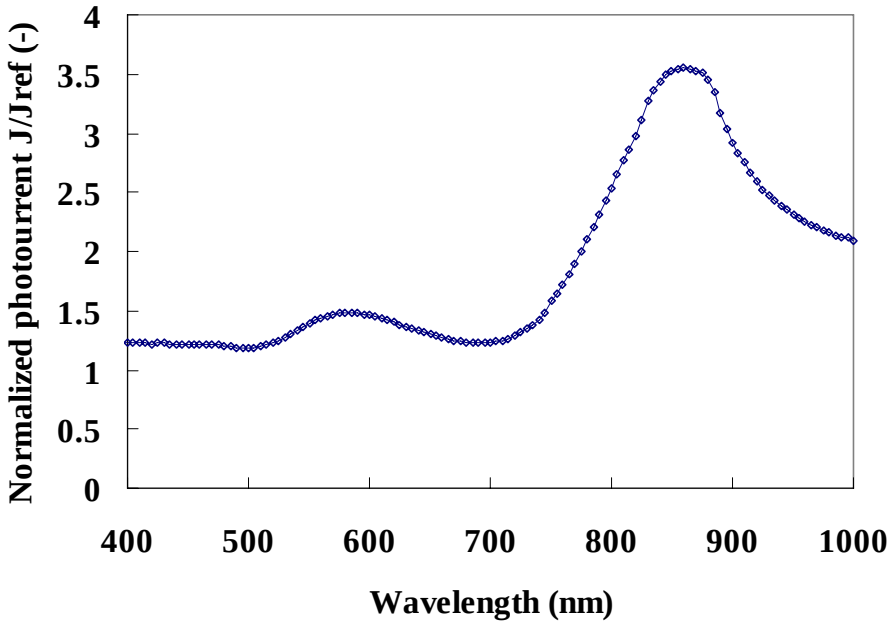

Fig. 7.16 Normalized photocurrent spectrum of the waveguide-like GaAs solar cell relative to the photocurrent of the reference cell.

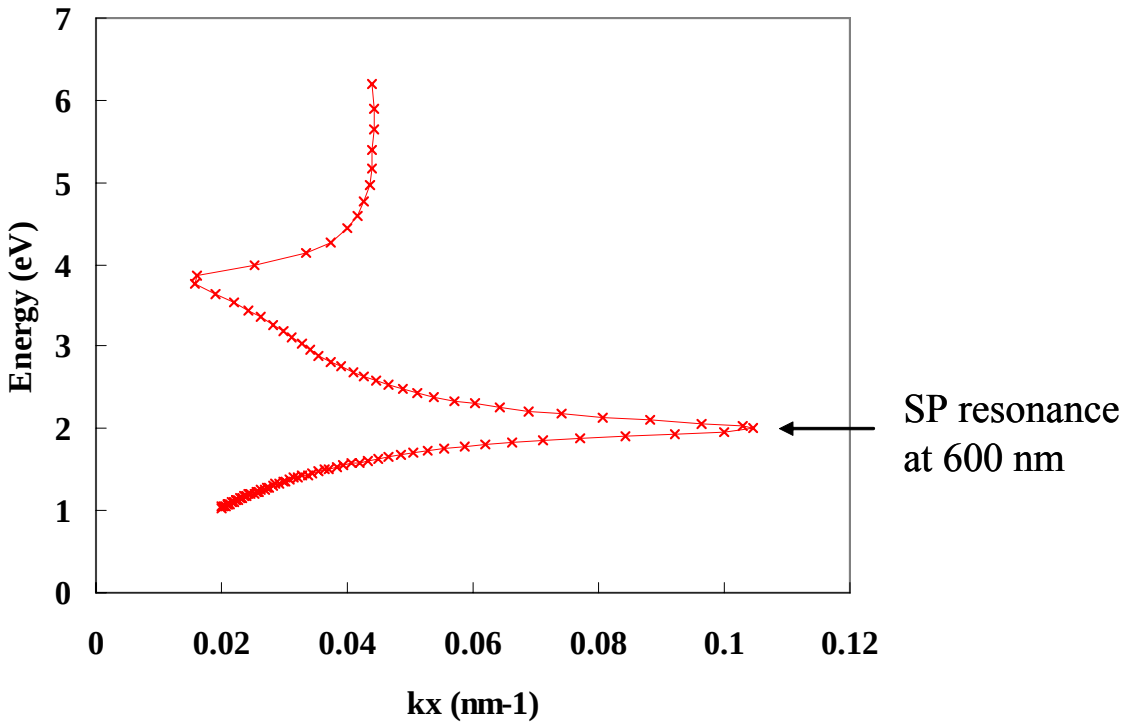

Fig. 7.17 Calculated dispersion relation at GaAs/Ag interface. Surface plasmon resonance peak is found at 600 nm, represented by the maximum of the wavevector *k* parallel to the interface.

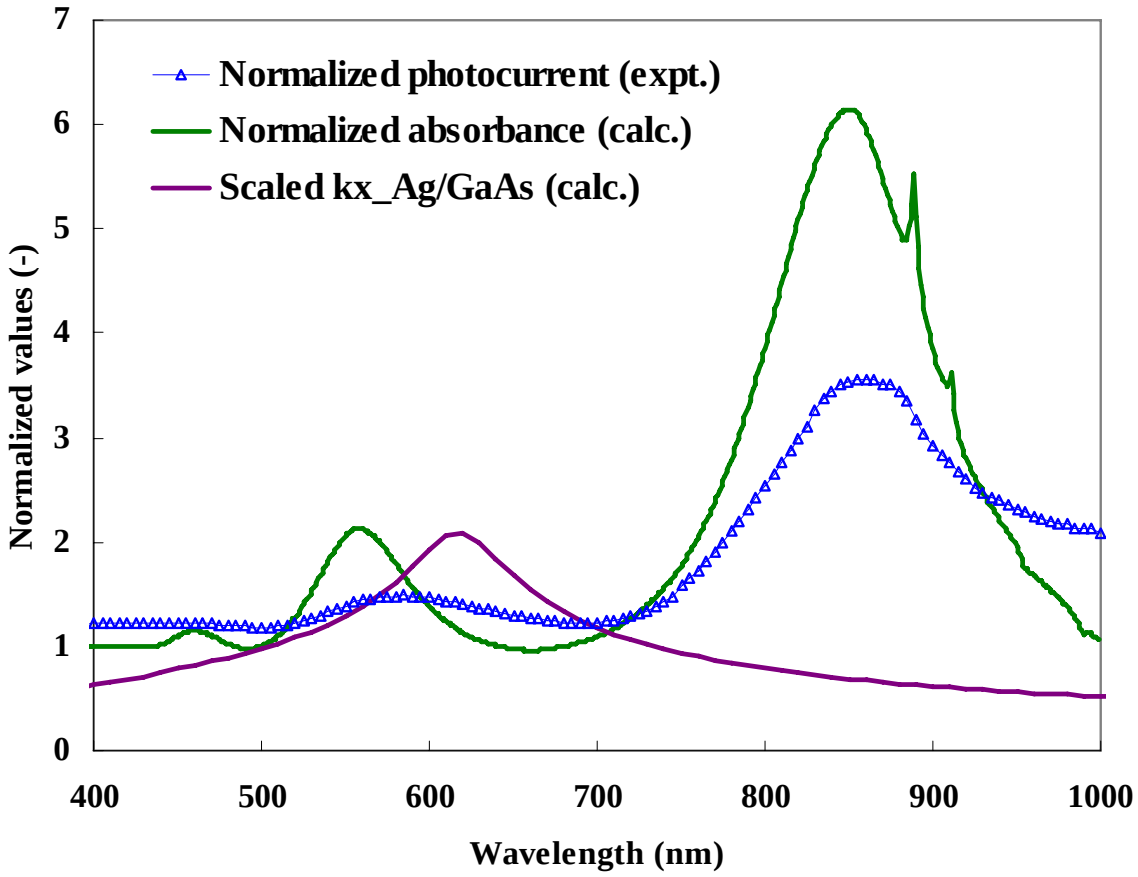

Fig. 7.18 Calculated normalized absorbance for the waveguide-like GaAs solar cell accounting Fabry-Perot resonance effect in the thin GaAs layer with the Ag back layer, as well as the wavevector parallel to the GaAs/Ag interface shown in Figure 7.17, superposed to the normalized photocurrent data in Figure 7.16.

Chapter 8 Summary

In this thesis, I have investigated three major topics, wafer-bonded multijunction solar cells, low cost alternative III-V-on-Si substrates and plasmonic solar cells. Wafer bonding technologies were applied for all of these three projects. Lattice-matched monolithic two-terminal GaAs/$In_{0.53}Ga_{0.47}As$ dual-junction solar cells were fabricated through GaAs/InP direct wafer bonding. InP/Si direct wafer bonding and also bonding with a SiO_2 bonding layer enabled high efficiency $In_{0.53}Ga_{0.47}As$ solar cells on Si via InP/Si alternative substrates. Ultrathin GaAs solar cells with Ag back structure were prepared through wafer bonding of Ag-on-GaAs and Ag-on-Si wafers. I thus have demonstrated various potential applications of wafer bonding with its excellent flexibility for materials choice focusing on novel solar cell structures.

Low resistance Ohmic GaAs/InP junctions were obtained overcoming ~4% lattice mismatch using direct wafer bonding technique. The key factors were reduction of the interfacial oxygen and hydrogen by annealing in reduction atmosphere and high doping for the interfacial bonding layers to induce tunneling current. The obtained bonded GaAs/InP structures are suitable for lattice-mismatched multijunction solar cell applications with their highly conductive interfaces. Simple considerations suggest that for such a cell the currently-reported interfacial resistance smaller than 0.1 Ohm-cm^2 would result in a negligible decrease in overall cell efficiency of ~0.02%, under 1-sun illumination.

A direct-bond interconnected multijunction solar cell, a two-terminal monolithic GaAs/InGaAs dual-junction cell, was then fabricated for the first time to demonstrate a

proof-of-principle for the viability of direct wafer bonding for solar cell applications. The bonded interface is a metal-free n^+GaAs/n^+InP tunnel junction with highly conductive Ohmic contact suitable for solar cell applications overcoming the 4% lattice mismatch. The quantum efficiency spectrum for the bonded cell was quite similar to that for each of unbonded GaAs and InGaAs subcells. The bonded dual-junction cell open-circuit voltage was equal to the sum of the unbonded subcell open-circuit voltages, which indicates that the bonding process does not degrade the cell material quality since any generated crystal defects that act as recombination centers would reduce the open-circuit voltage. Also, the bonded interface has no significant carrier recombination rate to reduce the open circuit voltage.

Such a wafer bonding approach can also be applied to other photovoltaic heterojunctions where lattice mismatch accommodation is also a challenge, such as the (Al)InGaP/GaAs/InGaAsP/InGaAs four-junction tandem cell by bonding a GaAs-based lattice-matched (Al)InGaP/GaAs subcell to an InP-based lattice-matched InGaAsP/InGaAs subcell.

Low cost InP/Si alternative substrates were successfully fabricated by He implantation of InP prior to bonding to a thermally oxidized Si substrate and annealing to exfoliate an InP thin film. The thickness of the exfoliated InP films was only 900 nm, which means hundreds of the InP/Si substrates could be prepared from a single InP wafer in principle. The photovoltaic current-voltage characteristics of the $In_{0.53}Ga_{0.47}As$ cells fabricated on the wafer-bonded InP/Si substrates were comparable to those synthesized on commercially available epi-ready InP substrates, and had a ~20% higher short-circuit

current which we attribute to the high reflectivity of the InP/SiO_2/Si bonding interface. This work provides an initial demonstration of wafer-bonded InP/Si substrates as an alternative to bulk InP substrates for solar cell applications.

Ultimately, the InP/Si substrates are also extendable to fabrication of ultrahigh efficiency four-junction (Al)InGaP/GaAs/InGaAsP/InGaAs cells via a direct bond interconnect between subcell structures of InGaAsP/InGaAs grown on InP/Si and (Al)InGaP/GaAs grown on GaAs to form the overall four junction cell structure.

Two types of "plasmonic" GaAs solar cell were investigated. Firstly, absorption enhancement by metal nanoparticle scattering in 'optically thin' GaAs solar cells was shown. Dense arrays of metal nanoparticles were deposited directly onto the $Al_{0.8}Ga_{0.2}As$ window layer of the GaAs cells through porous alumina membranes by thermal evaporation. Spectral response measurements revealed photocurrent enhancements up to 260% at 900 nm for a GaAs cell with Ag nanoparticles with 150 nm diameter, 20 nm height and 30% surface coverage, relative to reference GaAs cells with no metal nanoparticle array. This photocurrent enhancement and the spectral behavior of the normalized photocurrent are qualitatively reproduced by a simple optical model representing surface plasmon resonance of metal nanoparticles and multi-angle scattering. Particularly, larger subwavelength-size metal particles resulted in larger photocurrent due to higher radiation efficiencies both for Ag and Al. Secondly, waveguide-like GaAs solar cells with metallic back structures were introduced. Ultrathin GaAs cells with Ag back layers were fabricated through wafer bonding and layer transfer with selective etch back of the GaAs substrates. This waveguide-like GaAs cell showed net photocurrent

enhancement throughout the solar spectral range relative to the reference GaAs cell with an absorbing GaAs back layer. A large peak for the normalized photocurrent around at the GaAs bandedge was found and attributed to multiple-angle reflection at the Ag back layer. A smaller peak was found at 600 nm and is due either to surface plasmon coupling or Fabry-Perot resonance effect.

Appendix: Calculation codes

The calculations conducted in this Thesis were mostly all-analytical and therefore any reader could straightforwardly reproduce the results. There however are a couple of numerial calculations and I would like to explain them in this Appendix chapter.

The detailed balance limit efficiency calculation conducted in Chapter 2 contained only one analytical calculation. Equation 10 is a transcendental equation about V_m and I used the "Solver" function of Microsoft Excel to find the V_m which minimize the square of (left hand - right hand).

For Equation 21 in Chapter 7, absorbance in multiple-angle scattering, the integration of this equation cannot be solved analytically. I therefore conducted a numerical integration with forward Euler method with a trapezoidal approximation using Visual Basic A, built in Microsoft Excel. The code follows:

```
Sub integration_5()

'theta, s: angle
'alpha, a: absorption coefficient
'L: PV layer thickness
'F: absorbed fraction (the goal of this program)
'dF: part of F of that mesh (F = sum of dF's)
```

```
Dim s, ds, a(1000), L, F, dF As Double

L = [a7]
ds = ([a13] - [a10]) / [a16]

Dim i, i_final, j, j_final As Long

j = 0
j_final = [a19] - 4

Do

a(j) = Cells(j + 4, 15).Value
'In this macro, a(j) is actually the integrated alpha*L, not alpha.

i = 0
i_final = [a16] - 1
F = 0
s = [a10]

Do
```

```
If a(j) = 0 Then

dF = 0

ElseIf s > Cells(j + 4, 10).Value * 3.14159265358979 / 180 Then

dF = ds * 2 / 3 / 3.14159265358979 * (1 + (Cos(s)) ^ 2)

Else

'integration equation
'You can choose one of the two methods below.
'Trapezoidal method requires less meshes for convergence, but easier to overflow. (I don't
know why.)
'forward Euler
dF = ds * 2 / 3 / 3.14159265358979 * (1 + (Cos(s)) ^ 2) * (1 - Exp(-1 * a(j) / Cos(s)))
'considering one perfect reflection at the back surface

'trapezoidal
'dF = ds * (2 / 3 / 3.14159265358979 * (1 + (Cos(s)) ^ 2) * (1 - Exp(-a(j) * L / Cos(s))) +
2 / 3 / 3.14159265358979 * (1 + (Cos(s + ds)) ^ 2) * (1 - Exp(-a(j) * L / Cos(s + ds)))) / 2
```

```
'dF = ds * (1 / 3 / 3.14159265358979 * (1 + (Cos(s)) ^ 2) * (1 - Exp(-a(j) * L / Cos(s))) +
1 / 3 / 3.14159265358979 * (1 + (Cos(s + ds)) ^ 2) * (1 - Exp(-a(j) * L / Cos(s + ds))))

End If

F = F + dF

If i = i_final Then Exit Do
s = s + ds
i = i + 1

Loop

'output F into the cells on the worksheet
Cells(j + 4, 16) = F

If j = j_final Then Exit Do
j = j + 1

Loop

Beep
Beep
```

```
Beep


End Sub
```